

# **Transition Metal Doped ZIF-67/ZIF-8 Catalysts for Hydrogen Evolution Reaction**

Yudao Qin

A thesis presented for the degree of  
Doctor of Philosophy

Supervised by

Professor Zhengxiao Guo

Professor Gopinathan Sankar

Professor Junwang Tang

Professor Julian Richard Guy Evans

Department of Chemistry

Mathematical and Physical Sciences Faculty

University College London

September, 2019



## Declaration

I, Yudao Qin, confirm that the work presented in this thesis is my own. In Chapter 4, I carried out all the experiments, and the Density Functional Theory (DFT) simulations was done by my colleague, Dr Xiaoyu Han. Where information has been derived from other sources, I confirm that this has been indicated in this thesis.

## Acknowledgements

First and foremost, I would like to express my deepest appreciation to my supervisors, Professors Zhengxiao Guo and Gopinathan Sankar, for their guidance and help to my entire PhD project. Their rigorous attitude towards science and their passion for scientific research have inspired my persistent pursuit of this project. I could not have made as much achievement and progress without those. I would also like to thank my second directors, Professors Jun Wang Tang and Julian Evans, my colleagues, Drs. Srinivas Gadipelli and Xiaoyu Han for their great help and wise advice on my experiments and essay writing. I would also like to thank all my colleagues, Drs. Kaipei Qiu, Haitang Luo, Yuchen Yang and Zhuangnan Li, and Yue Lu, Juhun Shin, Jian Guo, Juntao Li, Yuting Yao, Bowen Guan and others for their support and help in the laboratory. Special thanks to Dr. Tingting Zhao for her great help in my experiments and writing. Besides, I would like to thank Dr. Steve Firth and Mr. Martin Vickers for their technical support and training. Thanks also due to all my other friends around me, who have made UCL's years unforgettable and meaningful.

Finally, I want to thank my parents and wife (Shiyuan Lu) for their love and constant support in my PhD research and my life to date.

## Publication List

1. Y. Qin, X. Han, S. Gadipelli, J. Guo, S. Wu, L. Kang, J. Callison and Z. Guo, *J. Mater. Chem. A*, 2019, 7, 6543–6551.
2. R. Xu, L. Kang, J. Knossalla, J. Mielby, Q. Wang, B. Wang, J. Feng, G. He, Y. Qin, J. Xie, A. C. Swertz, Q. He, S. Kegnæs, D. J. L. Brett, F. Schüth and F. R. Wang, *ACS Nano*, 2019, 13, 2463–2472.

## Abstract

Electrochemical water splitting is a sustainable method of producing hydrogen - the ultimate clean energy carrier. However, high cost and poor stability of the Pt catalyst for hydrogen evolution reaction (HER) hinder its wide applications. Here, the main aim of this project is to develop cost-effective and durable HER catalysts, with a focus on carbonized transition metal (Pt, Co, Ni, Fe, Mo) doped zeolite imidazolate framework (ZIF).

(1) The first approach is to obtain high catalyst dispersion while reducing overall catalyst content. More specifically, an ultra-low PtCo bimetallic catalyst embedded in porous carbon was prepared via direct annealing of Pt-doped ZIF-67. The resulting catalyst (CPt@ZIF-67) with only 5 wt.% Pt loading, exhibited superior performance with a Tafel slope of  $27.1 \text{ mV dec}^{-1}$  and an overpotential of only 50 mV at current density of  $10 \text{ mA cm}^{-2}$ . A 24-hour stability test for CPt@ZIF-67 showed negligible activity decay.

(2) Non-noble transition metals such as Ni, Fe and Co have been proved to be promising candidates in alkaline electrolytes, but they are easily corroded in acids. Herein, Ni-doped carbon nanowires (CNi@ZIF-8) was simply synthesized via carbonization of Ni-doped ZIF-8. Ni doping could both prevent the aggregation during high-temperature pyrolysis and enhance the exposure of surface active sites. CNi@ZIF-8 demonstrated a Tafel slope of  $40.4 \text{ mV dec}^{-1}$  with an overpotential of 141 mV at current density of  $10 \text{ mA cm}^{-2}$ . The optimized catalyst also gave long-term durability in 0.5 M  $\text{H}_2\text{SO}_4$ .

(3) Molybdenum carbide attracted attention in HER catalysis due to its Pt-like d-band electronic structure. CMo@ZIF-8 catalyst presented excellent HER activity and durability via carbonization of Mo-doped ZIF-8. The optimized electrocatalyst CMo@ZIF-8, required relatively low overpotentials of 310 mV to produce a current density of 10 mA cm<sup>-2</sup> and low Tafel slope (61.7 mV dec<sup>-1</sup>). Furthermore, there was no performance degradation in a durability test up to 24h.

## Impact Statement

Electrochemical water decomposition is a sustainable hydrogen production process in principle. However, its wide application has been hindered by its high cost and poor stability of Pt-based catalysts. Here, the main purpose of the PhD project is to develop a low-cost and highly durable hydrogen evolution catalyst through effective experimental design, with a focus on the carbonized transition metal-doped zeolitic imidazolate skeleton.

### Highlights

(1) HER electrocatalysts with high metal dispersion can effectively reduce the total noble metal content and retain the performance. More specifically, an ultra-low PtCo bimetallic catalyst embedded in porous carbon is directly annealed by Pt-doped ZIF-67. The obtained catalyst (CPt@ZIF-67) had only a Pt loading of 5% by weight and exhibited excellent hydrogen evolution rate and stability, due to the carbon cages generated over the bimetal clusters during annealing. The strategy can also be applied to other metal hybrids with porous carbon support for HER.

(2) Ni-doped carbon nanowires (CNi@ZIF-8) were simply synthesized by carbonization of Ni-doped ZIF-8. Ni doping not only prevents aggregation during pyrolysis, but also enhances the exposure of surface active sites to boost HER performance. The strategy of a nickel-metal doped carbon, a high-performance HER catalyst formed by high-temperature calcination, inspired by related research with similar



nanowire structured and Ni-doped electrocatalysts.

(3) Carbonized Mo-doped ZIF-8 (CMo@ZIF-8) showed excellent HER activity and durability due to its Pt-like d-band electronic structure. Therefore, a high-performance hydrogen evolution catalyst formed by changing the morphology of Mo or doping other transition metals is another effective strategy that can be widely used.

Whether it is doping cheap transition metals into precious metals, changing the catalyst structure (blocking aggregation), or looking for Pt-like d-band electronic structure (Mo), all three methods can be widely extended to the synthesis of hydrogen evolution electrocatalysts. Moreover, scaling up the quantity of electrocatalysts for HER can be further applied in fuel cell and new energy vehicles.

## Table of Contents

<b>Declaration</b> .....	iii
<b>Acknowledgements</b> .....	iv
<b>Publication List</b> .....	v
<b>Abstract</b> .....	vi
<b>Impact Statement</b> .....	viii
<b>List of Figures</b> .....	xiii
<b>List of Tables</b> .....	xx
<b>Abbreviation</b> .....	1
<b>Chapter 1 Introduction</b> .....	4
<b>Chapter 2 Literature review</b> .....	7
2.1 Fuel cells and hydrogen gas production.....	7
2.2 Basic principles of water splitting.....	9
2.2.1 Mechanism of hydrogen evolution reaction (HER) .....	11
2.2.2 Mechanism of oxygen evolution reaction (OER).....	13
2.3 ZIF-67 and ZIF-8 .....	15
2.4 Electrocatalysts for hydrogen evolution reaction.....	19
2.4.1 Noble metal based electrocatalysts.....	19
2.4.2 Non-noble transition metal based electrocatalysts (Ni, Fe, Co and Mo).....	21
2.4.3 Metal-free carbon materials .....	26
<b>Chapter 3. Aim/Research Plan</b> .....	32

## **Chapter 4. Carbonized Platinum@ZIF-67 or ZIF-8 High**

### **Performance Electrocatalysts for Hydrogen Evolution Reaction 34**

4.1 Introduction.....	34
4.2 Experiments .....	36
4.2.1 Synthesis methods.....	36
4.2.2 Physical characterization .....	37
4.2.3 Electrochemical test .....	38
4.2.4 Density Functional Theory (DFT) simulations .....	39
4.3 Results and Discussion.....	40
4.3.1 Morphology and composition.....	40
4.3.2 LSV tests for CPt@ZIF-67/ZIF-8 and different carbonization temperatures and durations .....	54
4.3.3 Optimization of CPt@ZIF-67/ZIF-8 for hydrogen evolution reaction .....	65
4.4 Conclusions.....	71

## **Chapter 5. Carbonized Ni/Co/Fe@ ZIF-67 or ZIF-8 as High**

### **Performance Electrocatalysts for Hydrogen Evolution Reaction 74**

5.1 Introduction.....	74
5.2 Methodology .....	76
5.2.1 Synthesis methods.....	76
5.2.2 Physical characterization .....	77
5.2.3 Electrochemical test .....	77
5.3 Results and Discussion.....	79
5.3.1 Morphology and composition.....	79
5.3.2 LSV performance of carbonized Ni/Co/Fe@ZIF-8.....	84

5.3.3 Optimization of carbonized Ni@ZIF-8 for hydrogen evolution reaction .....	87
5.4 Conclusions.....	91
<b>Chapter 6. Carbonized Mo@ZIF-67/ZIF-8 as High Performance Electrocatalysts for Hydrogen Evolution Reaction .....</b>	<b>92</b>
6.1 Introduction.....	92
6.2 Methodology .....	94
6.2.1 Synthesis methods.....	94
6.2.2 Physical characterization .....	96
6.2.3 Electrochemical test.....	96
6.3 Results and Discussion.....	97
6.3.1 Morphology and composition (the formation of carbon nanowires regarding to the size of ZIF structure).....	97
6.3.2 The LSV performance of carbonized Mo@ZIF-67/ZIF-8 for hydrogen evolution reaction.....	103
6.3.3 Optimization HER activity of carbonized Mo@ZIF based catalyst.....	106
6.4 Conclusions.....	106
<b>Chapter 7. Conclusions .....</b>	<b>108</b>
<b>Chapter 8. References .....</b>	<b>110</b>

## List of Figures

### Chapter 1 Introduction

Figure 1. 1 A sustainable pathway for the production and utilization of hydrogen energy.....6

### Chapter 2 Literature review

Figure 2. 2 OER mechanism for alkaline (red route) and acidic (green route) conditions. The black line shows that the OER involves the formation of a peroxide (MOH) intermediate, while the blue line demonstrates the direct reaction of two adjacent oxo (MO) intermediates to produce oxygen gas. ....15

Figure 2. 3 (a) 3D structure of ZIF-67/ZIF-8 (grey ball = carbon atom, blue ball = nitrogen atom, purple ball = cobalt/zinc atom). (b) Molecular structure of imidazolate.....17

Figure 2. 4 (a) NBO population analysis of six different nonmetallic heteroatoms in graphene matrix. pN and gN represent pyridinic and graphitic type of N, respectively. Inset shows the proposed doping sites for different elements, sites 1 and 2 are the edge and center in-plane sites, respectively, and site 3 is an out-of-plane center site in graphene.

(b) The calculated free energy ( $\Delta G_{H^*}$ ) diagram for HER at the

equilibrium potential ( $U_{\text{RHE}} = 0 \text{ V}$ ) for N- and/or P-doped graphene models. (c) Relationship between  $\Delta G_{\text{H}^*}$  and  $E_{\text{diff}}$ <sup>51</sup> Reprinted with permission from ref. 51. ....29

## **Chapter 4. Carbonized Platinum@ZIF-67 or ZIF-8 as High Performance Electrocatalysts for Hydrogen Evolution Reaction**

Figure 4. 1 Synthetic demonstration of the synthesis procedures of carbon encapsulated Pt-doped alloys embedded nitrogen-doped carbon framework. ....40

Figure 4. 2 (a) AFM image of Pt@ZIF-67. (b) 3D morphology of Pt@ZIF-67. (c) Height profile corresponding to the red line in (a). (d) AFM image of Pt@ZIF-8. (e) 3D morphology of Pt@ZIF-8. (f) Height profile corresponding to the red line in (d).....41

Figure 4. 3 SEM image of (a) Pt@ZIF-8, (b) Pt@ZIF-67, (c) CPt@ZIF-8, and (d) CPt@ZIF-67. ....43

Figure 4. 4 SEM image of (a) ZIF-67, (b) CPt@ZIF-67-600C-2h, (c) CPt@ZIF-67-700C-2h, (d) CPt@ZIF-67-800C-2h, (e) CPt@ZIF-67-900C-2h, (f) CPt@ZIF-67-900C-6h, (g) CPt@ZIF-67-900C-6h, and (h) CPt@ZIF-67-1000C-2h.....44

Figure 4. 5 TEM images for (a) as-synthesized Pt@ZIF-8, and (b) annealed CPt@ZIF-8.....45

Figure 4. 6 (a) Lattice spacing of PtCo alloy clusters in CPt@ZIF-67.

(b) TEM images for CPt@ZIF-67. (c) The size distribution of clusters in CPt@ZIF-67. It was analyzed by randomly selecting 100 nanoparticles to measure their diameters (average diameter = 2.7 nm). (d) TEM image of CPt@ZIF-67. Element mappings of (e) carbon, (f) nitrogen, (g) cobalt, and (h) platinum. ....46

Figure 4. 7 TEM image of (a) metal nanoparticles deposited onto the carbon support for CPt@ZIF-67, (b) CPt@ZIF-67 nanoparticles in homogenous solution before electrochemical test and the inset shows the size of nanoparticles. (c) TEM image of CPt@ZIF-67 after 24h electrochemical stability test and the inset shows the size of nanoparticles remains after stability test. (d) TEM image of commercial 20 wt.% Pt/C. (e) TEM image of commercial 20 wt.% Pt/C and the inset shows the size distribution of nanoparticles for commercial 20 wt.% Pt/C, it was analyzed by randomly selecting 100 nanoparticles to measure their diameters (average diameter = 5.2 nm). (f) TEM image of metal nanoparticles deposited on to the carbon support for CPt@ZIF-8.....47

Figure 4. 8 (a) TEM image of Pt@ZIF-67. Element mappings of (b) carbon, (c) nitrogen, (d) cobalt, and (e) platinum. ....48

Figure 4. 9 The PXRD diffraction pattern of (a) ZIF-67 and Pt@ZIF-67, (b) PtZIF-8 and Pt@ZIF-8, (c) CPt@ZIF-67 and CZIF-67, (d) CPt@ZIF-8 and CZIF-8, under Cu radiation, and (e) CPt@ZIF-67

under Mo radiation. ....	49
Figure 4. 10 Raman spectra of (a) CPt@ZIF-67, (b) CZIF-67-900-6, CZIF-67-900-2, C10Pt@ZIF-67-1000-2, C10Pt@ZIF-67-900-6, C10Pt@ZIF-67-900-2, C10PtZIF-67-800-2, C10PtZIF-67-700-2 and C10PtZIF-67-600-2. (c) Raman spectra of CPt@ZIF-67 before and after 24h electrochemical stability test. The peak D locates at 1340 $\text{cm}^{-1}$ , the peak G locates at 1596 $\text{cm}^{-1}$ and the 2D peak locates at 2652 $\text{cm}^{-1}$ .....	50
Figure 4. 11 XPS spectra of (a) nitrogen, (b) cobalt, (c) platinum of CPt@ZIF-67. ....	51
Figure 4. 12 XPS survey spectra of (a) CZIF-67 and CPt@ZIF-67, (b) CZIF-67 and CPt@ZIF-67 before and after 24h electrochemical stability test, (c) CZIF-8 and CPt@ZIF-8. ....	51
Figure 4. 13 $\text{N}_2$ sorption isotherms of (a) CPt@ZIF-67, (b) CZIF-67 and (c) Pt@ZIF-67. The pore size distribution of (d) CPt@ZIF-67, (e) CZIF-67 and (f) Pt@ZIF-67.....	52
Figure 4. 14 (a) Polarization curves of CZIF-67, CPt@ZIF-67, carbon black and 20 wt.% Pt/C. (b) Tafel plots of CZIF-67, CPt@ZIF-67, carbon black and 20 wt.% Pt/C. (c) I-t curve of CPt@ZIF-67 and 20 wt.% Pt/C up to 24 hours. (d) Polarization curves of carbonized Pt-doped ZIF-67 at 600 °C for 2h, 700 °C for 2h, 800 °C for 2h, 900 °C for 2h, 900 °C for 6h, 1000 °C for 2h, carbon black and 20 wt.% Pt/C. ....	54



Figure 4. 15 (a) Polarization curves of three tests for 20 wt.% Pt/C. (b) Polarization curves of CZIF-8, CPt@ZIF-8, carbon black and 20 wt.% Pt/C. (c) Tafel plots of CZIF-8, CPt@ZIF-8, carbon black and 20 wt.% Pt/C. (d) Chronopotentiometry of CPt@ZIF-8 under the current density of 10 mA cm <sup>-2</sup> up to 6 hours.....	55
Figure 4. 16 Electrochemical impedance spectra (EIS) of (a) CPt@ZIF-67 and (b) commercial 20 wt.% Pt/C over the frequency ranging from 100 kHz to 00.1 Hz at the open-circuit voltage.....	63
Figure 4. 17 Mass activity at 0.01 V (versus RHE) of the CPt@ZIF-67, CPt@ZIF-8 and Pt/C catalysts for the HER. ....	64
Figure 4. 18 (a) The electron density difference of PtCo <sub>54</sub> @C <sub>240</sub> , where the blue and yellow represents electron accumulated and diminished area, respectively. (b) The free energy diagram of HER on C <sub>240</sub> , PtCo <sub>54</sub> @C <sub>240</sub> and Pt <sub>2</sub> Co <sub>53</sub> @C <sub>240</sub> . ....	67
Figure 4. 19 The Co <sub>55</sub> (a), PtCo <sub>54</sub> (b) and Pt <sub>2</sub> Co <sub>53</sub> (c) metal clusters. Each cluster optimised to energy minimum. ....	68
Figure 4. 20 The possible reactive sites of C <sub>240</sub> and C <sub>240</sub> with Pt/Co alloy cluster inside.....	71
Figure 4. 21 The free energy diagram of naked Co and Pt/Co alloy clusters. ....	71

## **Chapter 5. Carbonized Ni/Co/Fe@ ZIF-67 or ZIF-8 as High Performance Electrocatalysts for Hydrogen Evolution**

## Reaction

Figure 5. 1 Synthetic demonstration of the synthesis procedures of carbonized Mo-doped nanoparticles (CMo@ZIF-8).....	79
Figure 5. 2 (a) SEM image of Ni@ZIF-8; (b) SEM image of carbonized Ni@ZIF-8 at 900 °C for 6 hours; (c) TEM image of Ni@ZIF-8; (d) TEM image carbonized Ni@ZIF-8 at 900 °C for 6 hours.....	80
Figure 5. 3 SEM images of (a) carbonized Co@ZIF-8; (b) carbonized Fe@ZIF-8 at 900 °C for 6 hours; .....	81
Figure 5. 4 The PXRD diffraction pattern of (a) ZIF-8 and Ni@ZIF-8, (b) CNi@ZIF-8 under Cu radiation. ....	82
Figure 5. 5 XPS spectra of (a) nitrogen, (b) nickel of CNi@ZIF-8. ....	83
Figure 5. 6 Polarization curves of CNi@ZIF-8, 20 wt.% Pt/C, carbon black, CZIF-8, CCo@ZIF-8 and CFe@ZIF-8. ....	86
Figure 5. 7 (a) Polarization curves of CNi@ZIF-8, 20 wt.% Pt/C, carbon black and CZIF-8. (b) Tafel plots of CNi@ZIF-8, 20 wt.% Pt/C, carbon black and CZIF-8. (c) V-t curve of CNi@ZIF-8 and 20 wt.% Pt/C up to 24 hours. (d) Polarization curves of carbonized Ni-doped ZIF-8 at 900 °C for 6h and 1000 °C for 6h. ....	87

## Chapter 6. Carbonized Mo@ZIF-67/ZIF-8 as High Performance Electrocatalysts for Hydrogen Evolution Reaction

Figure 6. 1 Synthetic demonstration of the synthesis procedures of carbonized Mo-doped nanoparticles (CMo@ZIF-8).....	98
Figure 6. 2 (a) SEM image of Mo@ZIF-8; (b) SEM image of carbonized Ni@ZIF-8 at 900 °C for 6 hours; (c) TEM image of Mo@ZIF-8; (d) TEM image carbonized Mo@ZIF-8 at 900 °C for 6 hours.....	99
Figure 6. 3 The PXRD diffraction pattern of CMo@ZIF-8.....	100
Figure 6. 4 XPS spectra of (a) molybdenum, (b) nitrogen of CPt@ZIF-67.....	101
Figure 6. 5 (a) Polarization curves of CMo@ZIF-8, 20 wt.% Pt/C, carbon black and CZIF-8. (b) Tafel plots of CMo@ZIF-8, 20 wt.% Pt/C, carbon black and CZIF-8. (c) V-t curve of CMo@ZIF-8 and 20 wt.% Pt/C up to 24 hours. (d) Polarization curves of carbonized Mo-doped ZIF-8 and Mo-doped ZIF-67 at 900 °C for 6h. ....	103

## List of Tables

### Chapter 2 Literature review

Table 2. 1 Three main industrial pathways for hydrogen production. ...8

Table 2. 2 Average bond length of C-N in pyrrole and pyridine. ....19

### Chapter 4. Carbonized Platinum@ZIF-67 or ZIF-8 as High Performance Electrocatalysts for Hydrogen Evolution Reaction

Table 4. 1 Pt content in CPt@ZIF-67.....53

Table 4. 2 TOF of the CPt@ZIF-67 and other catalysts.....60

Table 4. 3 Summary of representative HER catalysts in acidic electrolyte. ....61

Table 4. 4 The calculated formation energy of single Pt atom doping in Co<sub>55</sub> cluster. ....69

Table 4. 5 The calculated formation energy of dual Pt atoms doping in C<sub>55</sub> cluster. ....69

### Chapter 5. Carbonized Ni/Co/Fe@ ZIF-67 or ZIF-8 as High Performance Electrocatalysts for Hydrogen Evolution Reaction

Table 5. 1 Summary of representative HER catalysts in acidic electrolyte.....90

**Chapter 6. Carbonized Mo@ZIF-67/ZIF-8 as High Performance Electrocatalysts for Hydrogen Evolution Reaction**

Table 6. 1 Summary of representative HER catalysts in acidic electrolyte.....105

## Abbreviation

AHF	Ammonium hexafluorophosphate
Ar	Argon
AES	Atomic emission spectroscopy
ALD	Atomic layer deposition
BET	Brunauer-Emmett-Teller
CO <sub>2</sub>	Carbon dioxide
CO	Carbon monoxide
CNT	Carbon nanotubes
CA	Chronoamperometry
BH <sup>+</sup>	Conjugate acid
OH <sup>-</sup>	Conjugate base
CV	Cyclic voltammetry (CV)
ECSA	Electrochemically active surface area
EIS	Electrochemical impedance spectroscopy
$\Delta G_{H^*}$	Free energy of hydrogen adsorption
$\Delta G$	Gibbs free energy
GO	Graphene oxide
H <sub>2</sub>	Hydrogen

H <sub>3</sub> O <sup>+</sup>	Hydronium cation
QH	hydrogen adsorption
HER	hydrogen evolution reaction
Im	Imidazolate
Fe	Iron
LSV	linear sweep voltammetry
MP-AES	Microwave plasma atomic emission spectroscopy
Mo	Molybdenum
MoP	Molybdenum phosphide
MoP S	Molybdenum phosphosulfide
np-Mo <sub>2</sub> C NWs	Nanoporous molybdenum carbide nanowires
NBO	Natural bond orbital
Ni	Nickel
N <sub>2</sub>	Nitrogen
OER	Oxygen evolution reaction
PBE	Perdew-Burke-Ernzerhof
PDA	Polydopamine
PXRD	Powder X-ray diffractometer
reduced graphene oxide	rGO
RHE	Reversible hydrogen electrode
RDE	Rotating disk electrode
SEM	Scanning electron microscopy

TEM	Transmission electron microscopy
TOF	Turnover frequency
VASP	Vienna ab-initio Package
H <sub>2</sub> O	Water
XPS	X-ray photoelectron spectroscopy
ZIF	Zeolite imidazolate frameworks



## Chapter 1 Introduction

Fossil fuels are now widely used in people's daily lives. Whatever electricity usage in households, car driving or the energy supply in the industry, environmental pollution caused by large-scale fossil fuel combustion, such as global warming, has always been the focus of the world (Figure 1.1).<sup>1</sup> The energy crisis is also looming issue. According to a recent report, global energy demand will increase by 30% by 2040, and carbon dioxide emissions will reach 3.57 billion tons a year at the same time.<sup>2</sup> Therefore, the establishment of sustainable energy systems in virtually all countries across the world is the most urgent need and the greatest challenge for mankind. To this end, scientists around the world are working on various fields of research, such as the development and application of renewable energy such as hydropower, biomass, tidal energy, solar energy, and wind energy.<sup>3,4</sup> However, the spatial limitation, high cost and temporal discontinuity required for these energy sources lead to relatively low energy transmission efficiency. Therefore, a satisfactory solution is to convert these renewable energy sources into chemical fuels that are easy to store and transport. Hydrogen (H<sub>2</sub>), with the highest gravimetric energy density among all chemical fuels (142 MJ kg<sup>-1</sup>) is considered to be the ultimate clean energy carrier, which can significantly reduce carbon (CO<sub>2</sub>) emissions, at least at point of use.<sup>5</sup>

Photoelectrochemical and electrochemical water splitting are currently the two most effective and clean strategies to achieve solar-hydrogen conversion. However, compared to electrochemical water

decomposition, the photoelectrochemical strategy is restricted by its small current density, less gas production per unit time, the large footprint of the decomposition system and the choice of viable catalysts.<sup>6,7</sup> Therefore, electrochemical water splitting has greater flexibility and applicability and can effectively overcome the drawbacks of intermittence of renewable sources, in other words, to enhance the diversity of renewable energy sources with the help of grid-scale renewable energy collection infrastructure. Figure 1.1 shows a sustainable pathway for hydrogen cycling for both industry and domestic use. The whole cycle contains hydrogen gas, oxygen gas, water and electricity only, without any harmful and unsustainable side products.<sup>8</sup> Besides, H<sub>2</sub> is an ideal fuel for proton exchange membrane fuel cells which are the key component of electric vehicles. As a result, the development of efficient water electrolysis systems is key, enabling non-polluting H<sub>2</sub> production to create a clean and sustainable energy system for the future.

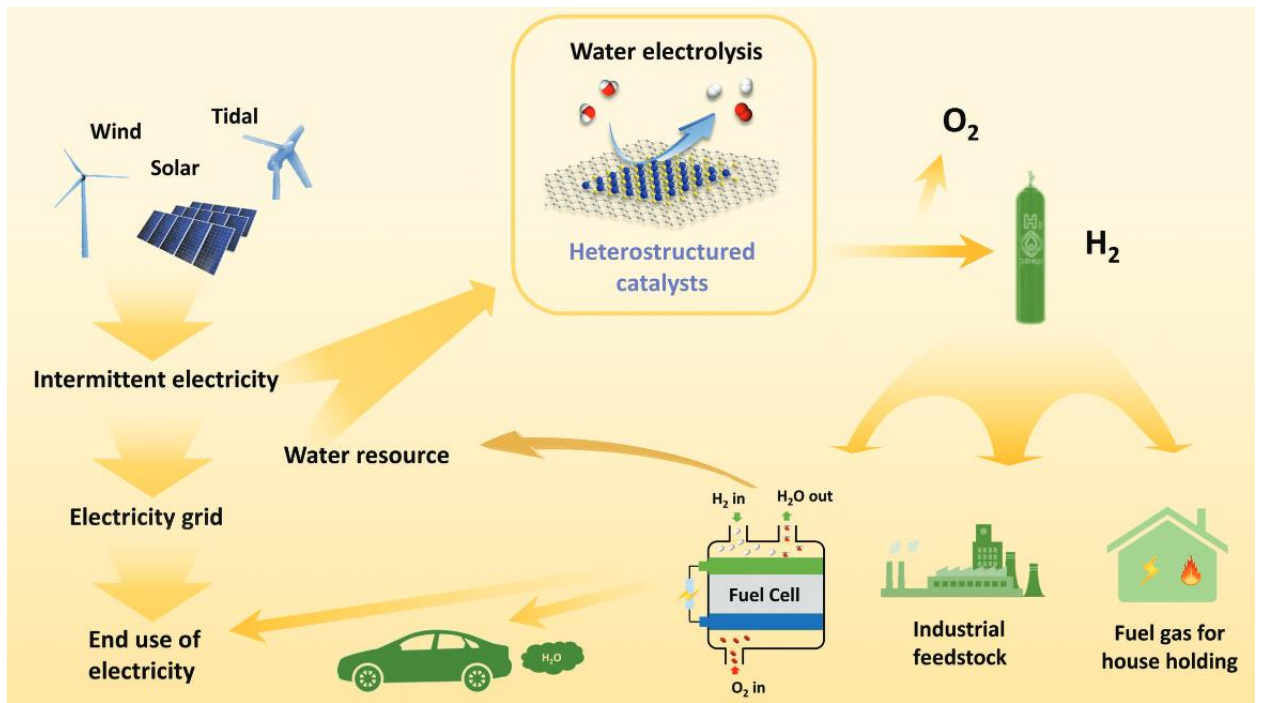


Figure 1. 1 A sustainable pathway for the production and utilization of hydrogen energy.

## Chapter 2 Literature review

### 2.1 Fuel cells and hydrogen gas production

Hydrogen is widely applied in our daily life, such as being used as a kind of stationary power. Due to its high energy density, hydrogen is widely produced and has a broad range of applications in everyday life, such as power stations, which produce energy, and in transport, with hydrogen-powered vehicles. The world produces tens of millions of tons of hydrogen every year, mainly for large-scale industrial purposes. The commercial production of hydrogen comes from four main sources: natural gas, oil, coal and electrolysis, which account for 48%, 30%, 18% and 4% respectively of the world's hydrogen production markets.<sup>9</sup> As people become increasingly aware of the need to reduce greenhouse gas emissions and achieve a new energy paradigm, it can be seen that hydrogen plays a more and more crucial role. Hydrogen provides effective chemical storage of electrical energy and can be easily converted to electricity with various applications. The European Hydrogen Association, American Hydrogen Association and Hydrogen Energy Systems Society of Japan all suggest that the revival of hydrogen generation and utilization is based on its capacity for improving energy efficiency and reducing greenhouse gas emissions from many aspects, hence enabling the global electrification trends. Commercial hydrogen is largely used in the refining process, where hydrogen is used to purify crude oil and to increase the hydrogen-to-carbon fuel ratio. Hydrogen has further applications in the production of ammonia for fertilisers, the manufacture of semiconductors in solar

panels, the “upgrading” of transition metals and many other industrial applications.

Table 2. 1 Three main industrial pathways for hydrogen production.

Method	Reagents	Products	Main reaction pathway
Steam methane reforming	Methane and steam	H <sub>2</sub> and CO <sub>2</sub>	$\text{CH}_4 + 2\text{H}_2\text{O} \rightarrow 4\text{H}_2 + \text{CO}_2$
Coal gasification	Coal and steam	H <sub>2</sub> and CO <sub>2</sub>	$\text{C} + 2\text{H}_2\text{O} \rightarrow 2\text{H}_2 + \text{CO}_2$
Water electrolysis	Water and electricity	H <sub>2</sub> and O <sub>2</sub>	$2\text{H}_2\text{O} \rightarrow 2\text{H}_2 + \text{O}_2$

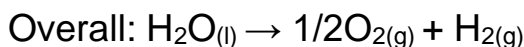
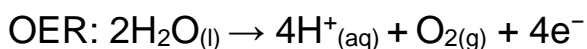
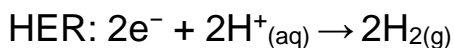
There are many hydrogen production methods, mainly intended for industrial use, but three methods dominate the world’s hydrogen production. These methods are steam methane reforming, coal gasification, and water electrolysis (Table 2.1).<sup>10</sup> Over 95% of hydrogen is manufactured by the first two methods, whereas water electrolysis only accounts for about 4% of the total. This means that current industrial technologies still rely heavily on carbon-based materials, fossil fuels, which are non-renewable and produce carbon dioxide (CO<sub>2</sub>), contributing to the greenhouse effect and exacerbating air pollution. For instance, during steam reforming, the complete combustion of methane and steam at high temperatures (600-1000 °C)

produces CO<sub>2</sub>. However, if incomplete combustion occurs (due to low temperature and shortage in energy supply), carbon monoxide (CO), a highly toxic and flammable gas, will be produced and released into the atmosphere. Consequently, steam methane reforming and coal gasification violate the purpose of reducing the greenhouse effect by promoting the utilization of hydrogen gas.

In batteries or fuel cells, reactants and products are separated to prevent chemical reaction with each other by the corrosive electrolyte. In addition to effectively separating anode and cathode gases or liquids (i.e. fuel and air, or hydrogen and oxygen), electrochemical reactions are mediated at both anodes and cathodes by exchanging specific ions at a very high rate. In a simple fuel cell, the reaction can take place between hydrogen and oxygen gases, a proton or oxide ionic current being driven through the electrolyte. Electronic current is formed at the electrodes. It can then be used to perform the purpose of fuel cell. If a similar device is in running but in the opposite direction of electron flow, this process is named as electrolysis (i.e. hydrogen evolution reaction), and hydrogen gas is produced. When the redox reactions take place in the fuel cell, energy storage system forms. Whether through a fuel cell, electrolysis or and energy storage system, oxygen simply can be obtained from air, but hydrogen is quite hard to manufacture. Therefore, in order to find a sustainable means of obtaining a large amount of fuel, electrolysis should be the preferred choice.

## **2.2 Basic principles of water splitting**

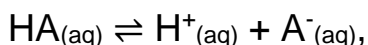
Generally, water electrolysis consists of two half reactions; the hydrogen evolution reaction (HER) and the oxygen evolution reaction (OER); the mechanisms of which are described in the following equations:



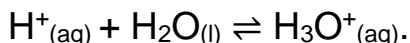
Under the standard conditions, 273.15 K and 1 atm, the Gibbs free energy ( $\Delta G$ ) of water decomposition reaction is 237.2 kJ mol<sup>-1</sup>, equivalent to the voltage of water splitting, 1.23V.<sup>11</sup> However, in fact, due to kinetic barriers, greater voltage needs to be applied to drive both HER and OER. In the words, the overpotential is much too high and this is therefore not a sustainable method for hydrogen gas synthesis. Electrocatalytic materials can stick on the electrode's surface in order to reduce overpotential. Precious metals, for instance, 20 wt.% Pt/C for HER and IrO<sub>2</sub> for OER are both commercialized in this process.<sup>12,13</sup> However, due to the scarcity and high price of precious metals, this prevents the large-scale application of this process in both laboratories and industry. Hence, it would be of great significance to reduce the quantity of noble metals used for water splitting, or to develop highly active earth-rich catalysts to promote the efficiency of the process, but also retain the activity and stability of catalysts in order to achieve a sustainable hydrogen production pathway.

### 2.2.1 Mechanism of hydrogen evolution reaction (HER)

HER is a two-electron transfer process which is shown in the half equation. The entire HER process is divided into two simple steps: absorption and desorption (Figure 2.1). Firstly, the protons - from the electrolyte are attached to the empty active sites of the catalysts on the electrode. The electrons from the electrode (catalyst) then combine with the free hydrogen positive ions to form hydrogen atoms. Two hydrogen atoms are coupled to give a gaseous hydrogen molecule ( $H_2$ ). In acidic electrolytes, the proton source is hydronium cation ( $H_3O^+$ ). Dissociation of acids takes the form:

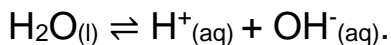


where HA represents the acid and  $A^-$  is the conjugate base. In water, the reaction is:

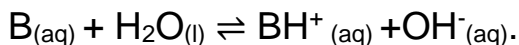


Hydrogen ions  $H^+_{(aq)}$  are easily dissociated from acid and react with water molecules ( $H_2O$ ) to create hydronium ions  $H_3O^+$ , which are the source of protons in acids.

In alkaline solutions, the proton source is water molecules ( $H_2O$ ):



A base B and water are used to generate a conjugate acid ( $BH^+$ ) and a conjugate base ( $OH^-$ ) by the following equilibrium equation:



In the alkaline solution, this process only generates  $OH^-$ . The proton comes from the dissociation of the water molecule  $H_2O$ . After this



process is completed, desorption takes place and molecular hydrogen leaves the site of the electrode (catalyst) and once again enters the solution (electrolyte). H<sub>2</sub> formation occurs via two different reaction pathways: with a Pt catalyst and without a Pt catalyst. When a Pt catalyst, two absorbed hydrogen atoms stick to the surface of the catalyst (electrode) and simultaneously combine to create a molecule of H<sub>2</sub>. This process is known as the Volmer-Heyrovsky mechanism. If there is no catalyst, the proton will attack the absorbed hydrogen atom which is attached to the electrode. These two atoms combine to produce H<sub>2</sub> gas, which is recognized as the Volmer-Tafel mechanism. The free energy of hydrogen adsorption ( $\Delta G_{H^*}$ ) is widely accepted as a description of a hydrogen evolution catalyst. Negative  $\Delta G_{H^*}$  means that H<sup>+</sup> combines favourably with the electrode surface, which is the preferred Volmer step, but if the absolute value of the  $\Delta G_{H^*}$  is too large, the subsequent Tafel or Heyrovsky steps will be difficult. On the contrary, if the catalyst has a large and positive  $\Delta G_H$ , the energy barrier for the whole reaction will be high and therefore reduce the efficiency of hydrogen molecule production as the interaction between protons and electrode surface is very weak. Therefore, the active HER catalyst should have a  $\Delta G_H$  of near zero.

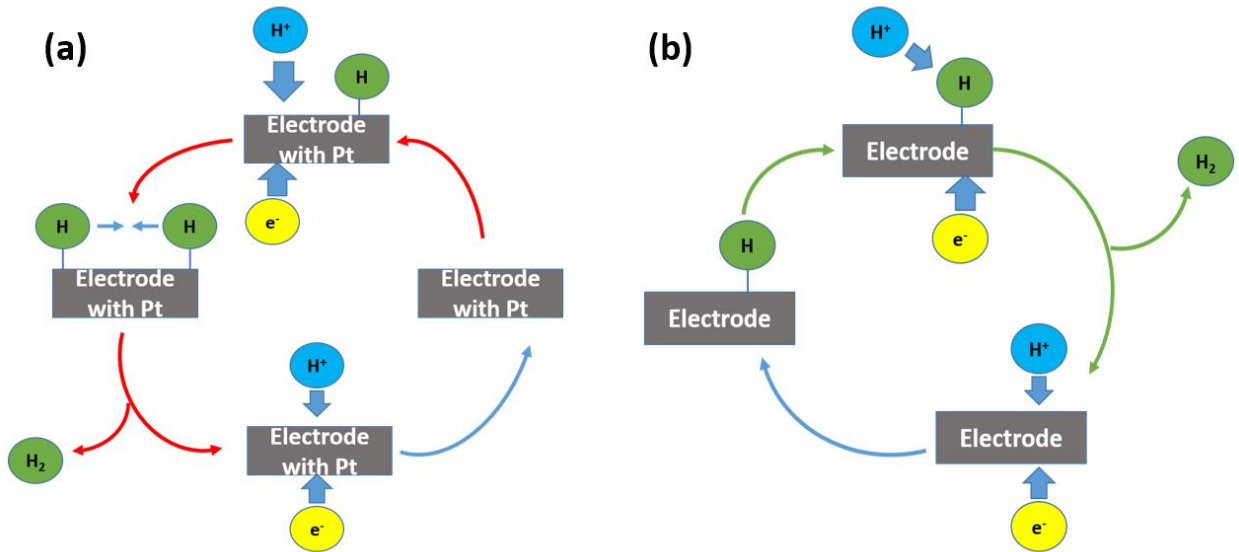
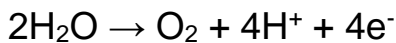


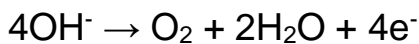
Figure 2. 1 Electrochemical desorption of hydrogen species on electrode (a) with Pt catalyst; (b) without Pt catalyst.<sup>3</sup>

### 2.2.2 Mechanism of oxygen evolution reaction (OER)

OER can be operated both under acidic and alkaline conditions. The overall reaction mechanism in an acidic electrolyte is:

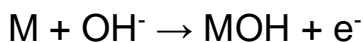


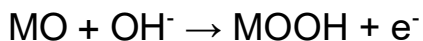
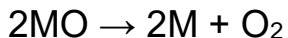
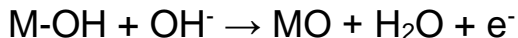
Similarly, in an alkaline electrolyte, the electron transfer pathway is:



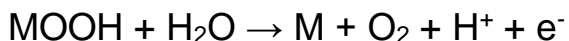
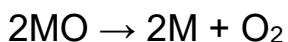
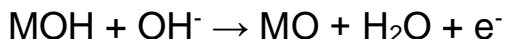
These two mechanisms are shown in Figure 2.2.<sup>14</sup> The possible mechanisms of OER under alkaline and acidic conditions have been proposed in detail below (M represents the surface of the electrocatalyst)

Alkaline conditions





Acidic conditions:



The proposed mechanisms include essential intermediates, such as MOH and MO, while the main difference in the two approaches is the formation of the oxygen molecule. It is worth mentioning that both methods produce the same intermediate, MO. In the green route, oxygen gas is produced by the direct combination from 2MO. Likewise, the alternative route involves the formation of an MOOH intermediate. MOOH decomposes into oxygen gas, which is illustrated in the last two steps of the mechanism. In summary, the crucial factor for an overall OER reaction is the bonding interaction (MO) with intermediates (MOH, MO and MOOH). The four-electron reaction can either be electron transfer steps or association/dissociation chemical steps.<sup>15</sup> Another factor in the catalytic ability of OER is the Tafel slope in electrocatalysis. A shallow Tafel slope means high HER kinetics. It also leads to the rate determining step at a later stage.

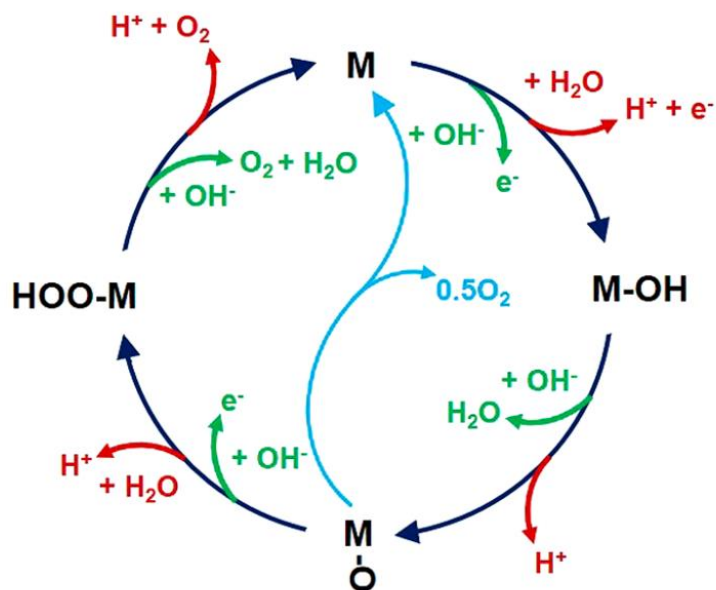


Figure 2. 2 OER mechanism for alkaline (red route) and acidic (green route) conditions. The black line shows that the OER involves the formation of a peroxide (MOH) intermediate, while the blue line demonstrates the direct reaction of two adjacent oxo (MO) intermediates to produce oxygen gas.

### 2.3 ZIF-67 and ZIF-8

In order to minimize the dosage of noble metal Pt and maximize the surface area (active sites) of electrocatalysts; zeolite imidazole frameworks are therefore applied. ZIF-8 and ZIF-67 are the first choices, due to their simplicity of synthesis, low-cost precursors and the existence of highly electroconductive Zn or Co metals that benefit the electrons transfer during HER (Figure 2.3a).<sup>16</sup>

Zeolitic imidazolate frameworks (ZIFs) are a subclass of metal organic frameworks (MOFs, also known as porous coordination polymers). ZIFs are also a class of porous crystals constructed from tetrahedral transition metal ions such as Zn and Co based on their linkage to imidazolate (Im). As shown in Figure 2.3b, imidazolate displays a conjugate structure that gives a high electron density that may enhance electron transfer and conductivity. The synthesis procedure for ZIF-67 and ZIF-8 from 2-methylimidazole is illustrated in the experimental section later.

In these ZIFs, the M-Im-M (M = metal) angle approaches  $145^\circ$ , giving them tetrahedral morphology. Notably, ZIFs exhibit permanent porosity, as well as high thermal and chemical stability, which make them attractive candidates for many applications such as substrate, gas separation and particularly, as the growth template for carbon-based materials. In comparison to the other MOFs, ZIFs share many rich elements of zeolite chemistry in terms of both structural topologies and coordination factors. In addition, they exhibit exceptional thermal and chemical stability due to the fact that a cage-form to encapsulate the central reactive transition metal.<sup>17</sup> Although reactive nitrogen atoms exist in the imidazolate linker (Figure 2.3b), the extra lone pair of nitrogen atoms are stabilised by the five-membered ring.

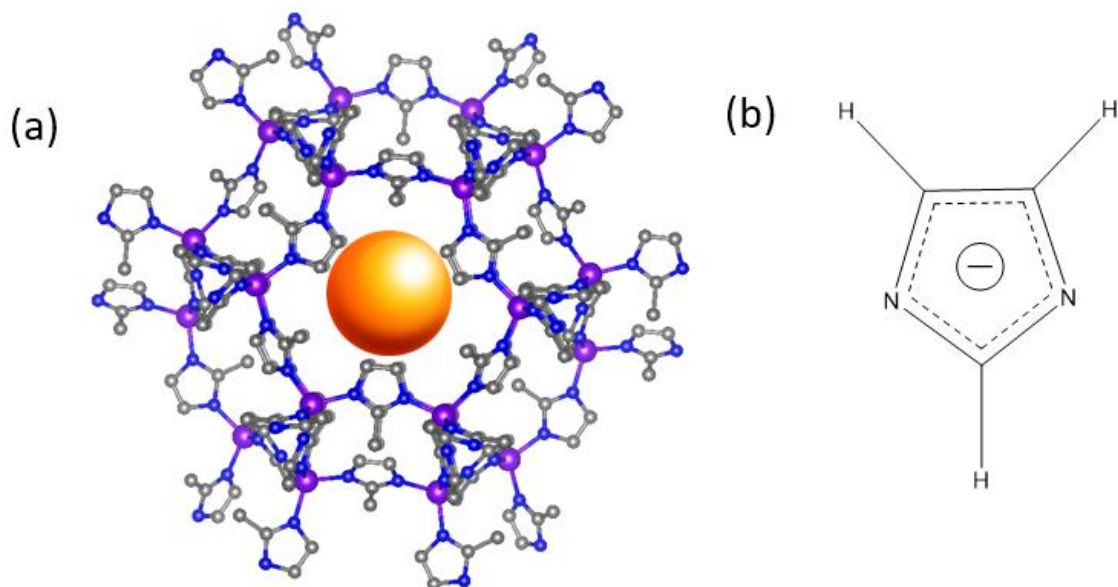
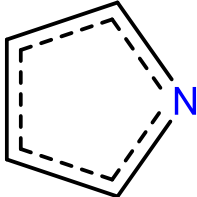
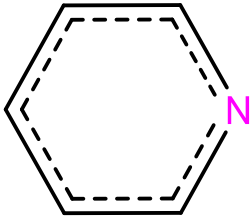


Figure 2. 3 (a) 3D structure of ZIF-67/ZIF-8 (grey ball = carbon atom, blue ball = nitrogen atom, purple ball = cobalt/zinc atom). (b) Molecular structure of imidazolate.

Both ZIF-67 and ZIF-8 demonstrate the same permanent porosity of 58.8% (Table 2.2) and their surface areas are  $1,320 \text{ m}^2\text{g}^{-1}$  and  $1,810 \text{ m}^2\text{g}^{-1}$ , respectively. The surface areas are an order of magnitude higher than that of the 20 wt.% Pt/C catalyst, which is only in the range of 10 to  $200 \text{ m}^2\text{g}^{-1}$ .<sup>18</sup> The extremely high stability, porosity, and surface areas of ZIF-67 and ZIF-8 make these the best candidates for creating the template to maximize the distribution of Pt nanoparticles, improving reactivity and increasing the number of active sites on the catalyst. Carbonization is an effective technique of removing unwanted functional groups from the ZIF structures to achieve graphitic carbon support and electric conductivity. During high temperature carbonization over  $1000 \text{ }^\circ\text{C}$ , the purity exceeds 90% and the yield can

be lower than 50%. If the carbonization temperature exceeds 900 °C, the central metal zinc in ZIF-8 is virtually released, as the boiling point of zinc is 907 °C<sup>19</sup> yet cobalt (boiling point is 2927 °C)<sup>20</sup> still remains. It is therefore important to determine the correct balance. Both substances feature the key properties of high electric conductivity and surface area, making them ideal catalysts for HER, whilst at relatively low cost in comparison with commercial 20 wt.% Pt/C catalysts. Central metal cobalt in ZIF-67 also provides the enhancement of conductivity. The ZIF-67 and ZIF-8 share the same crystalline structure with the only difference in the linkage atom, Co and Zn, respectively (Figure 2.3).

Table 2. 2 Average bond length of C-N in pyrrole and pyridine.<sup>21</sup>

Chemical class	Structural formula	Average C-N bond length (Å)
Pyrrole		1.372
Pyridine		1.337

## 2.4 Electrocatalysts for hydrogen evolution reaction

### 2.4.1 Noble metal based electrocatalysts

The noble metals are ruthenium, rhodium, osmium, iridium, palladium, platinum, silver and gold. Because of their low scarcity and high stability in the standard pressure and temperature, they are not suitable for large-scale manufacture in both labs and industries.

So far, precious metals (such as Pt and Pd) and their alloys are still the most widely used as active HER electrocatalysts, however the scarcity



and high price of noble metals greatly increases the cost of these catalysts. As a result, intensive studies have focused on the development of low-cost alternatives to noble metal-based catalysts. Nevertheless, another opinion states that the scarcity of Pt elements in commercial HER catalysts (20 wt.% Pt/C) is not as serious as expected.<sup>22</sup> On the contrary, many non-noble or metal-free catalysts, such as cobalt-based, nickel-based, molybdenum (Mo)-based and graphene oxide (GO)-based materials,<sup>23-27</sup> may be more scarce. This is not only because they need a higher quantity of catalyst loading to achieve the same current density as using a Pt-based catalyst, but also because the cost of time and reactants in the synthesis procedures will be even higher. For instance, GO-based catalysts are costly. GO itself has a high price; the unit price of GO is even higher than that a unit of the same quantity of Pt. In addition, strong acids, such as concentrated sulfuric acid and concentrated nitric acid, are used in the synthesis process, which can cause additional environmental pollution. However, the construction of noble-metal based heterostructures can further explore the activity limitation and make noble-metal based catalysts cheaper.

A simple strategy is to reduce the loading noble metals, such as Pt but to maintain the high activity and stability of the catalyst. In previous studies, several methods have been proposed. One of which is to dope Pt into fine structure in order to maximize the exposure of the active site.<sup>28,29</sup> Tang et al. synthesized an electrocatalyst, platinum nanowires grown on monolayer nickel hydroxide, Pt NWs/SL-Ni(OH)<sub>2</sub>, and the properties of HER were similar to those of commercial 20 wt.% Pt/C.<sup>30</sup>

Yet the synthesis method requires huge amount of time and cost. Another approach is to replace noble metals with relative cheap transition metals.  $\text{Ni}_5\text{P}_4$  and its related phosphorus compounds have reasonable HER properties.<sup>31</sup> Nonetheless, massive amounts of hydrogen gas is utilized during the annealing process, which conflicts with the initial purpose of hydrogen manufacture from water splitting. Recently, nitrogen-doped graphene with a small quantity of transition metal clusters has also given satisfactory HER activity, as nitrogen can induce active sites, but HER activity is much lower in comparison with the use of 20 wt.% Pt/C and, the Tafel slope is 2.6 times smaller than that of the commercial catalyst.<sup>32</sup>

#### **2.4.2 Non-noble transition metal based electrocatalysts (Ni, Fe, Co and Mo)**

##### **Ni-based catalysts for hydrogen evolution reaction**

Nickel (Ni) is an earth-abundant transition metal with the presence in the earth's crust of more than 50 ppm.<sup>33</sup> Moreover, the high corrosion-resistance and large quantity of Ni makes it one of the best candidates for HER substrates. The preparation of nanostructured Ni can enhance the stability and activity of HER through the hydrothermal process.<sup>34</sup> Also, after the hydrothermal treatment, Ni nanoparticles contain a great deal of branches, which provides rich active sites and may also enhance their high stability and activity against HER.

The activity and stability for HER can be enhanced by preparing

nanostructured Ni-rGO (reduced graphene oxide) composite (at Ni foam) by the supergravity electrodeposition method.<sup>35</sup> In comparison with the traditional electrodeposition method, supergravity electrodeposition can prevent the aggregation of Ni nanoparticles and rGO by refining Ni particles, thus promoting the surface area of the composite catalyst, which consequently results in more active sites during hydrogen evolution. Furthermore, the interfacial bonding strength between the composites of Ni nanoparticles and rGO sheets increase significantly due of the higher potential in comparison with the normal electrodeposition method. This is helpful improving the activity, conductivity and stability of the Ni-rGO electrocatalyst in the hydrogen evolution reaction.

Chung et al. synthesised nickel sulphide nanoparticles that showed a high electrocatalytic activity and durability for HER in acidic and alkaline media.<sup>36</sup> Both NiS and Ni<sub>3</sub>S<sub>2</sub> were manufactured by reflux reaction. Reflux at high temperatures (280 °C for NiS and 250 °C for Ni<sub>3</sub>S<sub>2</sub>) can produce the better mixing of reactants compared with hydrothermal methods, since magnetic stirring takes place in the former. The small surface of nanoparticles engineering used to control nickel sulphide can provide a good candidate as a water electrolysis catalyst. In terms of the activity of catalysts, NiS has a higher value than Ni<sub>3</sub>S<sub>2</sub> because of its strong affinity to hydrogen, which is proved both in experiment and DFT theory.

### **Fe-based catalysts for hydrogen evolution reaction**

Iron (Fe) is a transition metal that is widely abundant in the earth's surface. Fe is the fourth most common element in the earth's crust (abundance: > 6.3%).<sup>37</sup> Therefore, Fe-based electrocatalysts are a promising option for the development of inexpensive water-decomposition electrocatalysts because the lower price of iron-based materials is much lower. For instance, stainless steel costs £32 per square metre, which is much cheaper than carbon cloth (£690 per square metre) and nickel foam (≈£79 per square metre).<sup>38</sup> Therefore, significant effort and financial resources have been invested in the development of Fe-based electrocatalysts for the HER reaction.

Electronegative elements such as N and P dual-doping on Fe-based catalysts can enhance both stability and activity for HER. Liu et al. have observed that FeP/NCNT (an N-doped carbon nanotube supported by FeP nanocomposites) prepared by a one-step low-temperature phosphidation reaction has demonstrated excellent HER properties.<sup>39</sup> FeP/NCNT only needs overpotentials of 113 and 195 mV to achieve current densities of 10 and 100 mA cm<sup>-2</sup> respectively.

Likewise, Yang et al. found that FeCo alloy nanoparticles encapsulated in highly N-doped (8.2 atom%) graphene layers showed an overpotential of only 262 mV at 10 mA cm<sup>-2</sup>.<sup>40</sup> This catalyst was synthesised by the direct carbonisation of MOF with Fe/Co metal centres. After annealing, nitrogen-doped graphene layers formed to prevent corrosion from the acidic electrolyte and protect the centre metals, which are the active sites for the HER. Thus, the catalyst gave a promising performance, especially in long-term stability, as it

neglected stability loss after 10,000 cyclic voltammetry (CV) cycles. DFT theory calculation indicates that these excellent HER properties originated from the proper quantity of N-dopants, since N-dopants increase the H\* adsorption sites, which further enhances HER activity.

### **Co-based catalysts for hydrogen evolution reaction**

In terms of an HER catalyst with Co as the substrate, doping with a strong electronegativity element, such as phosphorus, in order to prepare the nanostructure of CoP, can boost the activity of the HER. Liu et al. synthesised a catalyst of CoP-decorated carbon nanotubes (CoP/CNT).<sup>41</sup> During preparation, the precursor Co<sub>3</sub>O<sub>4</sub>/CNT hybrid was formed by a hydrothermal method at 150 °C for 3 hours, followed by washing it with ethanol and deionised water. After that, a low-temperature phosphidation at 300 °C for 2 hours was carried out in order to produce the final CoP/CNT. This acid-stable nanohybrid exhibits an extraordinary HER activity in 0.5 M H<sub>2</sub>SO<sub>4</sub> electrolyte, with a small onset overpotential of 40 mV and a Tafel slope of 54 mV dec<sup>-1</sup>. Likewise, Xu et al. observed that CoP NWs/ CoOx has high activity and stability for HER.<sup>42</sup> The synthesis procedure is quite similar to that of CoP/CNT. A hydrothermal method at 120 °C for 12 hours is followed by subsequent low-temperature phosphorization at 100 °C for 10 minutes and then 320 °C for 2 hours under an argon (Ar) atmosphere. Finally, CoP NWs/CoOx was obtained by an oxygen plasma engraving treatment. The nanowire (with diameter ≈3 nm) morphology provides abundant active sites with which to increase activity (overpotential of -

65 mV at  $-10 \text{ mA cm}^{-2}$ ) and durability (a negligible decay at  $-10 \text{ mA cm}^{-2}$  after 5000 cycles of CV) in 1.0 M KOH.

### **Mo-based catalysts for hydrogen evolution reaction**

Mo-based electrocatalysts are another excellent candidate for HER since the various of Mo oxidation states provide electron vacancies for element doping. Datta et al. proved that oxygen doping in Mo-based materials creates defects with which to enhance the HER performance and stability.<sup>43</sup> Catalysts named as oxygen-deficient 2D  $\alpha\text{-MoO}_{3-x}$  nanosheets ( $x = 0.045$ ) have been successfully synthesised by liquid phase exfoliation. On average, sheets were made of 6 layers with dimensions of  $\approx 125 \text{ nm}$  to give low overpotential (142 mV at the current density of  $10 \text{ mA cm}^{-2}$ ), fast electron transfer ( $58 \text{ mV dec}^{-1}$ ) and high stability (negligible activity loss in 4 hours).

Except for the oxygen doping, introducing sulfur into molybdenum phosphide (MoP) produces a molybdenum phosphosulfide (MoP|S) catalyst with great HER activity and stability in 0.5 M  $\text{H}_2\text{SO}_4$ .<sup>44</sup> The mixed-anion catalyst with synergistic effects (sulfur and phosphorus doping) provides a high-surface-area electrode, resulting in a superior HER activity and stability by a two-step pyrolysis method. Initially, MoP was formed by reduction and calcination at  $650 \text{ }^\circ\text{C}$  under a forming gas mixture of 5%|95%  $\text{H}_2$ | $\text{N}_2$  in a quartz tube furnace. Next, (MoP|S) was prepared by post-sulfidation of the supported MoP in a quartz tube furnace at  $400 \text{ }^\circ\text{C}$  flowing under a mixture of 10%|90%  $\text{H}_2\text{S}$ | $\text{H}_2$  gas. As a result, MoP|S demonstrates excellent HER properties with an

overpotential of 64 mV at 10 mA cm<sup>-2</sup> and Tafel slope of 50 mV dec<sup>-1</sup>.

Transition metal carbides show significant catalytic activity because they have similar electronic and catalytic properties to Pt-based HER catalysts.<sup>45, 46</sup> For instance, nanoporous molybdenum carbide nanowires (np-Mo<sub>2</sub>C NWs) have been manufactured and provide a remarkable HER properties due to its large surface area and dispersed wires.<sup>47</sup> The np-Mo<sub>2</sub>C NWs was synthesized by a simple one-step calcination procedure with a MoO<sub>x</sub>/amine hybrid precursor under 725 °C for 5 hours in an argon inert atmosphere. The carbonized product gives a high value of nanoporosity and nanowires, which are the reinforced support for the superb HER activity with low overpotential (current densities of 80 mA cm<sup>-2</sup>, at an overpotential of 200 mV), a Tafel slope (60 mV dec<sup>-1</sup>) and high durability (negligible change over 24 hours) in 0.5 M H<sub>2</sub>SO<sub>4</sub>.

### **2.4.3 Metal-free carbon materials**

According to the literature listed in the sections above, nanocarbon materials, such as graphene, carbon nanotube or pyrolyzed ZIF, are usually selected to support HER nanocatalysts in order to enhance performance (promote activity and stability, reduce overpotential). Typically, in these cases, carbon nanoparticles can provide nanocatalyst-preferred structural support (for example, a large surface area or the dispersion of metal particles to maximise the quantity of active sites) or synergistic effects (for instance, accelerated electron transfer) or both. However, these nanocarbon materials are essentially

HER-inert since carbon is intrinsically HER-inert. In this section, a new class of HER catalysts, heteroatom-doped nanocarbons will be introduced.<sup>48, 49</sup> The basic difference between the carbon material substrate and the conventional metal-based catalyst material substrate is that the catalytically active site of nanocarbon catalyst does not involve metal ions. The attraction of a carbon-based "unconventional" HER catalyst mainly comes from the cheap and excellent physical and chemical properties of carbon materials (for example, high chemical and high thermal stability).

Heteroatom-doping can adjust the structure of carbon material and then cause the inactive pristine nanocarbon materials to become a highly active state (for HER). However, atom-introduction might lead to the creation of defects in order to optimise the chemical and physical properties of carbon-based catalysts. In other words, the addition of active sites promotes the activity and stability of nanocarbon HER catalysts. A heteroatom-doped graphene-based HER catalyst is an excellent example.

Dai et al. reported N, P and F tri-doped graphene metal-free electrocatalysts for HER.<sup>50</sup> The desired product underwent pyrolysis of polyaniline (PANi)-coated graphene oxide (GO-PANi) in the presence of ammonium hexafluorophosphate (AHF) at 950 °C for 1 hour. The high-temperature annealing procedure of AHF could not only provide heteroatom sources for tri-doping with N, P and F to give the defects for active sites, but also form porous structures to maximise the surface area. In order to find out the relationship between the electronic



properties of doped graphene catalysts and non-metallic dopants with similar electronegativities (N, B, O, S, P, F), it is necessary to carry out DFT theoretical calculations.<sup>51</sup> The heteroatoms act as the active sites in the electrocatalyst for HER. In Figure 4a, the natural bond orbital population analysis results show that N and O are negatively charged when they are adjacent to carbon. Therefore, Qiao et al. selected N and P co-doped graphene (with the relatively largest electronegativity difference) to tailor the electron acceptor-donor property and activate the adjacent C to provide the best-performing HER electrocatalyst. As expected, N-P graphene demonstrated the best H\* adsorption-desorption property ( $\Delta G_{H^*}$  is closest to zero) by correlating graphene's valence orbital energy (Figure 2.4b, c).

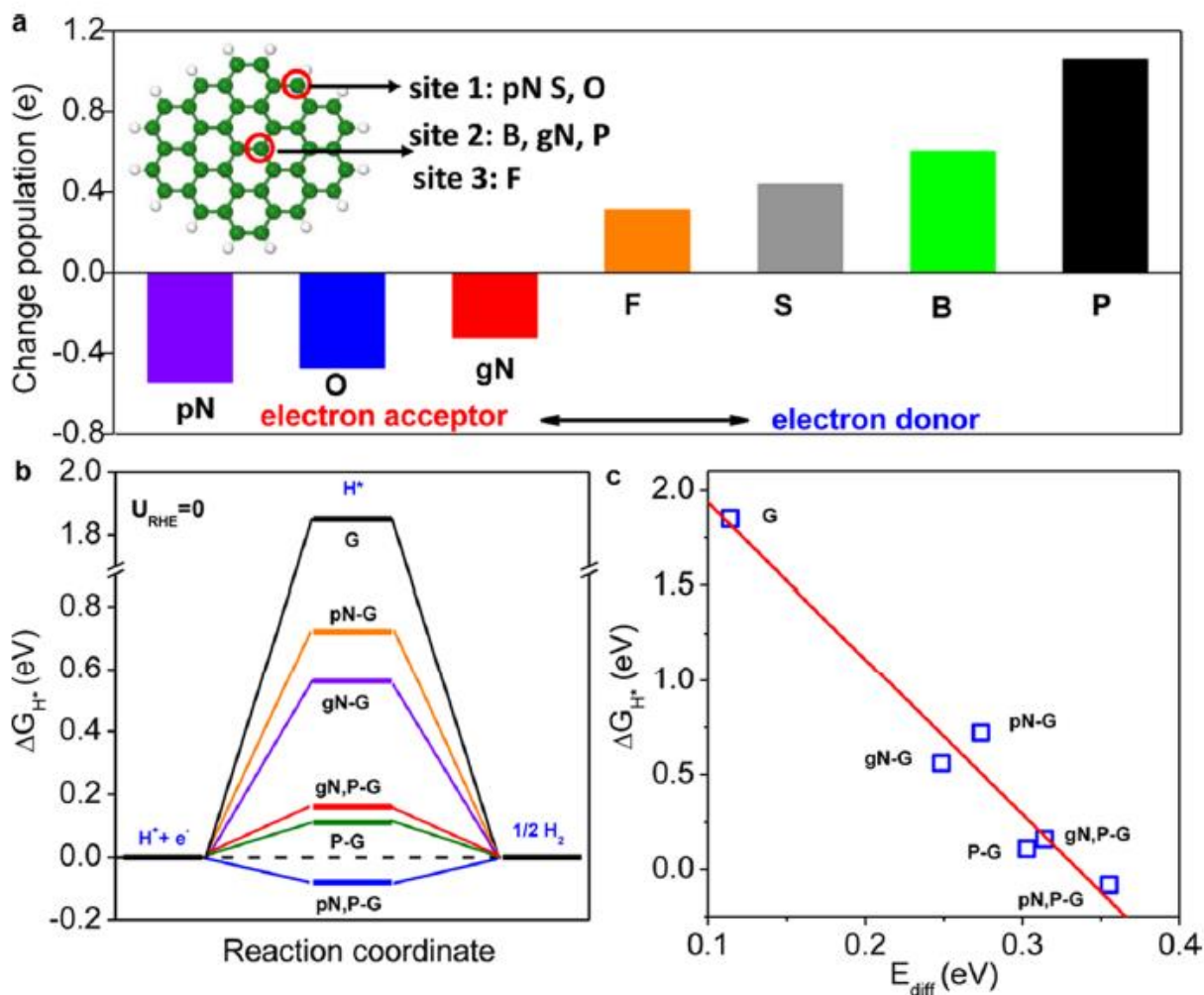


Figure 2. 4 (a) Natural bond orbital (NBO) population analysis of six different nonmetallic heteroatoms in graphene matrix. pN and gN represent pyridinic and graphitic type of N, respectively. Inset shows the proposed doping sites for different elements, sites 1 and 2 are the edge and center in-plane sites, respectively, and site 3 is an out-of-plane center site in graphene. (b) The calculated free energy ( $\Delta G_{H^+}$ ) diagram for HER at the equilibrium potential ( $U_{RHE} = 0$  V) for N- and/or P-doped graphene models. (c) Relationship between  $\Delta G_{H^+}$  and  $E_{diff}$ <sup>51</sup> Reprinted with permission from ref. 51.

In addition to graphene-based catalysts, heteroatom-doped carbon nanotubes have also been found to be effective HER catalysts. Qiao et al. prepared a polydopamine (PDA)-assisted N,S-codoping carbon nanotube (N,S-CNT) by a two-step “graft-and-pyrolyze” route.<sup>52</sup> In detail, PDA acted as the support to provide the source of nitrogen and sulfur elements to construct a multiple heteroatom-doped carbon nanotube for HER, since PDA is extremely reactive to thiol groups via a Schiff-base reaction in room temperature.<sup>53</sup> After chemically grafted with the thiol groups, pyrolysis took place at 400 °C then 700 °C, and the homogeneous product was derived from relatively high S-doping efficiency (5.6 at%). As a result, the PDA assisted N, S-CNT shows superior HER activity and stability in 1 M KOH. The authors also used DFT calculations to reveal the reason for the activity boost due to the N and S doping. The secondary S-doping brought in the formation of catalytically active sites and enhanced the charge transfer of the carbon material support (CNT). Furthermore, Cui et al. also proved that HER inert pristine carbon nanotubes could be activated by via acidic oxidation and subsequent cathodic pretreatment as a novel acid stable metal-free HER electrocatalyst with high performance.<sup>54</sup> The authors also discovered that the HER performance was in close correlated with the quantity of surface acidic groups (-COOH), since cathodic polarisation can lead to an increase of the -COOH group on the multi-walled carbon nanotube.

All the literatures listed above indicated that transition metal doped on carbon supports, especially for zeolite imidazolate framework compounds are promising cost-effective precursors when designing

and developing metal-incorporated carbon electrocatalysts. The design concept of these electrocatalysts from ZIFs could be extended to develop other novel, effective and stable catalyst systems whatever in fuel cells, hydrogen-powered vehicles or further advanced applications.

## Chapter 3. Aim/Research Plan

It is the primary intention of this project to investigate and develop highly efficient (kinetics), stable and cost-effective HER electrocatalysts. As one of the most sustainable sources of energy, hydrogen can be widely implemented for use in fuel cells. It is also of great interest and value in the field of research on sustainable energy. Based on the previous literature reviews, it is apparent that the transition metals (Pt, Ni, Fe, Co and Mo, etc.) doped zeolite imidazolate frameworks (ZIF), and the high-temperature carbonization pathway is an effective pathway by which to synthesize active and stable HER electrocatalysts.<sup>22,30,35,42-53</sup> However, it is desirable to rationally design electrocatalytic performance by optimizing structure / morphology, adjusting the carbon matrix (porosity and surface area), and the degree of interaction between the transition metal nanoparticles and/or the carbon supports. The synergistic effect of the resulting catalysts for HER is a crucial part in mechanism research. However, this research and synthetic strategy is still in its infancy. It is well known that synthetic methods can greatly modify the structure of the material and that of the support to eventually affect the performance of the catalyst. As a simple and effective technique, pyrolysis will frequently be used to prepare transition metals which are anchored on functionalized carbon substrates. The functionalization of the carbon substrates is a further key for the introduction of anchoring metal centers in order to control the growth of yielded electrocatalysts. Therefore, the study of pyrolysis with different temperatures and durations has been applied in order to

investigate the correlation between the degree of carbonization, metal cluster size, porosity, surface area and the carbon substrate for the final performance of the catalysts in HER.

Throughout this study, a number of different characterization techniques were implemented in order to determine the structure of the catalysts to derive its performance and its mechanism in HER. For structural characterizations, scanning electron microscopy, transition electron microscopy and atomic force microscopy (SEM, TEM and AFM respectively) generate information regarding the chemical composition and the external morphology of the samples. X-ray photoelectron spectroscopy (XPS) quantitatively measures the chemical state, electronic state and the surface composition of materials (external) unless depth profile technique is carried out (internal); powder X-ray diffraction (PXRD) determines the atomic and crystalline structure of catalysts; Raman spectroscopy identifies the graphitic characteristics of carbonized products and the exact content of Pt was measured by microwave plasma atomic emission spectroscopy (Agilent 4210 MP-AES). For electrochemical characterizations, cyclic voltammetry (CV), linear sweep voltammetry (LSV) and chronoamperometry (CA) will be used to evaluate the electrocatalytic performance, stability and relative mechanism study in a three-electrode cell. A glassy carbon rotating disk will be employed as the working electrode with a carbon rod and Ag/AgCl/saturated KCl as the counter and reference electrode.

## Chapter 4. Carbonized Platinum@ZIF-67 or ZIF-8 as High Performance Electrocatalysts for Hydrogen Evolution Reaction

### 4.1 Introduction

Clean and sustainable energy sources are highly desirable for the reduction of carbon dioxide emission and reliance on polluting fossil fuels. Hydrogen is an ideal choice due to its elemental abundance, high energy density per unit mass ( $143 \text{ kJ g}^{-1}$ )<sup>55</sup> and zero carbon emission at point of use. Industrial hydrogen production is undertaken by steam methane reforming and coal gasification, where  $\text{CO}_2$  emission persists unless effective  $\text{CO}_2$  capture is implemented, whereas, electrocatalytic water-splitting, e.g. using off-peak electricity, offers cost-effective potential to produce hydrogen (Table 2.1). The commercial Vulcan XC72 platinum on carbon (20 wt.% Pt/C) is still the benchmark catalyst for the hydrogen evolution reaction (HER) as it requires a very small overpotential. However, the noble-metal catalyst is rather costly and is prone to detachment from the carbon support in cycling. Thus, it is very desirable to develop low-cost, highly efficient and stable alternatives for HER.<sup>56-58</sup>

One straightforward strategy is to lower the Pt loading but preserve its performance. Several approaches have been proposed in the past, one of which is to dope Pt into fine structures to maximise Pt exposure

or active site density.<sup>59-61</sup> Tang *et al.* studied platinum nanowires grown on single-layered nickel hydroxide, Pt NWs/SL-Ni(OH)<sub>2</sub>, and show a comparable HER performance with commercial 20 wt.% Pt/C.<sup>30</sup> However, the synthesis method is arduous and time-consuming. Another approach is to adopt transition metal as alternatives to Pt. A nanocrystalline Ni<sub>5</sub>P<sub>4</sub> and its related phosphorus compounds have been reported to exhibit good HER performance.<sup>62</sup> However, these need hydrogen in the annealing procedure, which conflicts with the initial purpose of hydrogen production from water. Recently, nitrogen-doped graphene with a small amount of transition metal clusters,<sup>32,63-65</sup> has also exhibited HER activity, where nitrogen can induce active sites, but the HER activity is much lower than that of the 20 wt.% Pt/C, as the Tafel slope is more than 2.6 times larger than the commercial counterpart.<sup>32</sup>

Inspired by the above studies, zeolitic imidazolate framework (ZIF-67) (Co-2-methylimidazole) was selected as the precursor for nitrogen doped carbon skeleton,<sup>66,67</sup> the transition metal provider for anchoring Pt to minimize metal clustering via direct annealing under N<sub>2</sub> atmosphere (Figure 4.1).<sup>16,68-70</sup> The resulting encapsulated the Pt and nitrogen doped carbon framework catalysts demonstrated excellent HER activity and long-term stability, outperforming the commercial counterpart, particularly at low potential in an acidic electrolyte since ZIF-67 provided a skeletal structure for Pt to form alloy from clustering during annealing process. Moreover, Hubbard-corrected Density Functional Theory (DFT+U) simulations revealed that the free energy of the HER reaction could be dramatically tuned by the metal alloy with



different ratios inside the carbon cage. The Pt atom tended to dope at the edge positions of the Co clusters at a low concentration but then in bulk positions with increasing Pt loading, i.e. not all the Pt atoms will act as active sites in the alloy clusters. Hence, the HER performance does not increase proportionately with the Pt content in the system and dilute Pt doping can be very cost-effective in future catalyst design for HER. Our results provide not only a strategy of efficient utilization of noble metal elements in HER, but also a practical route for low-cost synthesis of such alloy catalysts. The simple synthesis procedure also offers a strong potential for industrial scale-up.

## **4.2 Experiments**

### **4.2.1 Synthesis methods**

#### Synthesis of ZIF-67

Firstly, the cobalt nitrate hexahydrate (7.185 g) was dissolved in 500 mL methanol. Then, 2-methylimidazole (8.106 g) was dissolved in another 500 mL methanol. The latter solution was slowly added to the former one in a 1 L wide mouth jar while stirring at room temperature. Stirring proceeded for 2 h and solution was then left for 24h to settle. The top clear solution was drained out and the purple precipitates were collected by centrifugation with further methanol washing. The sample was dried for 24h at 80 °C in an oven.

#### Synthesis of Pt@ZIF-67 and CPt@ZIF-67

As-synthesized ZIF-67 crystal powder (100 mg) and the chloroplatinic acid hexahydrate  $\text{H}_2\text{PtCl}_6 \cdot 6\text{H}_2\text{O}$  (26 mg) were added into methanol (20 mL). Sonication and stirring was carried out for 1 h to get a homogenous ink solution. Pt coated ZIF-67 (Pt@ZIF-67) was obtained by ground the purple solid into fine powder after evaporating the methanol in oven at 80 °C for 24 hours. Then, the product was carbonized at 900 °C in an alumina boat (1 × 1.5 × 5 cm) after transfer into a horizontal tube furnace to form carbonized ZIF-67 with Pt doping, namely CPt@ZIF-67. The temperature was increased to 900 °C with a heating rate of 5 °C min<sup>-1</sup>. Then, the powders were annealed at 900 °C for 6 hours under nitrogen and cooled down to room temperature. After carbonization, black solids were collected and ground into fine powder. To optimize the carbonization procedure, the samples synthesized at different temperatures and durations were also carried out, namely CPt@ZIF-67-x°C-y h (x and y represents the temperature and duration of the carbonization).

#### **4.2.2 Physical characterization**

Powder X-ray diffraction (PXRD, on Stoe Stadi-P, Cu-K-alpha and Mo-K-alpha) was carried out by encapsulation of samples in a 0.5 mm diameter borosilicate glass capillary under ambient conditions. X-ray photoelectron spectroscopy (XPS, on Al-K-alpha, Thermo Scientific), and scanning electron microscopy (SEM, Jeol) were carried out on the carbon tape. Transmission electron microscopy (TEM, Jeol) measurements were carried out on a carbon coated copper TEM grid

support. Raman spectroscopy (514.5 nm laser, Renishaw) was carried out with powder samples on a glass slide. Atomic force microscopy measurements were carried out in AC mode using silicon rectangular-shaped cantilevers with a tip curvature radius about 6 nm and a force constant of 40 N m<sup>-1</sup>. The test samples were prepared by dip-coating the materials on clean silicon substrate. (AFM, Keysight 5600LS). The content of Pt was measured by microwave plasma atomic emission spectroscopy (Agilent 4210 MP-AES).

### **4.2.3 Electrochemical test**

All the tests were carried out using an Autolab (Metrohm PGSTAT302N) electrochemical station, by a three-electrode method with a glassy carbon rotating disk as the working electrode, carbon rod and Ag/AgCl/saturated KCl as counter and reference electrodes, in an acidic electrolyte (0.5 M H<sub>2</sub>SO<sub>4</sub>) at room temperature. All the measurements were carried out with a fixed catalyst deposition of ~0.26 mg cm<sup>-2</sup> on a 3 mm diameter (or area of 0.0707 cm<sup>2</sup>) glassy carbon disk electrode. The catalyst was prepared as follows: 2 mg of sample was dispersed in a total 540 μL solution consisting 500 μL of 4:1 v/v water/ethanol and 40 μL of Nafion (5% solution) under sonication. The sonication was carried out up to an hour to get uniform catalyst dispersion ink, of which 5 μL was micropipetted and dropped on to a glassy carbon disk electrode followed by drying at 60 °C in the oven prior to the electrochemical tests. All the electrochemical test results were reported with respect to the reference, Ag/AgCl. The linear sweep voltammetry (LSV) curves were recorded with a voltage

sweeping at 10 mV s<sup>-1</sup> in the potential range of +0.0 V to -0.7 V with disk rotating speed in 1600 rpm in 0.5 M H<sub>2</sub>SO<sub>4</sub>. The data were collected after stable CVs were obtained. The measured potentials against Ag/AgCl were converted to RHE using the following relation. In 0.5M H<sub>2</sub>SO<sub>4</sub>,  $E_{(RHE)} = E_{Ag/AgCl} + 0.059 \text{ pH} + E^{\circ}_{Ag/AgCl}$ , where  $E^{\circ}_{Ag/AgCl} = 0.1976 \text{ V}$  at 25 °C and  $E_{Ag/AgCl}$  is the working potential. The overpotential  $E = E_{(RHE)}$ .

#### 4.2.4 Density Functional Theory (DFT) simulations

All the calculations were carried out based on Density Functional Theory, implanted in Vienna *ab-initio* Package (VASP).<sup>71, 72</sup> The Perdew-Burke-Ernzerhof (PBE) functional<sup>73</sup> for the exchange-correlation term was used with the projector augmented wave method.<sup>74,75</sup> A plane wave cutoff of 500 eV with forces converged to 0.01 eV/Å. Considering the cobalt carbon interaction, on-site Hubbard  $U$  corrections, 3.3, were selected for the Co delocalized d electrons, which has been assessed in the past.<sup>76, 77</sup> Spin polarization was counted in all the calculations. Gamma only was selected for the K-point sampling.

The free energies of the intermediates were obtained by

$$\Delta G(H^*) = \Delta E(H^*) + \Delta ZPE - T\Delta S$$

where  $\Delta E(H^*)$  is the adsorption energy calculated by

$$\Delta E(H^*) = E_{H@core-shell} - E_{core-shell} - \frac{1}{2} E_{H_2}$$

$\Delta ZPE$  is the zero-point energy change, and  $\Delta S$  is the entropy change of adsorption H. All the analysis within DFT scope were using normal-

mode analysis, proposed by Nørskov.<sup>78</sup>

$$\Delta ZPE(H^*) = ZPE(H^*) - \frac{1}{2}ZPE(H_2)$$

where,  $ZPE(H_2)$  is 0.27 eV.<sup>79</sup> Since the vibration frequency of H is less than 1 meV,  $\Delta S = S(H^*) - 0.5S(H_2) \approx -0.5S(H_2)$ . For  $H_2$  at 300K and 1 atm,  $TS(H_2) = 0.41$  eV. Then the  $T\Delta S \approx -0.2$  eV.

## 4.3 Results and Discussion

### 4.3.1 Morphology and composition

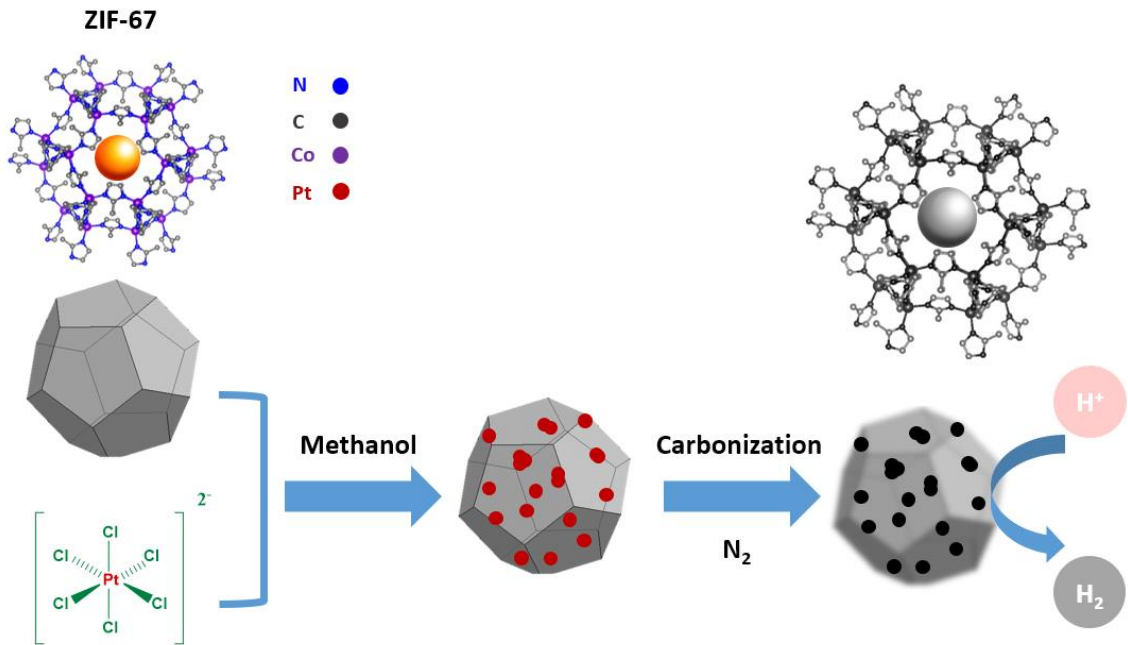


Figure 4. 1 Illustration of the synthesis procedures of carbon encapsulated Pt-doped alloys embedded in the nitrogen-doped carbon framework.

Carbon encapsulated Pt alloy carbon network, hereafter named as CPt@ZIF-67 were synthesized by a two-step approach, modified from that by Gadipelli *et al.*<sup>16</sup> Firstly, ZIF precursors and the platinum salt were completely dissolved in methanol by sonication and stirring; then, the solvent was evaporated and the as-synthesized material was annealed in an inert N<sub>2</sub> atmosphere at a given temperature to yield the final sample. For comparison, the carbonized ZIF without the Pt salt was also prepared, denoted as CZIF-67. The procedures were illustrated in Figure 4.1 and detailed in the Experimental section.

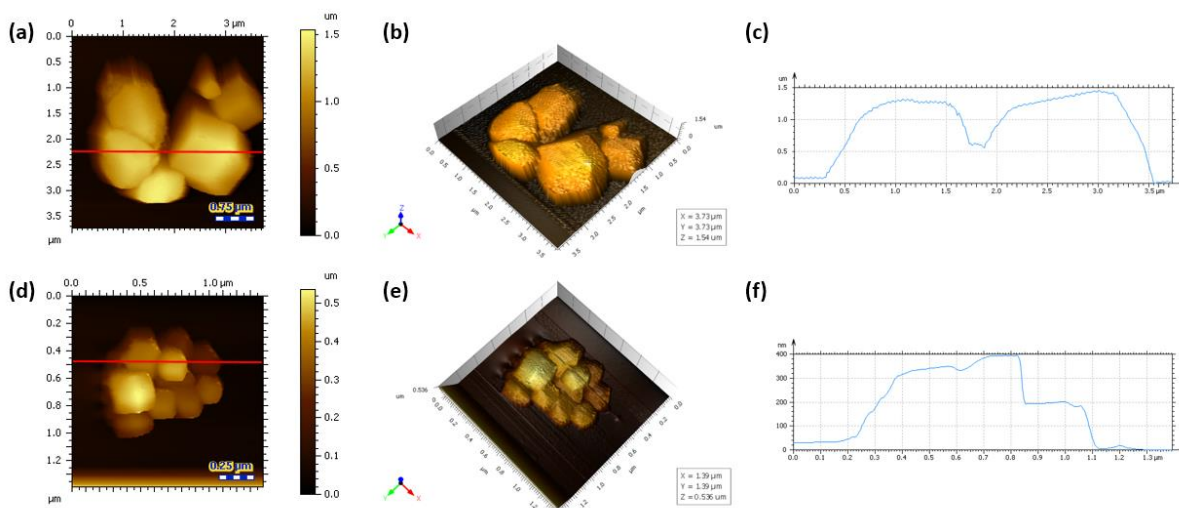


Figure 4. 2 (a) AFM image of Pt@ZIF-67. (b) 3D morphology of Pt@ZIF-67. (c) Height profile corresponding to the red line in (a). (d) AFM image of Pt@ZIF-8. (e) 3D morphology of Pt@ZIF-8. (f) Height profile corresponding to the red line in (d).

Firstly, the carbonization temperature and duration were optimized from 600 to 1000 °C for 2 or 6 hours. These samples were denoted as CPt@ZIF-67-x-y, where the carbonization temperature in x °C and y hours. The morphology of the pre-annealing samples was studied by

AFM and SEM. Before annealing, the samples show clear polyhedral structures (Figure 4.2a-b, 4.3b and 4.4a). The AFM height profile measurements (Figure 4.2c) indicate the particle sizes of Pt@ZIF-67 can vary from 0.8 to 1.5  $\mu\text{m}$ . After annealing, the samples became amorphous (Figure 4.4). The degree of amorphization gradually increased with the increasing carbonization temperature and duration, which is in line with previous observation.<sup>80</sup> For CPt@ZIF-67-600-2 (Figure 4.4b) and CPt@ZIF-67-700-2 (Figure 4.4c), the crystalline cubic ZIF morphology became rounded in the edges. When the annealing temperature was raised to 900 °C and above, the original structure fully collapsed into an amorphous structure (Figure 4.4f-h). Hence, the optimum carbonization temperature and duration are 900 °C and 6 hours. The optimized CPt@ZIF-67-900-6 also showed effective catalysis performance with the lowest onset potential and the highest current density compared with those from other carbonization conditions, which will be illustrated later. Hence, all the samples used were the 900 °C-6h one, unless specified otherwise.

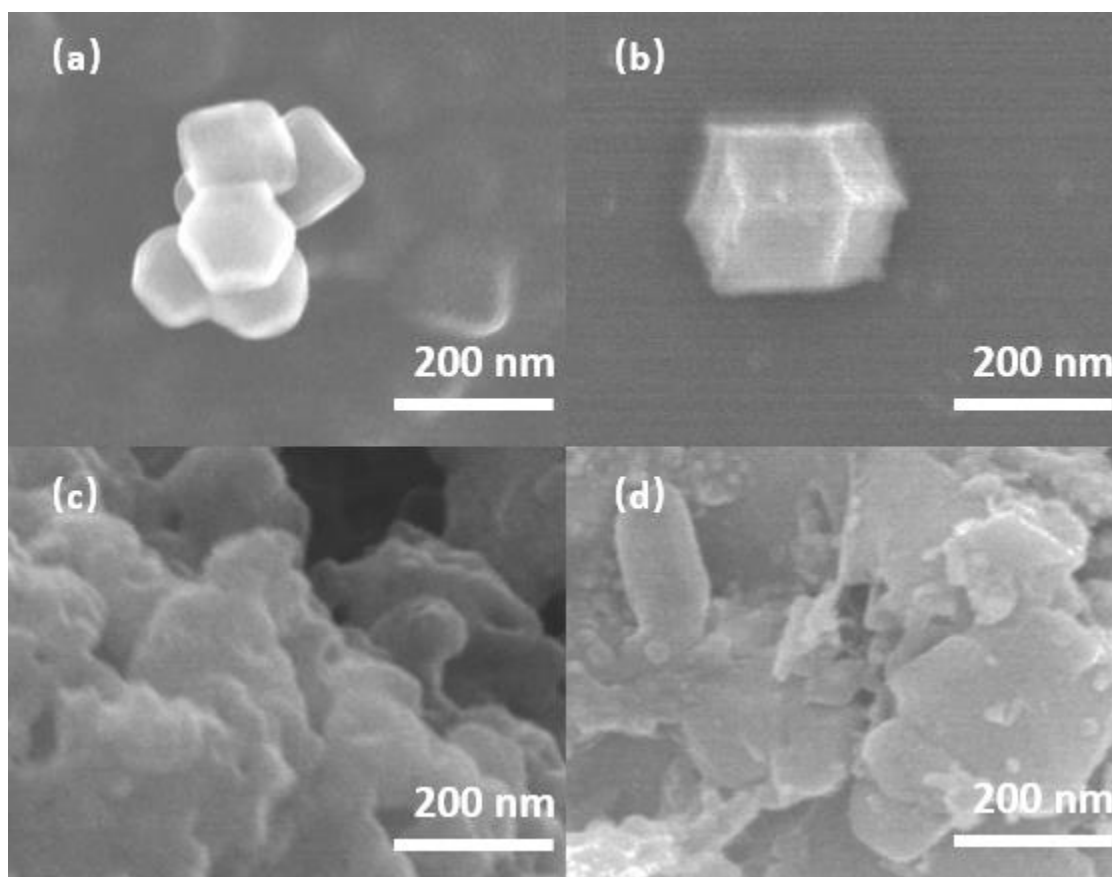


Figure 4. 3 SEM image of (a) Pt@ZIF-8, (b) Pt@ZIF-67, (c) CPt@ZIF-8, and (d) CPt@ZIF-67.



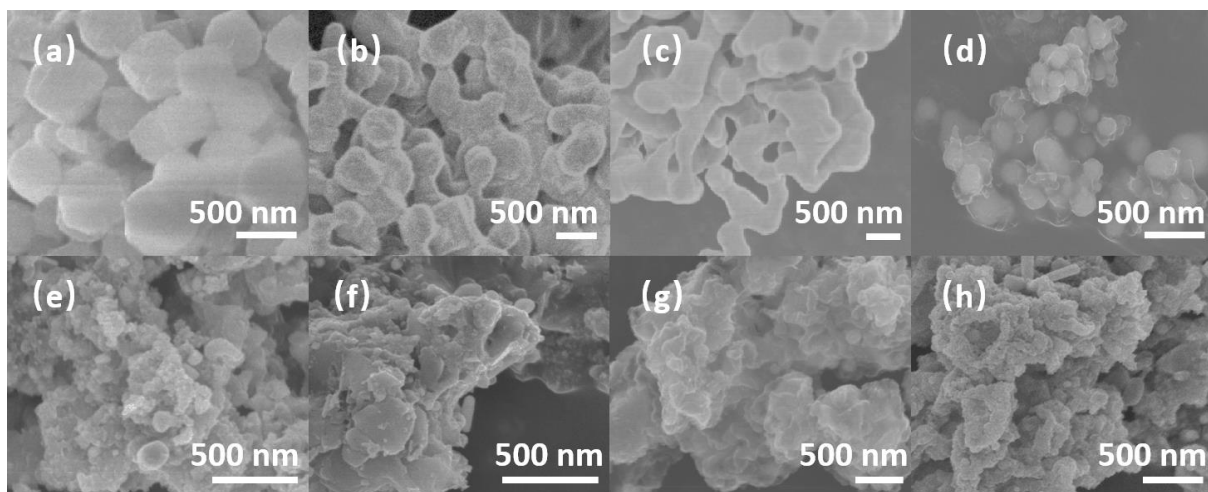


Figure 4. SEM image of (a) ZIF-67, (b) CPt@ZIF-67-600C-2h, (c) CPt@ZIF-67-700C-2h, (d) CPt@ZIF-67-800C-2h, (e) CPt@ZIF-67-900C-2h, (f) CPt@ZIF-67-900C-6h, (g) CPt@ZIF-67-900C-6h, and (h) CPt@ZIF-67-1000C-2h.

It is worthy to note that TEM characterizations of Pt@ZIF-8 and CPt@ZIF-8 show the size and density of the metal clusters in ZIF-8 in Figure 4.5a and 4.5b, respectively. Compared with the particle sizes in Figure 4.6a, the Pt cluster size has doubled after the annealing CPt@ZIF-8, which suggest that Pt only particles tends to grow during annealing, due to Ostwald ripening with kinetically limited growth.

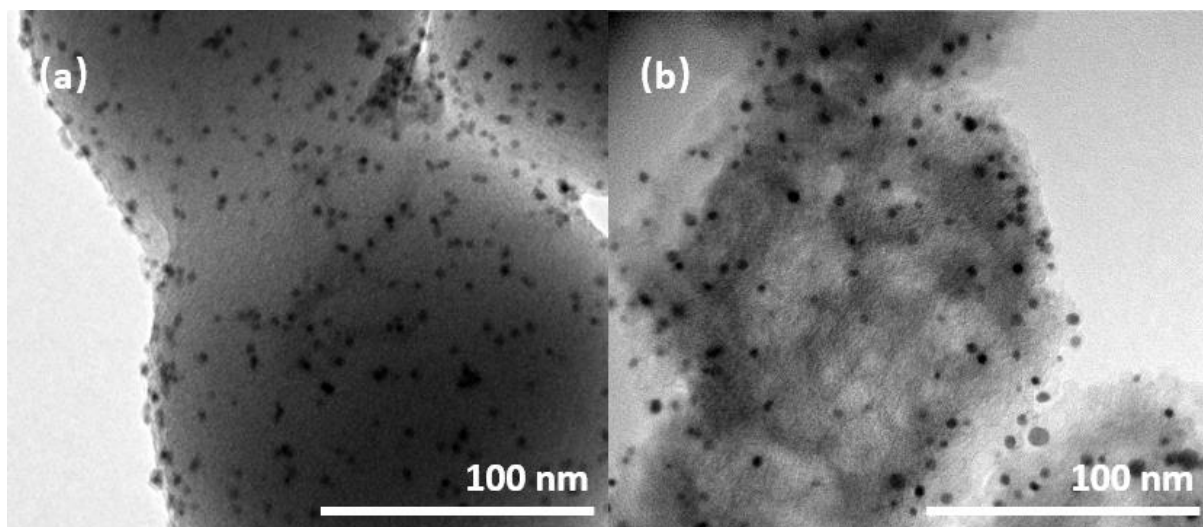


Figure 4. 5 TEM images for (a) as-synthesized Pt@ZIF-8, and (b) annealed CPt@ZIF-8.

Further TEM images (Figure 4.6a-c) show that the size of the PtCo alloy clusters in CPt@ZIF-67 is 2.7 nm in average, nearly halved the particle size (5.2 nm in average) of the commercial 20 wt.% Pt/C (Figure 4.7e). Meanwhile, the densities of the metal clusters in CPt@ZIF-67 and in 20 wt.% Pt/C were at a comparable level (Figure 4.6b and 4.7d or Figure 4.7a and 4.7e). Hence, the metal particle of our samples is in one eighth scale as the commercial one.

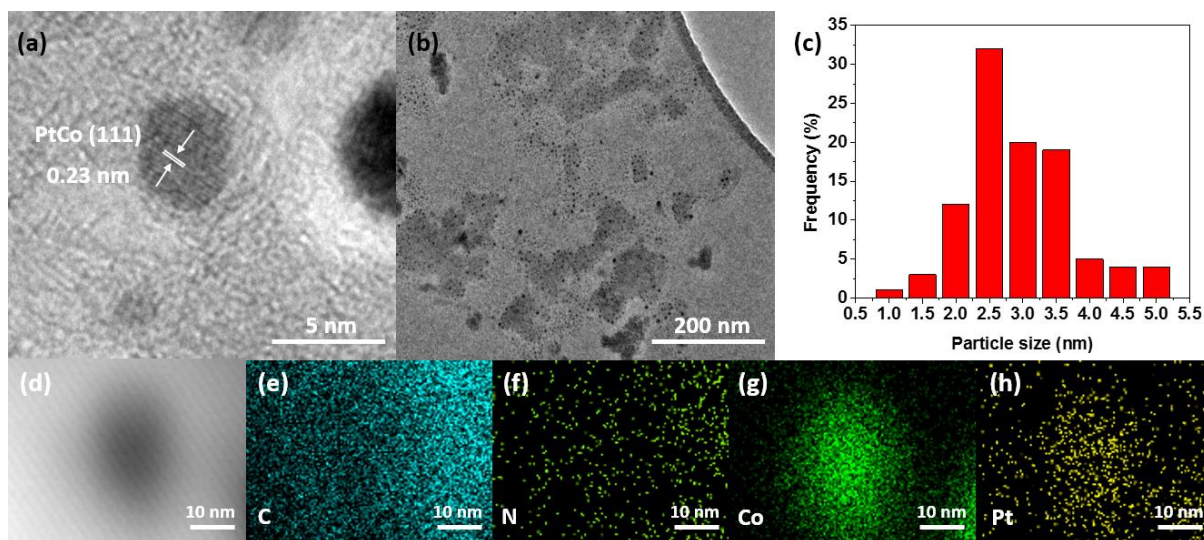


Figure 4. 6 (a) Lattice spacing of PtCo alloy clusters in CPt@ZIF-67. (b) TEM images for CPt@ZIF-67. (c) The size distribution of clusters in CPt@ZIF-67. It was analyzed by randomly selecting 100 nanoparticles to measure their diameters (average diameter = 2.7 nm). (d) TEM image of CPt@ZIF-67. Element mappings of (e) carbon, (f) nitrogen, (g) cobalt, and (h) platinum.

By tailoring of the carbonization conditions, the graphitic or graphene shell may still be structurally porous, or with varied thickness, i.e. not completely covering the whole cluster or only with one or two graphene layers, so as to allow easy access of electrolyte to the catalytic metal sites, while protecting the clusters from further growth and clustering. As a result, the catalyst is expected to be very effective and stable over a long period of service.

The high crystallinity of the PtCo alloy has been observed in Figure 4.6a, with a lattice spacing of 0.23 nm, corresponding to the PtCo(111) plane.<sup>81</sup> Elemental mapping, Figure 4.6e-h, reveals that both Pt and

Co elements distribute homogenously in the alloy. Meanwhile, the elemental mapping of the Pt@ZIF-67 (Figure 4.8) indicates that these elements are uniformly distributed even before annealing.

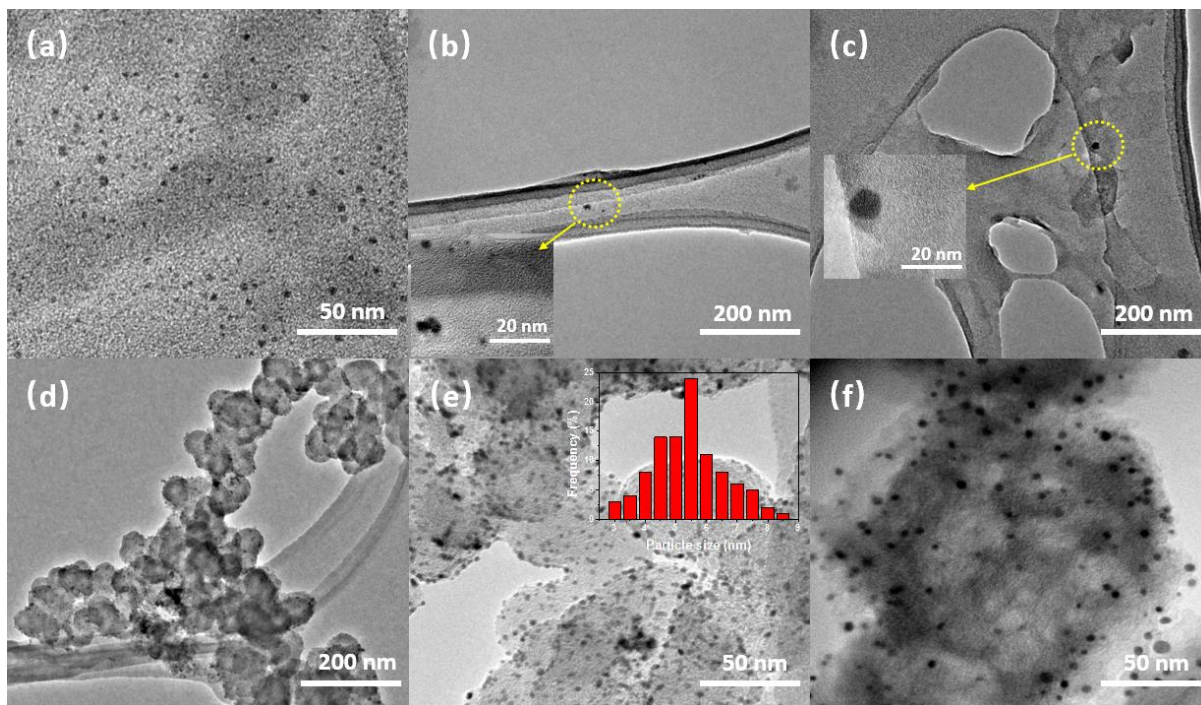


Figure 4. 7 TEM image of (a) metal nanoparticles deposited onto the carbon support for CPt@ZIF-67, (b) CPt@ZIF-67 nanoparticles in homogenous solution before electrochemical test and the inset shows the size of nanoparticles. (c) TEM image of CPt@ZIF-67 after 24h electrochemical stability test and the inset shows the size of nanoparticles remains after stability test. (d) TEM image of commercial 20 wt.% Pt/C. (e) TEM image of commercial 20 wt.% Pt/C and the inset shows the size distribution of nanoparticles for commercial 20 wt.% Pt/C, it was analyzed by randomly selecting 100 nanoparticles to measure their diameters (average diameter = 5.2 nm). (f) TEM image of metal nanoparticles deposited on to the carbon support for CPt@ZIF-8.

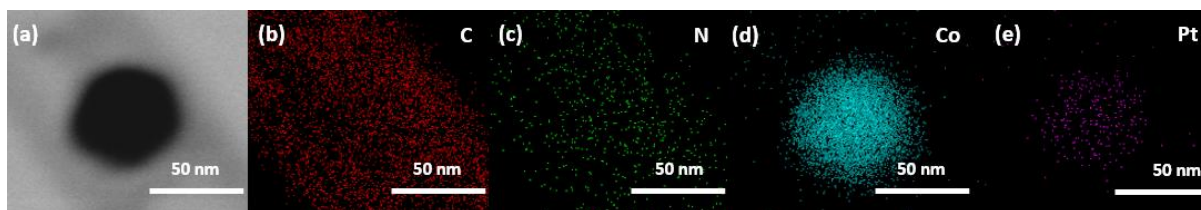


Figure 4. 8 (a) TEM image of Pt@ZIF-67. Element mappings of (b) carbon, (c) nitrogen, (d) cobalt, and (e) platinum.

Further, the structural analysis was carried out on PXRD patterns. Before annealing (Figure 4.9a) the peaks of the samples with and without Pt doping appeared at the same positions with strong contrast with the baseline. It indicates that high crystallinity of the pre-annealed samples and Pt was well distributed without disturbing the ZIF structure.<sup>82,83</sup> After annealing, peaks at  $44.2^\circ$  and  $51.3^\circ$  of CZIF-67 could be assigned to Co (111) and (200) (JCPDS 15-0806) (Figure 4.9c).<sup>84</sup> Blue shifts of those peaks were observed in the CPt@ZIF-67 sample, which is due to the Pt atoms alloyed in the Co cluster structure leads to lattice expansions.<sup>81,85</sup> Meanwhile, the closeness of peaks compared with the CZIF-67 indicates that a limited amount of Pt atoms is alloyed into the Co lattice. The Mo-radiation PXRD of the CPt@ZIF-67 was shown in Figure 4.9e the peaks can be indexed as C (002),<sup>16</sup>  $\text{Co}_3\text{O}_4$  (311),<sup>86</sup> PtCo (111)<sup>87</sup> and PtCo (200),<sup>81</sup> which indicates that the catalyst consists of carbon, cobalt oxide and platinum cobalt alloy respectively.

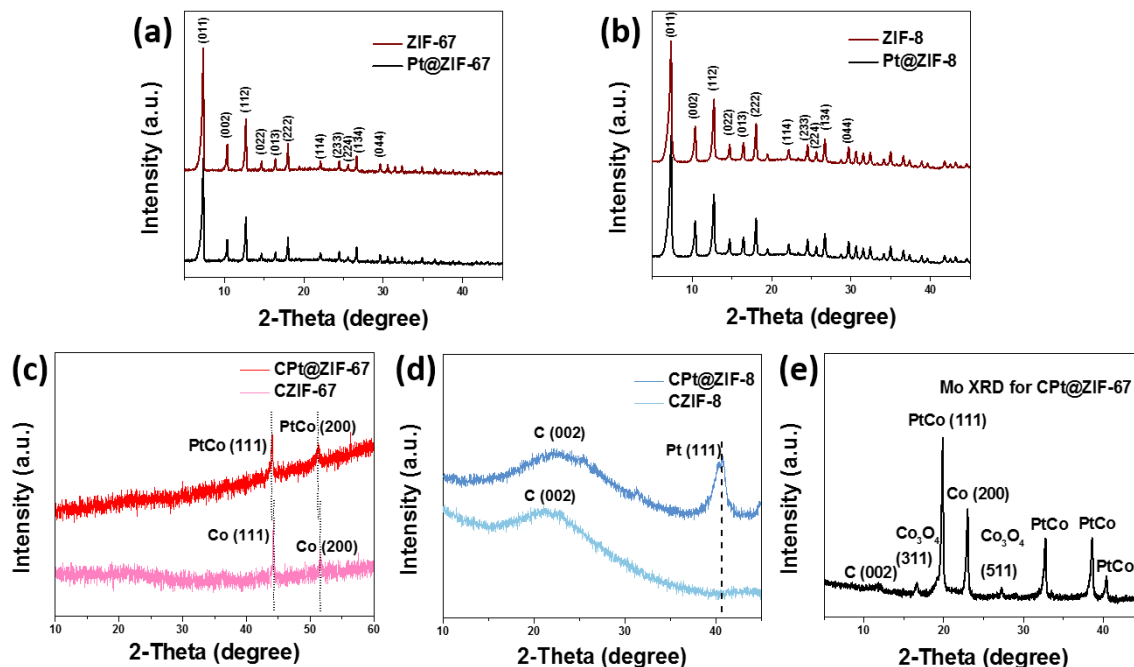


Figure 4. 9 The PXRD diffraction pattern of (a) ZIF-67 and Pt@ZIF-67, (b) PtZIF-8 and Pt@ZIF-8, (c) CPt@ZIF-67 and CZIF-67, (d) CPt@ZIF-8 and CZIF-8, under Cu radiation, and (e) CPt@ZIF-67 under Mo radiation.

Raman spectroscopy measurements were carried out and shown in Figure 4.10. The D band peak (signature disorder-induced  $sp^2$ -hybridized graphitic carbon that is often activated by defects) and the G band peak (the ordered graphitic carbon with stretching vibrations) located at 1340 and 1596  $cm^{-1}$ , respectively. Moreover, the high  $I_D/I_G$  ratio of CPt@ZIF-67 could be concluded that the carbonized ZIFs possessed graphitic characteristics with abundant defect concentration (Figure 4.10a).<sup>88</sup> Another relatively weak 2D broad peak located at 2652  $cm^{-1}$  indicates the metal core contact doping electron to the carbon cages.

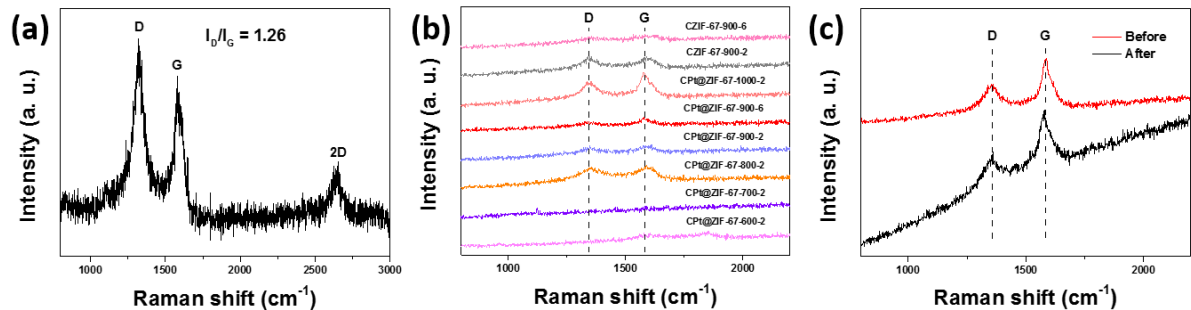


Figure 4. 10 Raman spectra of (a) CPt@ZIF-67, (b) CZIF-67-900-6, CZIF-67-900-2, C10Pt@ZIF-67-1000-2, C10Pt@ZIF-67-900-6, C10Pt@ZIF-67-900-2, C10Pt@ZIF-67-800-2, C10Pt@ZIF-67-700-2 and C10Pt@ZIF-67-600-2. (c) Raman spectra of CPt@ZIF-67 before and after 24h electrochemical stability test. The peak D locates at  $1340\text{ cm}^{-1}$ , the peak G locates at  $1596\text{ cm}^{-1}$  and the 2D peak locates at  $2652\text{ cm}^{-1}$ .

The surface composition, chemical state and electronic state of the CPt@ZIF-67 were characterised by XPS (Figure 4.11). As shown in Figure 4.12a, the comparison of CPt@ZIF-67 and CZIF-67 proved the formation of Pt alloy. In Figure 4.11a, three distinct peaks at 398.4, 400.6 and 402.3 eV, can be assigned to pyridinic N, graphitic N and quaternary N, respectively.<sup>89,90</sup> The formation of the pyridinic N in the annealed sample indicates that the carbonization led to more stable six-membered rings (Table 2.2). The Co and Pt spectra in CPt@ZIF-67 were shown in Figure 4.11b and 4.11c, respectively. The two peaks in each spectrum could be assigned to Co  $2p_{3/2}$  and Co  $2p_{1/2}$ , Pt  $4f_{7/2}$  and Pt  $4f_{5/2}$ , respectively. Compared with the pure Pt metal peaks in 71.4 and 74.5 eV, notable shifts of CPt@ZIF-67 relocated to 71.9 and

75.1 eV.<sup>91</sup> This positive shift was due to the charge transfer from transition metal Co to the noble metal Pt in the alloy, which is also in line with our PXRD analysis.<sup>92</sup>

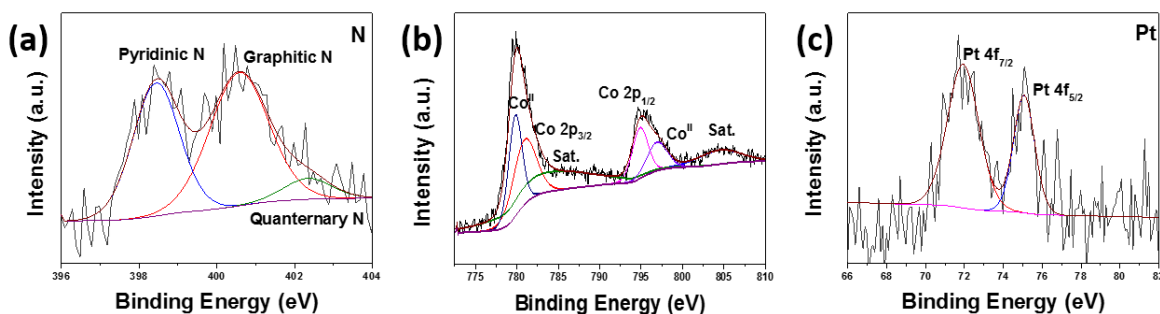


Figure 4. 11 XPS spectra of (a) nitrogen 1s, (b) cobalt 2p, (c) platinum 4f of CPt@ZIF-67.

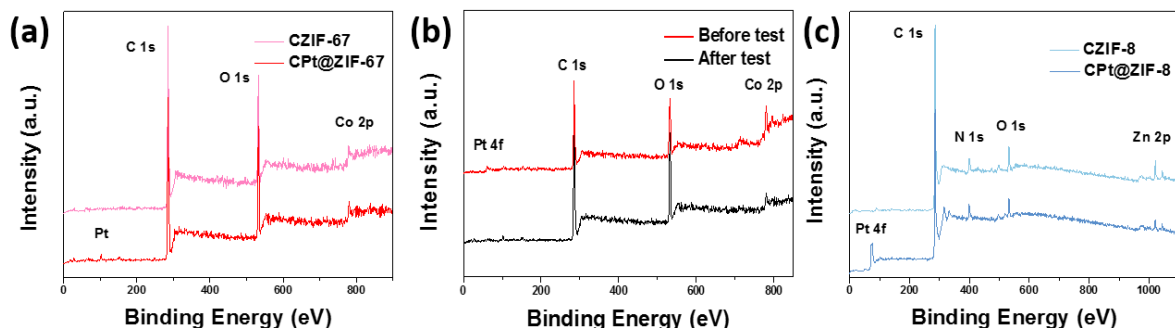


Figure 4. 12 XPS survey spectra of (a) CZIF-67 and CPt@ZIF-67, (b) CZIF-67 and CPt@ZIF-67 before and after 24h electrochemical stability test, (c) CZIF-8 and CPt@ZIF-8.

The Brunauer-Emmett-Teller (BET) surface area and pore size distribution were obtained by N<sub>2</sub> sorption isotherms. The calculated surface areas of CPt@ZIF-67, CZIF-67 and Pt@ZIF-67 were 90.1 m<sup>2</sup>



$\text{g}^{-1}$ ,  $330.2 \text{ m}^2 \text{ g}^{-1}$  and  $1516.2 \text{ m}^2 \text{ g}^{-1}$ , respectively (Figure 4.13a-c). The pore size distributions were also investigated. As shown in Figure 4.13d-f, the CPt@ZIF-67 possessed larger pore size than CZIF-67 and Pt@ZIF-67, mainly concentrated in the range of 4 to 6 nm (Figure 4.13d). In contrast, the pore size ranges of CZIF-67 and Pt@ZIF-67 were focused within 1-4 nm and 1-2 nm, respectively. (Figure 4.13e, f). Hence, the CPt@ZIF-67, with mesoporous characteristics, effectively promotes electrolyte penetration and charge transfer, even while possessing much less surface area.

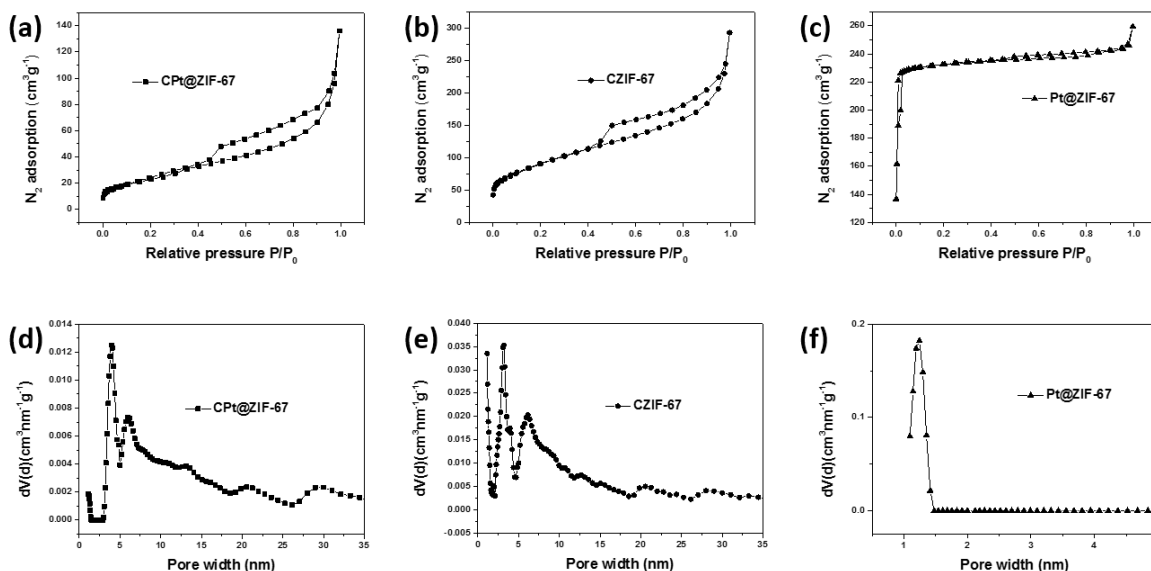


Figure 4. 13  $\text{N}_2$  sorption isotherms of (a) CPt@ZIF-67, (b) CZIF-67 and (c) Pt@ZIF-67. The pore size distribution of (d) CPt@ZIF-67, (e) CZIF-67 and (f) Pt@ZIF-67.

Both MP-AES and XPS were employed to determine the Pt loading and near surface composition of the Pt in the alloy cluster, respectively. The ICP results show that the average Pt loading in the catalysts is ~

5 wt.%, which is comparable with the level of an atomic layer deposition (ALD) synthesis by deposition of single Pt atoms on a nitrogen doped graphene.<sup>56</sup>

XPS depth profiling is also carried out to quantitatively measure the weight percentage of Pt in CPt@ZIF-67. Depth profiling uses an ion beam to etch layers of the surface to reveal subsurface information. In this case, 6 levels (5 gaps of 10 nm) are applied to determine the elemental composition. To eliminate the error, six points were selected from the XPS analysis to give a mean value of only 0.93 wt.% Pt in the near surface region of the catalyst, as detailed in Table 4.1. Collective results show that the CPt@ZIF-67 is of much lower Pt content than the commercial 20 wt.% Pt/C.

Table 4. 1 Pt content in CPt@ZIF-67.

Atomic weight percentage from XPS	Weight percentage of Pt in the catalyst
0.05	0.70
0.06	0.85
0.06	0.90
0.07	0.99
0.07	1.01
0.08	1.15
Average	0.93

### 4.3.2 LSV tests for CPt@ZIF-67/ZIF-8 and different carbonization temperatures and durations

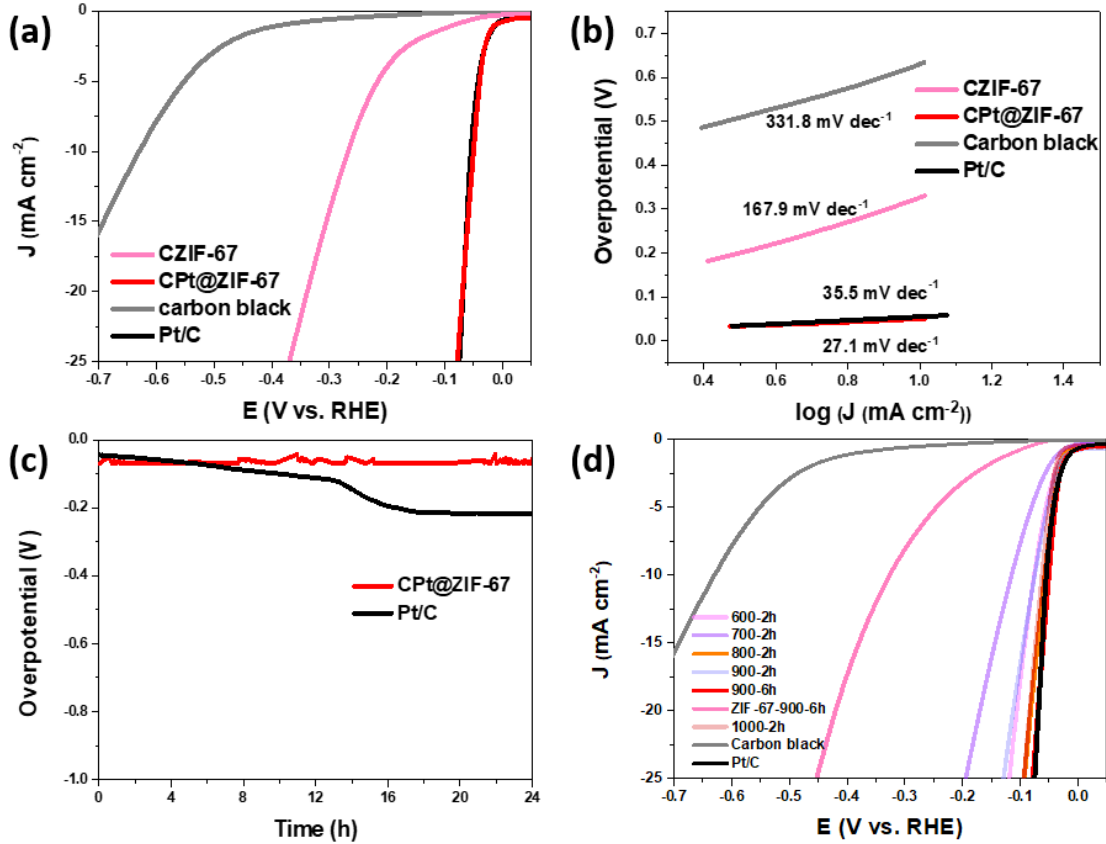


Figure 4. 14 (a) Polarization curves of CZIF-67, CPt@ZIF-67, carbon black and 20 wt.% Pt/C. (b) Tafel plots of CZIF-67, CPt@ZIF-67, carbon black and 20 wt.% Pt/C. (c) I-t curve of CPt@ZIF-67 and 20 wt.% Pt/C up to 24 hours. (d) Polarization curves of carbonized Pt-doped ZIF-67 at 600 °C for 2h, 700 °C for 2h, 800 °C for 2h, 900 °C for 2h, 900 °C for 6h, 1000 °C for 2h, carbon black and 20 wt.% Pt/C.

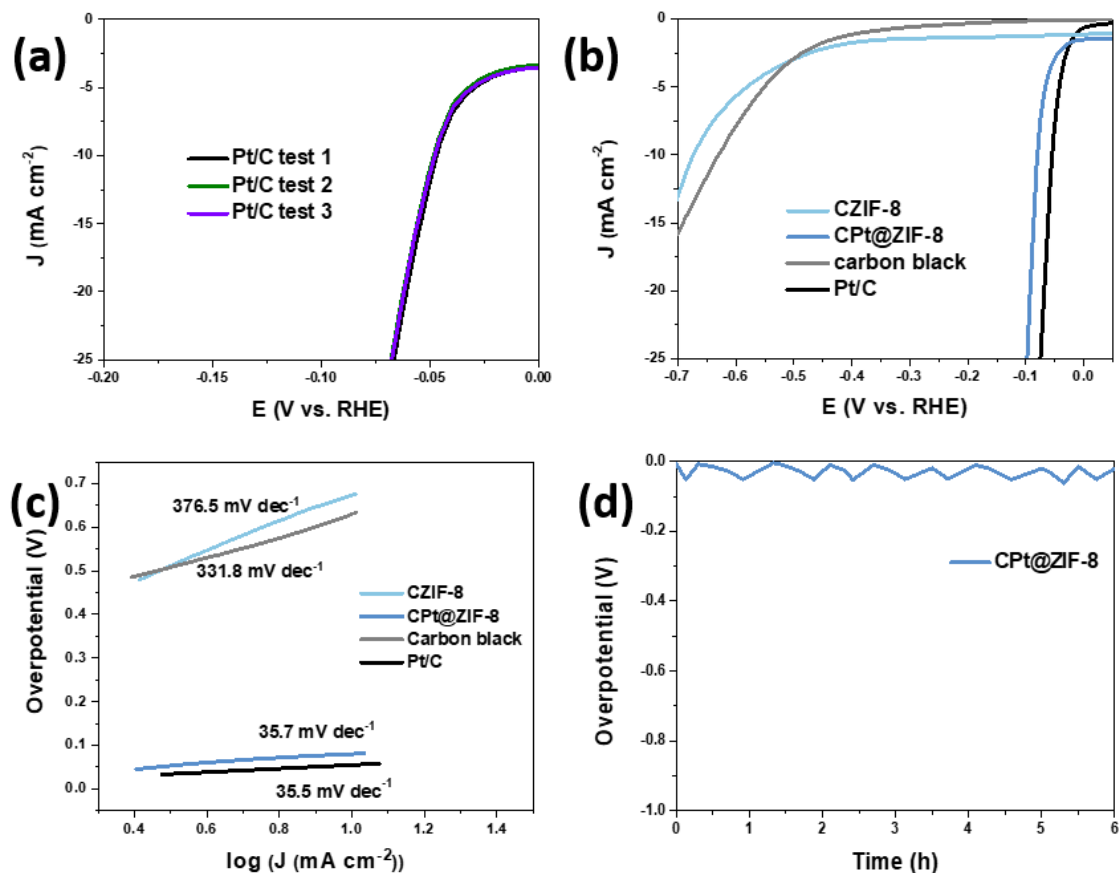


Figure 4. 15 (a) Polarization curves of three tests for 20 wt.% Pt/C. (b) Polarization curves of CZIF-8, CPt@ZIF-8, carbon black and 20 wt.% Pt/C. (c) Tafel plots of CZIF-8, CPt@ZIF-8, carbon black and 20 wt.% Pt/C. (d) Chronopotentiometry of CPt@ZIF-8 under the current density of 10 mA cm<sup>-2</sup> up to 6 hours.

The electrocatalytic HER capability of the catalysts was studied using steady-state linear sweep voltammetry (LSV) on a glassy carbon disk electrode in 0.5 M H<sub>2</sub>SO<sub>4</sub>. The LSV curves of CPt@ZIF-67 were shown in Figure. 4.14a, along with those of CZIF-67, carbon black and 20 wt.% Pt/C for comparison. Overall, the catalysts with Pt loading outperform those without. To achieve a reference current density of 10 mA cm<sup>-2</sup>,

the alloy CPt@ZIF-67 required a 50 mV overpotential, which was 5 mV lower than the 20 wt.% Pt/C (55 mV). Tafel slopes of the four samples were plotted in Figure. 4.14b. The values are 167.9, 27.1, 331.8 and 38.1 mV dec<sup>-1</sup> for CZIF-67, CPt@ZIF-67, carbon black and 20 wt.% Pt/C, respectively (Figure. 4.14b). The results indicate that the HER follows the Volmer-Heyrovsky mechanism.<sup>93,94</sup> It worth to mention that the additional tests were carried out on 20 wt.% Pt/C (Figure. 4.15a), the Tafel slope calculated from these three new tests were all identical, 35.5 mVdec<sup>-1</sup>, which is slightly poorer with the previous literature (31 mVdec<sup>-1</sup>).<sup>95,96</sup> It demonstrates the same trend as in the polarization curves.

The Tafel plot is an electrochemical diagram that shows the relationship between the current generated by an electrochemical cell and the potential of an electrode for a particular metal or a metal-based material. To construct the Tafel plot, the whole process is divided into three steps. At first, select the onset reaction region of the polarization curve (normally 50-100 mV) at the beginning of the reaction. Next, these data points plot the corresponding current density on a logarithmic scale (the X-axis) and the corresponding potential on the Y-axis. Eventually, calculate the slope of the corresponding curve in the linear region. This would be the Tafel slope. CPt@ZIF-67 has approximately 30% lower Tafel slope value in comparison with commercial 20 wt.% Pt/C. The HER on the Pt/C with a Tafel slope of 35.5 mV dec<sup>-1</sup> follows the well-known Tafel mechanism. The CPt@ZIF-67 has a similar Tafel slope (27.1 mV dec<sup>-1</sup>), suggesting that the HER on this catalyst is also dominated by the Tafel mechanism. These

diagrams are usually electrochemical experiments performed under controlled conditions. A 24-hour stability test CPt@ZIF-67 and 20 wt.% Pt/C were carried out, as shown in Figure. 4.14c, where the activity decays are virtually negligible for CPt@ZIF-67 in comparison with 20 wt.% Pt/C. This could be attributed to the catalyst being protected by the carbon shell from erosion by the acidic electrolyte. The morphology and structure of the catalyst are well-stored since Figure 4.7b, 4.7c, 4.10c and 4.12b proves that there is imperceptible change for CPt@ZIF-67 before and after stability tests. Assuming all the Pt atoms are the active sites to the acidic electrolyte. Approximately  $4.01 \times 10^{16}$  sites  $\text{cm}^{-2}$  are accessible to the electrolyte, which are more than that of Pt(111) ( $1.5 \times 10^{15}$  sites  $\text{cm}^{-2}$ ).<sup>97</sup> Then the turnover frequency (TOF) of the HER is calculated.

To calculate the turnover frequency (TOF) per platinum site on the CPt@ZIF-67 catalyst, we used the following formula:

$$\text{TOF} = \frac{\# \text{ total hydrogen turnover} / \text{cm}^2 \text{ geometric area}}{\# \text{ active sites} / \text{cm}^2 \text{ geometric area}}$$

The maximum number of the active sites was calculated based on the assumption that all Pt atoms in the CPt@ZIF-67 form the active sites and are accessible to the electrolyte. The Pt content of the CPt@ZIF-67 was calculated from the ICP data:

$$\begin{aligned} & \frac{5 \text{ mg}}{100 \text{ mg}} \times 0.26 \frac{\text{mg}}{\text{cm}^2} \times \frac{1}{195.08} \frac{\text{mmol}}{\text{mg}} \times 6.022 \times 10^{20} \frac{\text{sites}}{\text{mmol}} \\ & = 4.01 \times 10^{16} \frac{\text{sites}}{\text{cm}^2} \end{aligned}$$

The total of hydrogen turnover was calculated from the current density:

$$\#_{\text{H}_2} = \frac{j \times N_A}{n \times F}$$

$j$  = the current density ( $\text{A cm}^2$ )

$N_A$  = the Avogadro number

$n$  = the number of electrons transferred to evolve  $\text{H}_2$

$F$  = the Faraday constant

$\#_{\text{H}_2}$

$$\begin{aligned} &= \left(j \frac{\text{mA}}{\text{cm}^2}\right) \left(\frac{1 \text{ mol e}^{-1}}{96485.3 \text{ C}}\right) \left(\frac{1 \text{ C}}{1000 \text{ mA}}\right) \left(\frac{1 \text{ mol H}_2}{2 \text{ mol e}^{-1}}\right) \left(\frac{6.022 \times 10^{23} \text{ molecules H}_2}{1 \text{ mol H}_2}\right) \\ &= 3.12 \times 10^{23} \frac{\text{H}_2/\text{s}}{\text{cm}^2} \text{ per } \frac{\text{mA}}{\text{cm}^2} \end{aligned}$$

Hence, at an overpotential of 100 mV, the HER current density is 37.8  $\text{mA cm}^{-2}$ , and the TOF of the CPt@ZIF-67 was

$$\text{TOF} = \frac{\frac{3.12 \times 10^{15} \text{ H}_2/\text{s}}{\text{cm}^2} \text{ per } \times 37.8 \frac{\text{mA}}{\text{cm}^2}}{4.01 \times 10^{16} \text{ sites per cm}^2} = 2.94 \text{ s}^{-1}$$

Similarly, the TOF of the CPt@ZIF-67 at the overpotential of 50 mV was

$$\text{TOF} = \frac{\frac{3.12 \times 10^{15} \text{ H}_2/\text{s}}{\text{cm}^2} \text{ per } \times 10.3 \frac{\text{mA}}{\text{cm}^2}}{4.01 \times 10^{16} \text{ sites per cm}^2} = 0.80 \text{ s}^{-1}$$

The TOF the CPt@ZIF-67 is 2.94 and 0.80  $\text{s}^{-1}$  at  $\eta = 100$  and 50 mV, respectively, much better than the other published noble-metal or non-noble metal-based catalysts (Table 4.2). Likewise, Table 4.3 gives a

clear comparison of the Tafel slopes of CPt@ZIF-67 and other reported HER catalysts, included Pt alloy.



Table 4. 2 TOF of the CPt@ZIF-67 and other catalysts.

Catalysts	Electrolyte	Overpotential (mV)	TOF (s <sup>-1</sup> )	Reference
CPt@ZIF-67	0.5 M H <sub>2</sub> SO <sub>4</sub>	100	2.94	This work
Li-PPS ND	0.5 M H <sub>2</sub> SO <sub>4</sub>	140	1.60	98
MoS <sub>2</sub>  Au111]	0.5 M H <sub>2</sub> SO <sub>4</sub>	100	~0.10	99
FeP/Ti	0.5 M H <sub>2</sub> SO <sub>4</sub>	100	0.28	100
Ni-C-N NSs	0.5 M H <sub>2</sub> SO <sub>4</sub>	100	0.44	101
CoP	0.5 M H <sub>2</sub> SO <sub>4</sub>	100	0.046	102
CoNx/C	0.5 M H <sub>2</sub> SO <sub>4</sub>	100	0.39	103
Ni <sub>2</sub> P nanoparticles	0.5 M H <sub>2</sub> SO <sub>4</sub>	100	0.015	104
Electrodeposited H <sub>2</sub> -CoCat	aqueous phosphate buffer	380	0.020	105
Defect-rich MoS <sub>2</sub> nanosheet	0.5 M H <sub>2</sub> SO <sub>4</sub>	300	0.73	106

Table 4. 3 Summary of representative HER catalysts in acidic electrolyte.

Catalyst	Electrolyte	Overpotential at 10 mA cm <sup>-2</sup> (mV)	Tafel slope (mV dec <sup>-1</sup> )	Reference
CPt@ZIF-67	0.5 M H <sub>2</sub> SO <sub>4</sub>	50	27	This work
ALD50Pt/NGNs	0.5 M H <sub>2</sub> SO <sub>4</sub>	45	29	56
Co@BCN	0.5 M H <sub>2</sub> SO <sub>4</sub>	96	64	107
NiMo-NGTs	0.5 M H <sub>2</sub> SO <sub>4</sub>	65	67	108
Co <sub>2</sub> P@NPG	0.5 M H <sub>2</sub> SO <sub>4</sub>	130	58	109
WS <sub>2</sub> nanosheets	0.5 M H <sub>2</sub> SO <sub>4</sub>	230	60	110
N, P-graphene	0.5 M H <sub>2</sub> SO <sub>4</sub>	420	91	51
Cu <sub>3</sub> P@NPPC-650	0.5 M H <sub>2</sub> SO <sub>4</sub>	292	76	111
MoS <sub>2</sub> /RGO	0.5 M H <sub>2</sub> SO <sub>4</sub>	140	41	112
Pt-SnS <sub>2</sub>	0.5 M H <sub>2</sub> SO <sub>4</sub>	117	69	113
MoS <sub>2</sub> /graphene	0.5 M	121	46	114

	H <sub>2</sub> SO <sub>4</sub>			
Pt-MoS <sub>2</sub>	0.5 M H <sub>2</sub> SO <sub>4</sub>	-	52	115
Pd ND/DR- MoS <sub>2</sub>	0.5 M H <sub>2</sub> SO <sub>4</sub>	208	66	116
Au-MoS <sub>2</sub>	0.5 M H <sub>2</sub> SO <sub>4</sub>	-	69	117
Ru-C <sub>3</sub> N <sub>4</sub>	0.5 M H <sub>2</sub> SO <sub>4</sub>	140	57	118

The electrochemically active surface area (ECSA) was calculated by measuring the total charge of the H<sub>upd</sub> adsorption/desorption region.<sup>119</sup> The specific ECSA (the ECSA per unit weight of metal) of the CPt@ZIF-67 is 64.3 m<sup>2</sup> g<sub>pt</sub><sup>-1</sup> that is slightly higher than the commercial 20 wt.% Pt/C (63 m<sup>2</sup> g<sub>pt</sub><sup>-1</sup>).<sup>120</sup>

Cyclic voltammetry (CV) measurements were carried out in 0.5 M H<sub>2</sub>SO<sub>4</sub> electrolyte at a scan rate of 10 mVs<sup>-1</sup>. The ECSA was determined by the following formula:

$$\text{specific ECSA} = Q_H / (m \times q_H)$$

where Q<sub>H</sub> is the total charge for H<sub>upd</sub> adsorption, m is the active mass of Pt metal, and q<sub>H</sub> is the charge required to oxidize a monolayer of hydrogen on a Pt surface.

The ECSA was estimated by measuring the coulombic charge for hydrogen adsorption (Q<sub>H</sub>) in the range of -0.2 to -0.4 V (vs. RHE) and q<sub>H</sub> is a constant which equals to 210 μC cm<sup>-2</sup>. The H<sub>upd</sub> adsorption

charge ( $Q_H$ ) can be calculated by  $Q_H = Q/2$ , where  $Q$  is the total charge under the  $H_{\text{upd}}$  adsorption/desorption area obtained after double-layer correction. The loading mass of Pt was investigated by the microwave plasma atomic emission spectroscopy (MP-AES) result. Hence, the ECSA of CPt@ZIF-67 is  $64.3 \text{ m}^2 \text{ g}_{\text{pt}}^{-1}$ .

To further understand the electrocatalytic activity of CPt@ZIF-67 for HER, we performed electrochemical impedance spectroscopy (EIS). The Nyquist plots of the EIS results are demonstrated in Figure 4.16. The Nyquist plot of CPt@ZIF-67 gave a similar semicircle in comparison with commercial 20 wt.% Pt/C. This result gives another proof that the CPt@ZIF-67 affords the close kinetics with the commercial catalyst (although only a quarter of Pt applied).

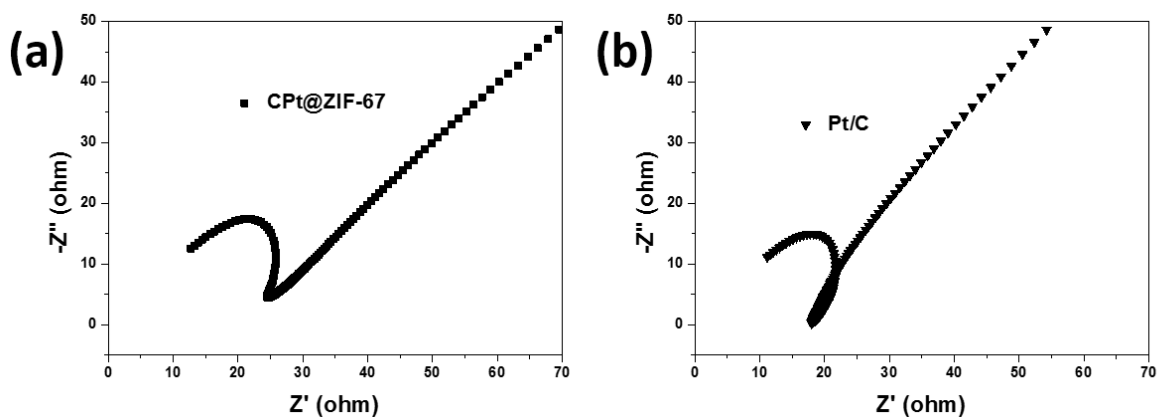


Figure 4. 16 Electrochemical impedance spectra (EIS) of (a) CPt@ZIF-67 and (b) commercial 20 wt.% Pt/C over the frequency ranging from 100 kHz to 00.1 Hz at the open-circuit voltage.

The mass density comparison is shown in Figure 4.17. At an

overpotential of 10 mV, CPt@ZIF-67 exhibited a mass density of 0.87 A mg<sup>-1</sup> Pt, which is about 4 times higher than those obtained by commercial 20 wt.% Pt/C (0.22 A mg<sup>-1</sup> Pt). This outstanding electrocatalytic activity of CPt@ZIF-67 may be ascribed to the uniformly dispersed PtCo clusters spreading over relatively large surface area for electrochemical reactions, even at a relatively low overall loading (5 wt.%). More importantly, a downshift of the Pt d-band may exist for the Pt electronic structure when PtCo alloy is formed, due to the charge localization between Co and Pt.<sup>121</sup> This should reduce the desorption energy of proton around the Pt site, so as to facilitate formation of H<sub>2</sub> gas molecules.

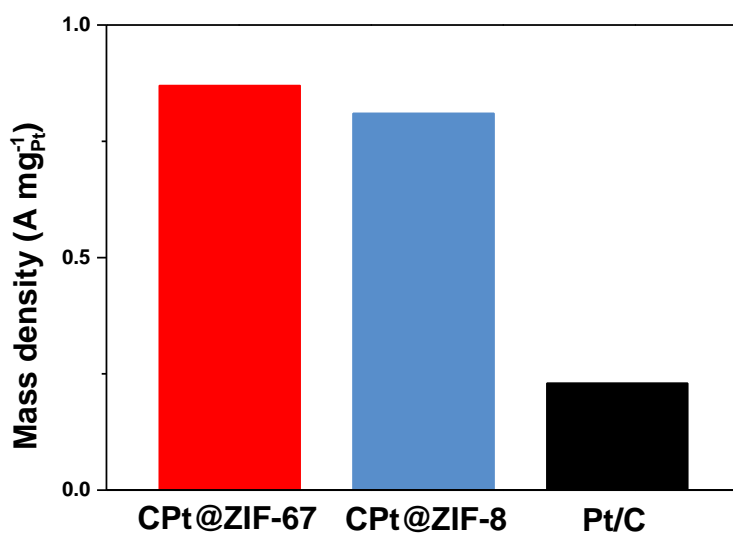


Figure 4. 17 Mass activity at 0.01 V (versus RHE) of the CPt@ZIF-67, CPt@ZIF-8 and Pt/C catalysts for the HER.

### 4.3.3 Optimization of CPt@ZIF-67/ZIF-8 for hydrogen evolution reaction

Moreover, the effect of annealing temperature and time on CPt@ZIF-67 for the HER performance were also investigated, as shown in Figure 4.14d. As expected, the activities are in the following order: CPt@ZIF-67-900-6 > CPt@ZIF-67-800-2 > CPt@ZIF-67-1000-2 > CPt@ZIF-67-900-2 > CPt@ZIF-67-600-2 > CPt@ZIF-67-700-2. The results suggest that the porosity and metal clustering of the catalysts play an important role. Meanwhile, the long annealing time seems to outperform the short ones, possibly by yielding higher crystallinity of carbon, to enhance conductivity of the catalysts.

ZIF-8 was synthesized using a similar synthetic route with ZIF-67, Pt@ZIF-8 and CPt@ZIF-8 only using the zinc nitrate hexahydrate, instead of the cobalt nitrate hexahydrate.

Before annealing, the AFM imaging and height profile measurements indicate the cubic structure of Pt@ZIF-8 and the particle sizes of Pt@ZIF-8 can vary from 200 to 400 nm (Figure 4.2d-f). The SEM images (Figure 4.3a) confirms the same morphology.

After annealing, CZIF-8 showed no evident peak, implying an amorphous structure. It also confirmed that there is virtually no crystalline Zn residue for ZIF-8 related compounds after annealing at 900 °C or above. For the CPt@ZIF-8, the peak at 40.7° can be assigned to Pt (111) (JCPDS 65-2868), which also possesses the

active sites and lowers the overpotential for HER (Figure 4.9d).

The LSV curve of CPt@ZIF-8 was shown in Figure 15, along with those of CZIF-8, carbon black and 20 wt.% Pt/C for comparison. Overall, the catalysts with Pt loading outperform those without. The similar performance levels of the CZIF-8 and carbon black also indicate no metal residue as catalysts centers in the CZIF-8. Tafel slope of the four samples were plotted in Figure 15b. The values are 376.5, 35.7, 331.8 and 38.1 mV dec<sup>-1</sup> for CZIF-8, CPt@ZIF-8, carbon black and 20 wt.% Pt/C, respectively. The results indicate that the HER follows the Volmer-Heyrovsky mechanism.<sup>122,123</sup> It demonstrates the same trend as in the polarization curves. Both CPt@ZIF-8 has a comparable HER activity with the commercial 20 wt.% Pt/C. In addition, a 6-hour stability test of CPt@ZIF-8 was carried out, as shown in Figure 4.15c, where the activity decays are virtually negligible. This could be attributed to the catalyst being protected by the carbon shell from erosion by the acidic electrolyte.

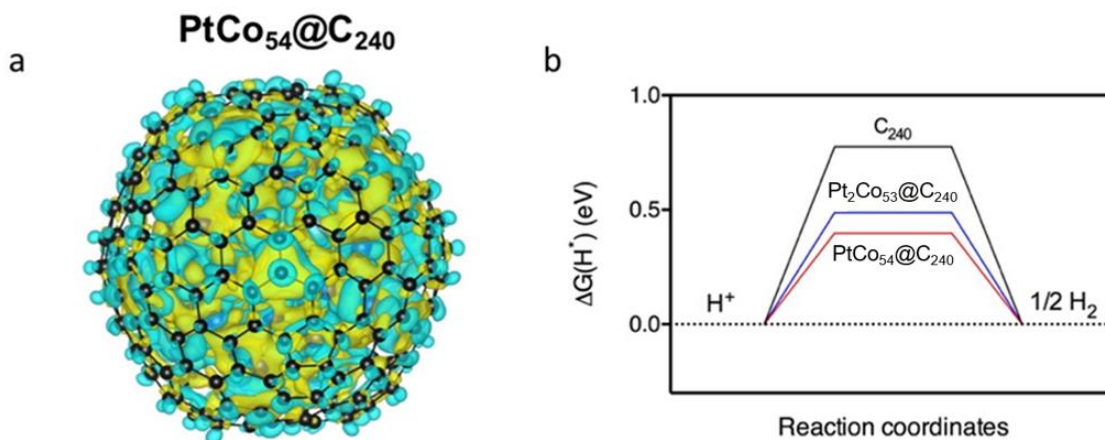


Figure 4. 18 (a) The electron density difference of PtCo<sub>54</sub>@C<sub>240</sub>, where the blue and yellow represents electron accumulated and diminished area, respectively. (b) The free energy diagram of HER on C<sub>240</sub>, PtCo<sub>54</sub>@C<sub>240</sub> and Pt<sub>2</sub>Co<sub>53</sub>@C<sub>240</sub>.

Density Functional Theory (DFT) calculations were carried out in order to clarify further the effects of alloying and the metal cluster embedded nitrogen-doped carbon catalysts. Predominately,  $|\Delta G(H^*)|$  is a good descriptor for the HER activity and should be close to zero to balance H<sup>\*</sup> adsorption and desorption within the reaction steps.<sup>124</sup> The chosen models included the metal clusters, *i.e.* Co<sub>55</sub> cluster, and Pt doped Co clusters of different Pt/Co ratios, as shown in Figure 4.19. The C<sub>240</sub> fullerene ball was adopted to mimic the outer carbon coating for the metal clusters, as adopted in previous studies.<sup>125,126</sup> Furthermore, to avoid the DFT description failure on the open shell d-electrons of the transition metal, DFT+U, originally proposed by Anisimov *et al.*<sup>127</sup> was adopted to treat appropriately the strongly correlated electron intra-atomic Coulomb (U) and exchange (J) interactions within a HF-like theory, while the rest of the system with pure DFT.



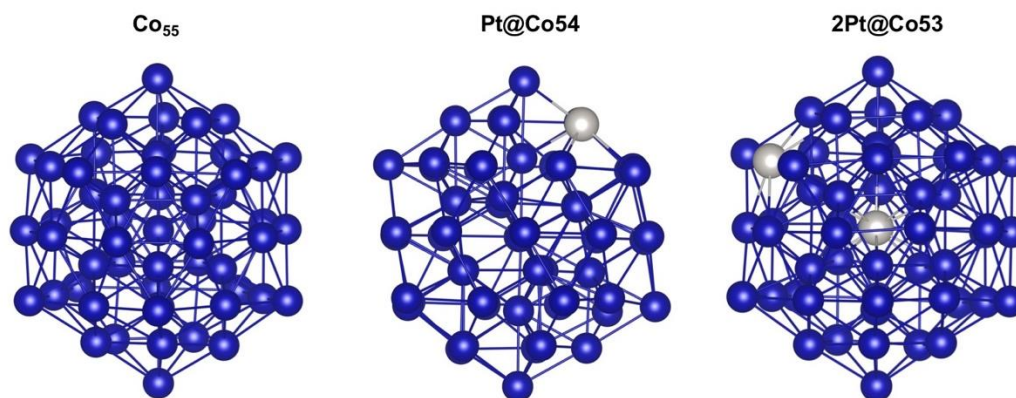


Figure 4. 19 The  $\text{Co}_{55}$  (a),  $\text{PtCo}_{54}$  (b) and  $\text{Pt}_2\text{Co}_{53}$  (c) metal clusters. Each cluster optimised to energy minimum.

Unlike the metal clusters used in previous studies, which are simple cubic  $\text{Co}_{55}$  clusters, the model here was adopted from the global minima with the Gupta potential, as shown in Figure 4.19a. The energy difference of those two clusters was 1.05 eV/atom, which is too great to be ignored. Furthermore, Pt doping positions were also considered, including corner, edge and body positions, respectively. As shown in Table 4.4, for  $\text{PtCo}_{54}$ , a single Pt atom tended to occupy the edge positions (Figure 4.19b). This conclusion is consistent with a recent publication, where Pt atoms enrich the edge positions of the dodecahedral Pt/Ni clusters.<sup>128</sup> It should be also noted that both doping at the corner and the edge positions were exothermic, while the replacement at the body position was endothermic. For  $\text{Pt}_2\text{Co}_{53}$  (Figure 4.19c), the formation energy was listed in Table 4.5. Dual Pt atoms preferred to dope the edge and the body positions (Figure 4.19c). Clearly, only the surface doped Pt could act as an effective active site for HER. The Bader analysis was also carried out to study the electron

transfer within the metal alloy cluster.<sup>129</sup> The results show that the average valence electrons on Pt increased by 0.77e and 0.87e for PtC<sub>54</sub> and Pt<sub>2</sub>Co<sub>53</sub>, respectively. This is also in line with the observation in our XPS and PXRD analyses. According to the d-band theory, these charge transfer to the active sites can further reduce the overpotential.

Table 4. 4 The calculated formation energy of single Pt atom doping in Co<sub>55</sub> cluster.

Pt doping position	E formation (eV)
corner	-1.13
edge	-1.28
body	2.96

Table 4. 5 The calculated formation energy of dual Pt atoms doping in C<sub>55</sub> cluster.

Pt doping position	E formation (eV)
corner- corner nearby	-5.49
corner- corner faraway	-5.59
corner- edge nearby	-4.57
corner- edge faraway	-5.69
corner- body	-5.47
edge- edge nearby	-5.63
edge-edge faraway	-5.47
edge- body	-5.78
body-body nearby	-5.17
body-body faraway	-4.95

The details of calculation of the HER free energy were provided in the Methods Section, and different adsorption/desorption sites of  $H^*$  were also considered, as shown in Figure 4.20. The calculated free energy diagram of a single-layer carbon shell, carbon shell within different PtCo alloy clusters was shown in Figure 18b. Compared with bare  $C_{240}$ , the free energy has been dramatically tuned down, by 48.6%, if the metal cluster is inside the carbon shell. For different levels of Pt doping, the energy barrier of the structure with 2 Pt atoms was 90.1 meV higher than that of the single Pt doped. Hence, the “extra” Pt atom in  $Pt_2Co_{53}@C_{240}$  does not provide an additional active site, nor lowers the energy barrier for activation. Hence, the catalyst performance didn't linearly increase with the Pt doping level. The free energy of the metal-only clusters was also calculated for comparison, Figure 4.21. Though those possess a lower free energy (0.12 eV), the metal-only clusters were difficult to stabilize in the practical environment, due to the lack of a ligand stabilizer. The electron density difference with/without the C-shell,  $PtCo_{54}@C_{240}$ , was also calculated, shown in Figure 18a. The electron density seems to be accumulated at the outside of the carbon cage, which is also in line with the Raman shift in our experiment section. The charge redistribution could largely facilitate the attraction / sorption of the  $H^+$  for the HER reaction.

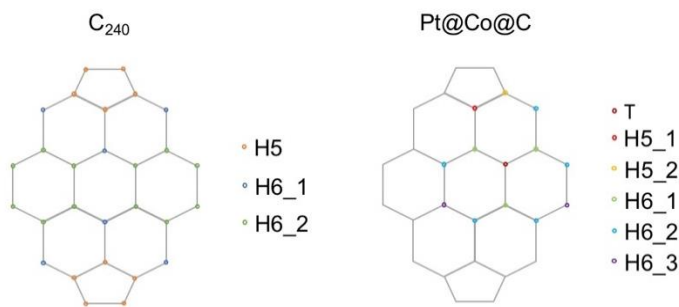


Figure 4. 20 The possible reactive sites of  $C_{240}$  and  $C_{240}$  with Pt/Co alloy cluster inside.

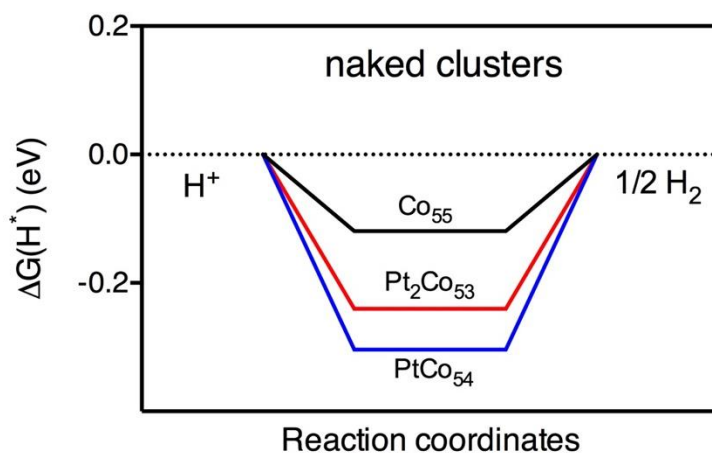


Figure 4. 21 The free energy diagram of naked Co and Pt/Co alloy clusters.

#### 4.4 Conclusions

PtCo cluster-embedded porous carbon catalysts have been effectively synthesized via Pt-doped ZIF-67 formation and then tailored carbonization, leading to nitrogen doped and finely dispersed PtCo clusters firmly anchored over the derived porous carbon. The resulting

catalyst (CPt@ZIF-67 or CPtCo@C) exhibits extraordinary performance for HER in 0.5 M H<sub>2</sub>SO<sub>4</sub>, achieving a Tafel slope of 27.1 mV dec<sup>-1</sup> with an overpotential of only 50 mV at the reference current density of 10 mA cm<sup>-2</sup>, which is four times of the mass-specific energy density of the commercial counterpart (20 wt.% Pt/C), even at a much lower Pt loading of 5 wt.%.

The improvement is partly attributed to the readiness of charge transfer from the metal cluster to lower the d-band centre, the high electron conductivity of the well-integrated carbon substrate, and the richness of the N-functional groups, along with the dispersion of the fine clusters and large surface area. Meanwhile, the catalysts also possessed excellent stability, up to 24 hours with negligible loss of activity in an acidic electrolyte. DFT calculations further revealed that the Pt doping in the Co cluster does not always favour the surface sites, to impart direct benefit to HER. Hence, additional Pt doping does not proportionally enhance the HER activity. The carbon cage outside the metal clusters is more electronegative, which also enhances H<sup>+</sup> sorption for HER. Overall, the approach harnessed several beneficial effects to generate a very effective HER catalyst as a low cost and highly stable alternative to the commercial 20 wt.% Pt/C for hydrogen production. It also provides a design strategy for low Pt loading over surfaces to impart effectiveness at low material's cost. The catalyst can also be a strong candidate for the overall water splitting process in the future.

Note: Most of the work in Chapter 4 was published in the paper “Y. Qin, X. Han, S. Gadipelli, J. Guo, S. Wu, L. Kang, J. Callison and Z. Guo, *J. Mater. Chem. A*, 2019, 7, 6543–6551.”

## Chapter 5. Carbonized Ni/Co/Fe@ ZIF-67 or ZIF-8 as High Performance Electrocatalysts for Hydrogen Evolution Reaction

### 5.1 Introduction

The process of electrochemical hydrogen production via water splitting is of great importance for solving the energy crisis and associated environmental problems (particularly for global warming). Noble metal Pt-based material has been recognized as the optimal catalyst for the hydrogen evolution reaction. However, because of the degree of scarcity and the high costs associated with the procurement of noble metals, the large-scale utilization of the Pt base material catalyst is severely limited. Therefore, a highly active and stable non-noble metal electrocatalyst should be developed. This should incorporate a number of constituents. These include carbides,<sup>130, 131</sup> oxides,<sup>132, 133</sup> nitrides,<sup>134, 135</sup> sulfides,<sup>136, 137</sup> phosphides.<sup>138, 139</sup> This is the key to reducing the cost whilst improving the efficiency of water decomposition.

To maximize the HER electrocatalytic efficiency and stability of transition-metal-based catalysts, the structure of the catalysts should be optimized in order to expose more catalytic active sites to improve the catalytic efficiency of HER.<sup>140</sup> Liang reported that the HER performance can be improved via heteroatom doping with porous carbon.<sup>141</sup> Zeolitic imidazolate frameworks (ZIFs), such as ZIF-67 and

ZIF-8, is a new class of porous material, which has huge BET surface area (beneficial to charge and mass transfer in electrocatalysis), high thermal and chemical stability, abundant carbon and nitrogen atoms, as well as high metal ion content that it is expected to be a good candidate as the template to synthesize porous nanostructured materials for HER.<sup>142,143</sup> However, until the present, the designing of a new hybrid nanostructure between transition-metal-based materials and heteroatom carbon material as an effective HER catalyst continues to represent a challenging task.

In order to address the considerations previously discussed, a nanostructured catalyst was synthesized. This consisted of nickel nanoparticles anchored on a nitrogen doped ZIF-8 via direct carbonization strategy, named CNi@ZIF-8 (carbonized Ni doped on ZIF-8 with carbonization temperature of 900 °C for 6 hours). All of the samples mentioned below take the carbonization temperature and duration of 900 °C for 6 hours, unless otherwise specified. The electrochemical measurements indicated that it worked particularly well as an efficient and stable hydrogen evolution reaction catalyst. CNi@ZIF-8 achieved a Tafel slope of 40.4 mV dec<sup>-1</sup> with an overpotential of 141 mV at current density of 10 mA cm<sup>-2</sup>. The optimized catalyst also gave long-term durability in 0.5 M H<sub>2</sub>SO<sub>4</sub> up to 24h.



## 5.2 Methodology

### 5.2.1 Synthesis methods

#### Synthesis of ZIF-8

First, zinc nitrate hexahydrate (12.33 g) was dissolved in 500 mL methanol. Then, 2-methylimidazole (13.59 g) was dissolved in another 500 mL methanol. The latter solution was slowly added to the former in a 1 L wide mouth jar while stirring at room temperature. Stirring proceeded for 2 h, after which the solution was left to settle for 24 h. The clear top solution was drained, and the white precipitate was collected by centrifugation with further methanol washing. The sample was dried in an oven at 80 C for 24 h.

#### Synthesis of Ni@ZIF-8 and CNi@ZIF-8

1 g of nickel (II) nitrate hexahydrate ( $\text{Ni}(\text{NO}_3)_2 \cdot 6\text{H}_2\text{O}$ ) was dissolved in 10 mL methanol. As-synthesized ZIF-8 crystal powder (100 mg) and 100  $\mu\text{L}$  of nickel (II) nitrate hexahydrate solution were added into methanol (20 mL). Sonication and stirring were carried out for 1 h to achieve a homogenous inky solution. Ni-doped ZIF-8 (Ni@ZIF-8) was obtained by grinding the green solid into fine powder after evaporating the methanol in the oven at 80 °C for 24 hours. Then, the product was carbonized at 900 °C (heating rate of 5 °C  $\text{min}^{-1}$ ) in an alumina boat (1 x 1.5 x 5 cm) in a horizontal tube furnace to form carbonized ZIF-8 with Ni doping, termed CNi@ZIF-8. The powders were annealed at 900 °C

for 6 hours under nitrogen and cooled to room temperature. After carbonization, black solids were collected and ground into fine powder. Carbonized cobalt doped ZIF-8 (CCo@ZIF-8) and carbonized iron doped ZIF-8 (CFe@ZIF-8) were also prepared by the similar pathways, only changed nickel (II) nitrate hexahydrate into cobalt (II) nitrate hexahydrate and iron(III) nitrate nonahydrate, respectively.

### **5.2.2 Physical characterization**

Powder X-ray diffraction (PXRD, Stoe Stadi-P, Cu-K-alpha and MoK-alpha) was carried out by encapsulation of samples in a 0.5 mm diameter borosilicate glass capillary under ambient conditions. X-ray photoemission spectroscopy (XPS, Al-K-alpha, Thermo Scientific) and scanning electron microscopy (SEM, Jeol) were carried out on carbon tape. Transmission electron microscopy (TEM, Jeol) measurements were completed on a carbon-coated copper TEM grid support.

### **5.2.3 Electrochemical test**

All tests were carried out using an Autolab (Metrohm PGSTAT302N) electrochemical station, using a three-electrode method with a glassy carbon rotating disk as the working electrode and carbon rod and Ag/AgCl/saturated KCl as counter and reference electrode, respectively, in an acidic electrolyte (0.5 M H<sub>2</sub>SO<sub>4</sub>) at room temperature. All measurements were carried out with a fixed catalyst deposition of  $\sim 0.26 \text{ mg cm}^{-2}$  on a 3 mm diameter (area of  $0.0707 \text{ cm}^2$

2) glassy carbon disk electrode. The catalyst was prepared as follows: 2 mg of sample was dispersed in a 540 mL solution consisting 500 mL of 4:1 v/v water/ethanol and 40 mL of Nafion (5% solution) under sonication. The sonication was carried out up to an hour to get uniform dispersion of catalyst ink, of which 5 mL was micropipetted and dropped on a glassy carbon disk electrode followed by drying at 60 C in the oven. All electrochemical test results are reported with respect to the reference Ag/AgCl. The linear sweep voltammetry (LSV) curves were recorded with voltage sweeping at  $10 \text{ mV s}^{-1}$  in the potential range of +0.0 V to -0.7 V with disk rotating speed of 1600 rpm in 0.5 M  $\text{H}_2\text{SO}_4$ . The data were collected after stable CVs were obtained. The measured potentials against Ag/AgCl were converted to RHE using the following relation: in 0.5M  $\text{H}_2\text{SO}_4$ ,  $E_{(\text{RHE})} = E_{\text{Ag/AgCl}} + 0.059 \text{ pH} + E^{\circ}_{\text{Ag/AgCl}}$ , where  $E^{\circ}_{\text{Ag/AgCl}} = 0.1976 \text{ V}$  at 25 °C and  $E_{\text{Ag/AgCl}}$  is the working potential. The overpotential  $E = E_{(\text{RHE})}$ .

## 5.3 Results and Discussion

### 5.3.1 Morphology and composition

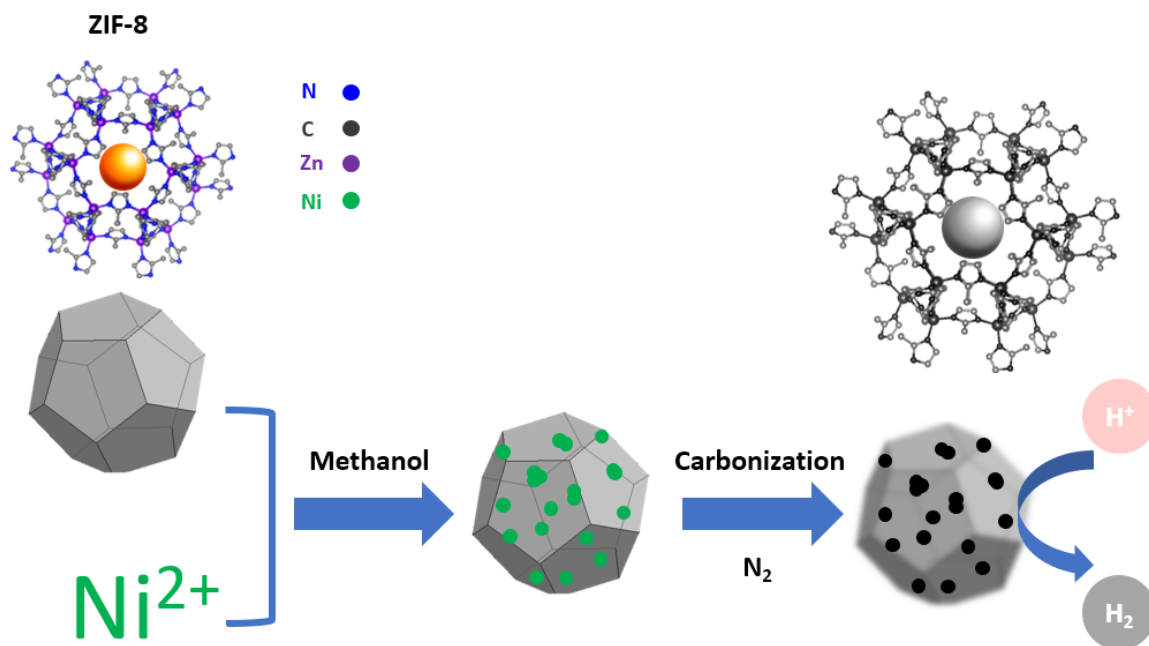


Figure 5. 1 Illustration of the synthesis procedures of carbonized Ni-doped nanoparticles (CNi@ZIF-8).

CNi@ZIF-8 was synthesized by mixing ZIF precursors and the nickel salt in methanol by stirring and refluxing. Following this, the solvent was evaporated and the as-prepared material was annealed in an inert N<sub>2</sub> atmosphere at 900 °C for 6h. For comparison, the carbonized ZIF without the Ni salt was also prepared, denoted as CZIF-8. The procedures are illustrated in Figure 5.1 and detailed in the Experimental section.

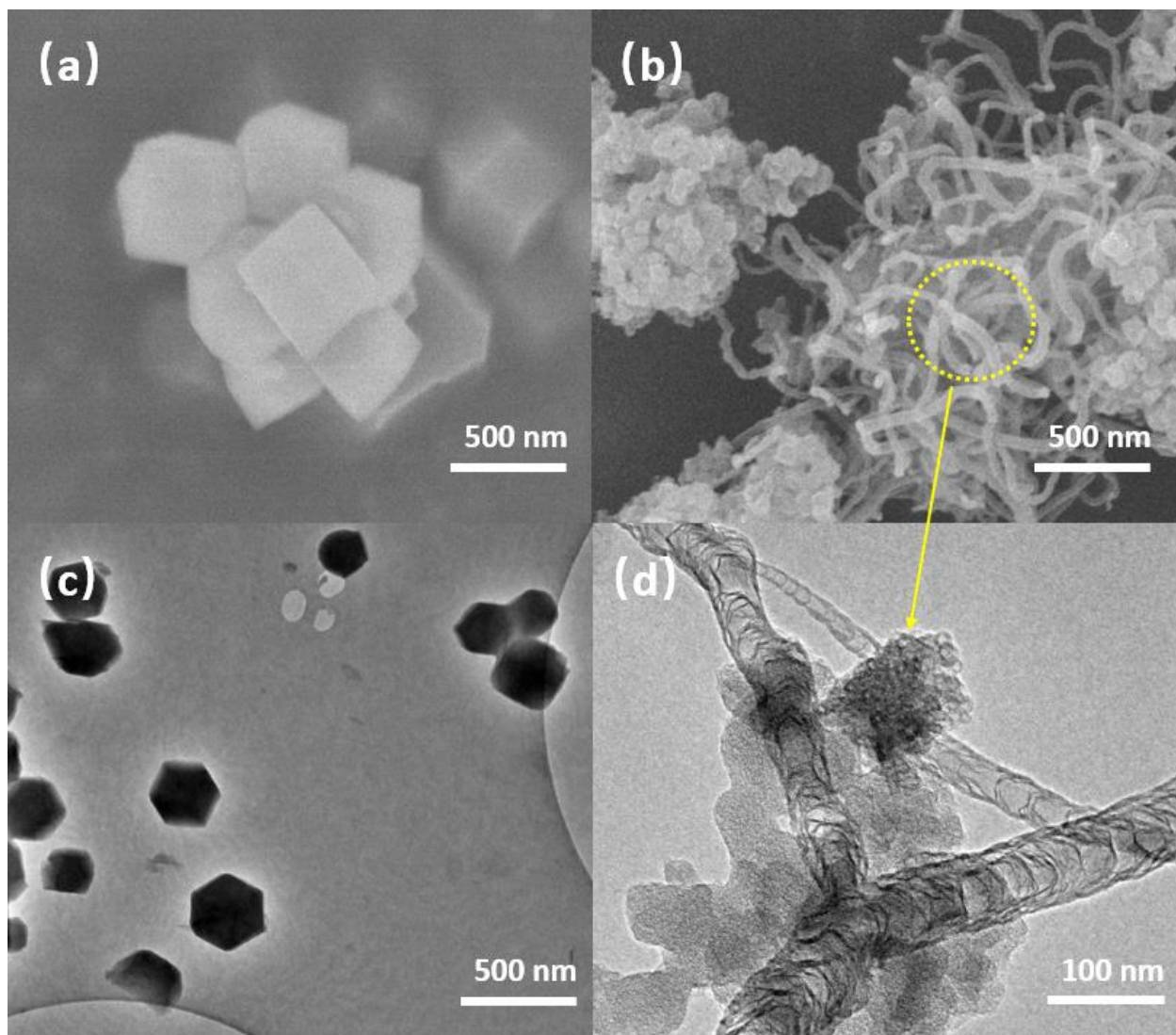


Figure 5. 2 (a) SEM image of Ni@ZIF-8; (b) SEM image of carbonized Ni@ZIF-8 at 900 °C for 6 hours; (c) TEM image of Ni@ZIF-8; (d) TEM image carbonized Ni@ZIF-8 at 900 °C for 6 hours.

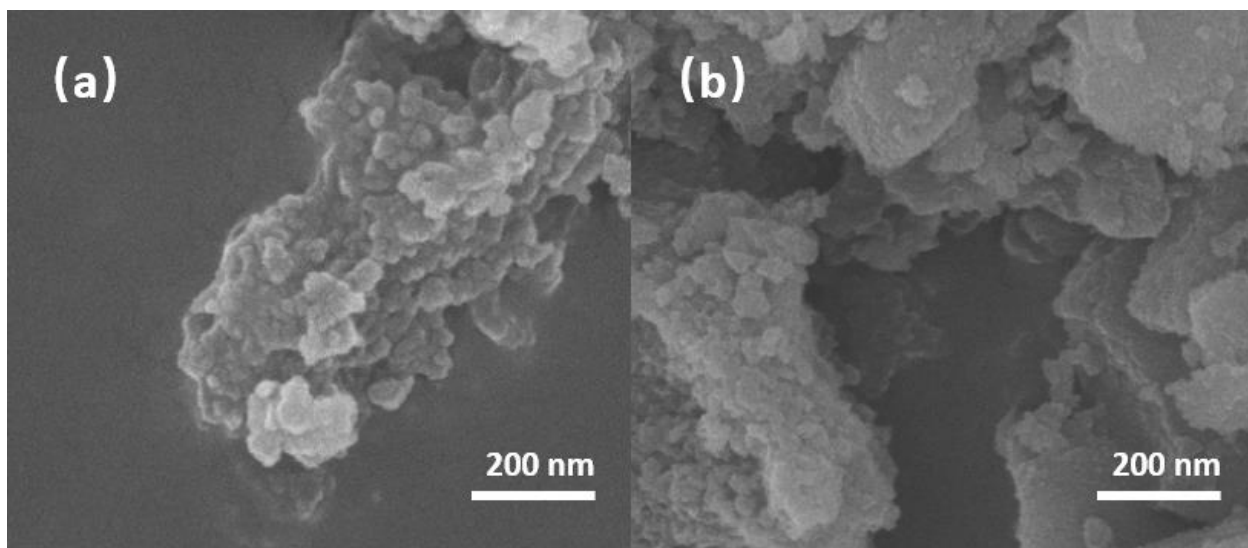


Figure 5. 3 SEM images of (a) carbonized Co@ZIF-8; (b) carbonized Fe@ZIF-8 at 900 °C for 6 hours;

Firstly, the duration and temperature of the carbonization process were optimized at 900 °C for a period of 6 hours. This sample was denoted as CNi@ZIF-8 whilst the sample prior to annealing was denoted as Ni@ZIF-8, respectively. As mentioned in Chapter 4, the crystalline cubic ZIF morphology became spherical at the edges when the annealing temperature was below 900 °C. Likewise, when the annealing temperature increased to 900 °C or above, the original structure collapsed into an amorphous structure (nanowire structure forms in CNi@ZIF-8). Hence, the optimum carbonization temperature and duration are 900 °C and 6 hours. The optimized CNi@ZIF-8 also showed effective catalysis performance (low onset potential and high current density). In detail, as revealed by SEM and TEM (Figure 5.2a, c), the Ni@ZIF-8 as prepared displays a uniform cubic structure with a smooth surface. SEM also confirms high crystallinity and a zeolite-type structure. Following carbonization at 900 °C for 6 hours, the resulting

CNi@ZIF-8 frameworks partially collapsed into nanowires due to the existence of Ni metals (Figure 5.2b, d). The practice of Ni doping serves to prevent the process of aggregation during high-temperature annealing. Additionally, it also acts as the active site for the hydrogen evolution reaction. The same principle is applied to the growth of carbon nanotubes which are derived from the catalytic chemical vapour deposition from the gaseous or liquid carbon precursors.<sup>144</sup> Transition metals (i.e. Ni, Fe and Co) doped at the framework act as a nucleation site where nanowires begin to grow. Ni is the best metal for this purpose compared with Co and Fe which have hardly any wires formed (Figure 5.3).

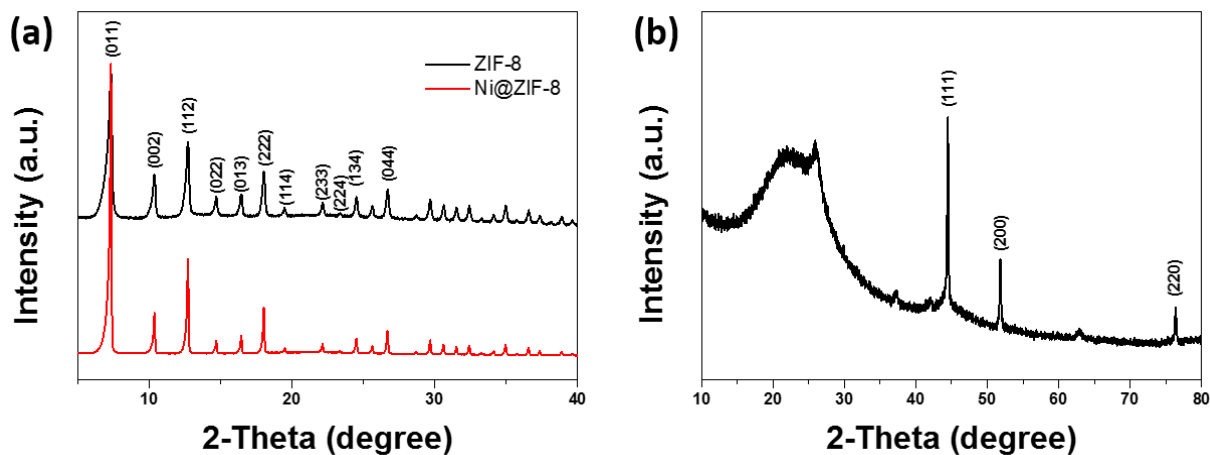


Figure 5. 4 The PXRD diffraction pattern of (a) ZIF-8 and Ni@ZIF-8, (b) CNi@ZIF-8 under Cu radiation.

PXRD patterns act as further proof for structural analysis. Prior to the process of annealing (Figure 5.4a) the peaks of samples with and without Ni doping appeared at the same positions. This was in strong contrast with the baseline. This indicates the high crystallinity of

Ni@ZIF-8 and that Ni nanoparticles were well distributed without disturbing the ZIF structure.<sup>145</sup>

The multiple peaks on the XRD pattern of the synthesized CNi@ZIF-8 (Figure 5.4b) have the typical crystalline structure with Ni-MOF in the previous literature.<sup>146</sup> The characteristic peaks located at 44.5, 51.8 and 76.4 are indexed to the (111), (200), and (220) planes of cubic phase of Ni metal (JCPDS No. 04-0850), respectively. The broad shoulder peak around 25° is ascribed to partially graphitized carbon species.

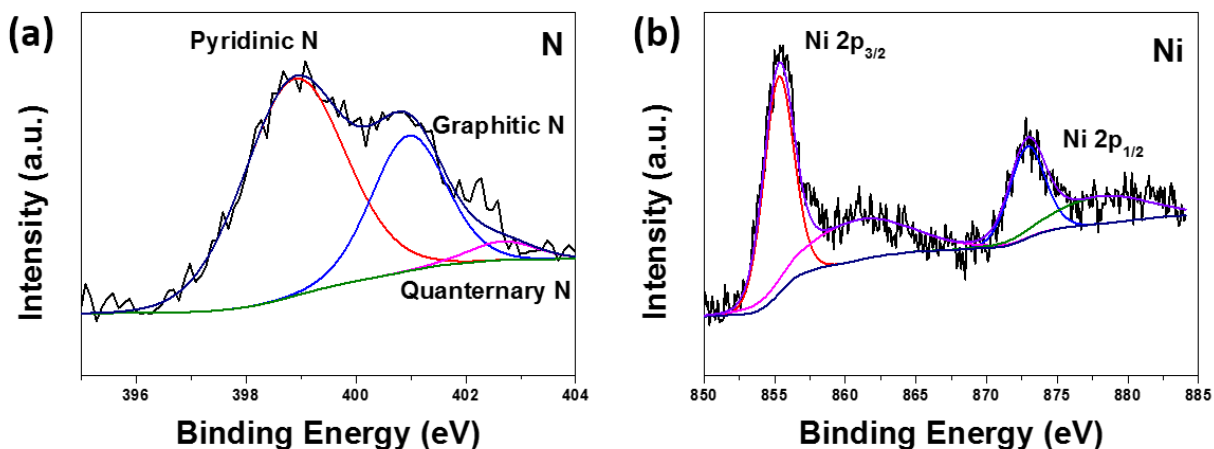


Figure 5. 5 XPS spectra of (a) nitrogen 1s, (b) nickel 2p of CNi@ZIF-8.

The surface composition and electronic states of CNi@ZIF-8 were characterized by XPS. The bonding configuration of nitrogen atoms in CNi@ZIF-8 was characterized by XPS in N1s spectrum. As Figure 5.5a illustrates, there are three distinct peaks at 398.9, 401.0 and 403.5 eV. These can be assigned to pyridinic N, graphitic N and quaternary N,



respectively, which in agreement with the literature.<sup>147</sup> The peak with the lowest binding energy, pyridinic-like nitrogen is attributed to the  $\pi$ -conjugated system with a pair of p-electrons in the six-membered pyridine ring. It is also worth mentioning that the higher pyrolysis temperature will lead to more graphitic N in the N1s high-resolution spectrum.<sup>147</sup> These results demonstrate that the annealing temperature has the greatest impact on the modulation of the chemical state of nitrogen in CNi@ZIF-8. Similarly, the high-resolution peaks observed at 855.3 and 860.9 eV corresponding to the Ni 2p<sub>3/2</sub> level. From the Ni 2p<sub>1/2</sub> level, the peaks were exhibited at 872.9 and 878.1 eV. This corresponds with the statements made in the existing related studies.<sup>148, 149</sup> The existence of these absorption peaks displays a significant level of interaction between Ni species and nitrogen-doped carbon frameworks (Figure 5.5b).<sup>150</sup>

### 5.3.2 LSV performance of carbonized Ni/Co/Fe@ZIF-8

The electrocatalytic HER capability of the catalysts was studied using steady state linear sweep voltammetry (LSV) on a glassy carbon disk electrode in 0.5 M H<sub>2</sub>SO<sub>4</sub>. All of the samples were prepared by carbonization with a heating rate of 5 °C min<sup>-1</sup>. This slower pyrolysis rate (heating rate) can lower the rate at which volatile substances such as methane are produced. It may also assist in the transformation of the ZIF structures into more porous open carbon structures.<sup>151</sup>

The LSV curves of CNi@ZIF-8, CCo@ZIF-8 and CFe@ZIF-8 are illustrated in Figure 5.6. The reference HER performances for 20 wt.%

Pt/C, carbon black and CZIF-8 are also listed in the same figure. Under such conditions, the Pt/C reference displays the best HER activity with the onset overpotential being close to zero. Besides, the CNi@ZIF-8 sample is observed to be highly active for the electrocatalytic HER that provides a close overpotential with the commercial Pt/C catalyst in comparison with CCo@ZIF-8 and CFe@ZIF-8. CCo@ZIF-8 and CFe@ZIF-8 have lower activity levels since they tend to agglomerate together and encompass a smaller specific area, yet CNi@ZIF-8 forms a nanowire structure (Figure 5.2b, d). In this case, these transition metal doped samples have relatively poor catalytic qualities. This is because there are no electron-rich elements, such as boron or phosphorus.

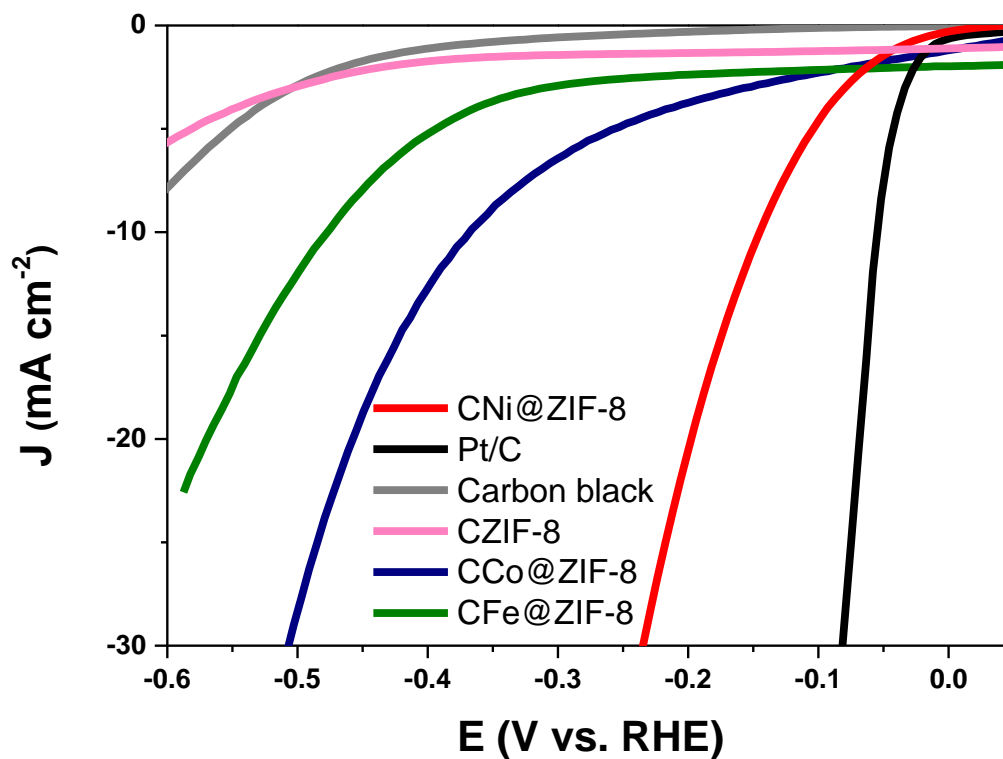


Figure 5. 6 Polarization curves of CNI@ZIF-8, 20 wt.% Pt/C, carbon black, CZIF-8, CCo@ZIF-8 and CFe@ZIF-8.

### 5.3.3 Optimization of carbonized Ni@ZIF-8 for hydrogen evolution reaction

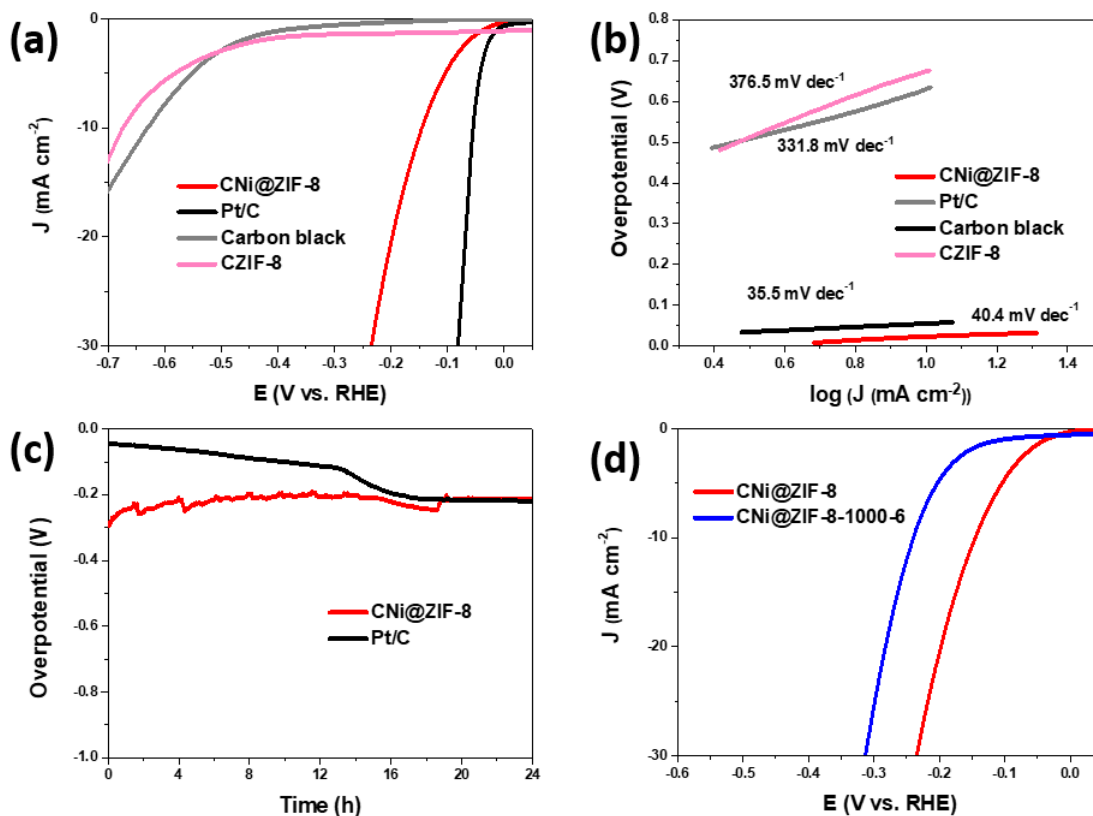


Figure 5. 7 (a) Polarization curves of CNI@ZIF-8, 20 wt.% Pt/C, carbon black and CZIF-8. (b) Tafel plots of CNI@ZIF-8, 20 wt.% Pt/C, carbon black and CZIF-8. (c) V-t curve of CNI@ZIF-8 and 20 wt.% Pt/C up to 24 hours. (d) Polarization curves of carbonized Ni-doped ZIF-8 at 900 °C for 6h and 1000 °C for 6h.

The LSV curve of CNI@ZIF-8 is clearly shown in Figure 5.7a. This is worthy of detailed analysis as it exhibits the most optimal degree of HER performance among CNI@ZIF-8, CCo@ZIF-8 and CFe@ZIF-8. In comparison with 20 wt.% Pt/C, carbon black and CZIF-8, these

curves directly express the various HER performances of CNi@ZIF-8 and reference catalysts at a scan rate of 10 mV s<sup>-1</sup>. Under such conditions, the Pt/C reference exhibits superior HER activity with the onset overpotential being close to zero. Although the commercial 20 wt.% Pt/C outperforms the rest of them, the CNi@ZIF-8 sample is observed to be highly active for the electrocatalytic HER that provides a close overpotential and Tafel slope with the commercial Pt/C catalyst. At a reference current density of 10 mA cm<sup>-2</sup>, the CNi@ZIF-8 required a 141 mV overpotential. 20 wt.% Pt/C requires 55 mV to accomplish the same current density. In addition, CNi@ZIF-8 exhibits an impressive HER activity with a small onset overpotential (~50 mV), beyond which the cathodic current density rapidly rises and visible H<sub>2</sub> bubbles begin to evolve on the electrode surface. However, the bubbles on the electrodes are removed in time in order to prevent their accumulation which would affect the HER tests.

The Tafel slope estimated from the Tafel plots derived from the corresponding polarization curves was used to evaluate the HER kinetics. A Tafel slope of the four samples is plotted in Figure 5.7b. The values are 40.4, 35.5, 376.5, and 331.8 mV dec<sup>-1</sup> for CNi@ZIF-8, 20 wt.% Pt/C, CZIF-8 and carbon black respectively. The results indicate that the HER follows the Volmer-Heyrovsky mechanism.<sup>152, 153</sup> As mentioned previously, additional tests were carried out on 20 wt.% Pt/C (Figure 4.15a); the Tafel slopes calculated from these three new tests were identically 35.5 mV dec<sup>-1</sup>, which is slightly lower than that reported in previous literature (31 mV dec<sup>-1</sup>).<sup>154,155</sup> This data exhibits the same trend as that witnessed with the polarization curves. CNi@ZIF-8 again

displays the close value with the commercial 20 wt.% Pt/C. The exceptionally low Tafel slope of 40.4 mV dec<sup>-1</sup> at a low potential for CNi@ZIF-8 represents nearly a 12% shortage than the commercial 20 wt.% Pt/C. This value compares favorably to those of the majority of the reported nickel-based electrocatalysts in 0.5 M H<sub>2</sub>SO<sub>4</sub> (Table 5.1). According to the classical two-electron-reaction pattern, the HER in acidic media generally proceeds in the following two steps. Firstly, the Volmer reaction ( $\text{H}_3\text{O}^+ + \text{e}^- \rightarrow \text{H}^*_{\text{ads}} + \text{H}_2\text{O}$ ) is the H<sup>+</sup> adsorption step at the Tafel slope of 120 mV dec<sup>-1</sup>. Secondly, the Heyrovsky reaction ( $\text{H}^*_{\text{ads}} + \text{H}_3\text{O}^+ + \text{e}^- \rightarrow \text{H}_2 + \text{H}_2\text{O}$ ) is the desorption step of the hydrogen gas (H<sub>2</sub>), or the mechanism ( $\text{H}^*_{\text{ads}} + \text{H}^*_{\text{ads}} \rightarrow \text{H}_2$ ) is a recombination step at the Tafel slope of 40 mV dec<sup>-1</sup> or 30 mV dec<sup>-1</sup>, respectively.<sup>156</sup> In the case of the Tafel slope of 40.4 mV dec<sup>-1</sup>, this demonstrates that CNi@ZIF-8 catalyzed HER proceeds by a Volmer-Heyrovsky mechanism, where the electrochemical desorption of hydrogen is the rate determining step. Moreover, as Figure 5.7c illustrates, the durability of the CNi@ZIF-8 and 20 wt.% Pt/C during HER catalysis were evaluated by a chronopotentiometry test, where the activity decays are virtually negligible for CNi@ZIF-8, however, the activity of 20 wt.% Pt/C reduces by approximately 25%.

Table 5. 1 Summary of representative HER catalysts in acidic electrolyte.

Catalyst	Electrolyte		Overpotential at 10 mA cm <sup>-2</sup> (mV)	Tafel slope (mV dec <sup>-1</sup> )	Reference
CNi@ZIF-8	0.5 M H <sub>2</sub> SO <sub>4</sub>	M	141	40	This work
NiSe <sub>2</sub> NW/CC	0.5 M H <sub>2</sub> SO <sub>4</sub>	M	145	42	157
CoNi@NC	0.5 M H <sub>2</sub> SO <sub>4</sub>	M	142	105	158
Ni <sub>2</sub> P hollow nanoparticles	0.5 M H <sub>2</sub> SO <sub>4</sub>	M	116	46	159
NiS <sub>2</sub> nanoflake	0.5 M H <sub>2</sub> SO <sub>4</sub>	M	245	79	160
NiSe <sub>2</sub>	0.5 M H <sub>2</sub> SO <sub>4</sub>	M	>235	57	161
NiP <sub>2</sub> NS/CC	0.5 M H <sub>2</sub> SO <sub>4</sub>	M	75	51	162
NiMo/C	0.5 M H <sub>2</sub> SO <sub>4</sub>	M	290 (@2 mA cm <sup>-2</sup> )	55	135

Furthermore, the CNi@ZIF-8 sample is observed to present a better performance than the CNi@ZIF-8-1000-6 counterparts. This is evidenced by its relatively lower overpotential at the same current

density (141 mV vs 242 mV @10 mA cm<sup>-2</sup>) and the larger catalytic current in the same potential window (Figure 5.7d). The results suggest that the metal clustering of the catalysts plays a significant role (higher temperature, more aggregation).

## 5.4 Conclusions

CNi@ZIF-8 electrocatalyst has been effectively synthesized via Ni-doped ZIF-8 carbonization, leading to nitrogen doped and finely dispersed nickel nanoparticles dispersed on porous carbon. The resulting catalyst (CNi@ZIF-8) exhibits superior performance for HER in 0.5 M H<sub>2</sub>SO<sub>4</sub>, achieving a Tafel slope of 40.4 mV dec<sup>-1</sup> with an overpotential of only 141 mV at the reference current density of 10 mA cm<sup>-2</sup>. The main reason for the activity improvement is the nanowires structure that mitigate the aggregation during high-temperature calcination, the high electron conductivity carbon substrate, and the richness of the N-functional groups, along with the dispersion of the fine nickel nanoparticles and large surface area. Meanwhile, the catalysts also gave excellent stability, up to 24 hours with negligible activity decay in an acidic electrolyte. Overall, the approach generates a very effective HER catalyst as a low cost and highly stable alternative to the commercial 20 wt.% Pt/C for hydrogen production.



## Chapter 6. Carbonized Mo@ZIF-67/ZIF-8 as High Performance Electrocatalysts for Hydrogen Evolution Reaction

### 6.1 Introduction

The limited consumption of fossil fuel energy has increased dramatically in scientists' laboratories, in workers' factories, and in people's lives (in terms of cars, daily coal power generation, etc.). Moreover, the associated environmental pollution problems have led to widespread research interest in finding clean and sustainable energy sources.<sup>163, 164</sup> Electrochemical water decomposition is considered to be an effective eco-friendly and sustainable hydrogen production pathway. It also represents a promising method for hydrogen production since the only by-product produced throughout the entire process is water. However, its implementation remains a significant challenge due to the half-cell reaction of water splitting and the hydrogen evolution reaction (HER) at the cathode. This is affected by the essentially inevitable dynamic overpotential. Due to the sluggish kinetics, an effective and stable electrocatalyst is required for the improvement of the energy conversion efficiency.<sup>165</sup> So far, in terms of Pt-based materials and composites, there has been commercial production in both labs and wider industries. However, a low level of abundance, stability and the high cost of such catalysts significantly limits their widespread use. Therefore, the prospect of designing and developing cost effective but efficient and viable alternatives, rather

than the noble metal electrocatalysts described above, is a definite priority.

Transition metal materials, such as metal nanoparticles doped with nitrogen,<sup>166, 167</sup> oxygen,<sup>168</sup> sulfur<sup>169, 170</sup> and phosphorus<sup>171, 172</sup> to re-adjust the electronic arrangement or the use of high-temperature calcination to synthesize electrocatalysts made of carbides are considered to be excellent candidates for electrocatalytic water decomposition.<sup>173, 174</sup> Among them, molybdenum carbide materials have attracted a significant amount of attention and the ascription of positive prospects. This is due to their Pt-like d-band electronic structure and wonderful chemical stability and low cost. For example, Wang's group summarised that it was urgently necessary to develop synthetic strategies which enable a better control of nanostructures and components in order to further increase the activity of the resulting electrocatalysts for HER.<sup>175</sup> In recent years, MOFs, especially ZIFs, has been in the spotlight. This is because they can assist in the development of new materials and nanostructures such as core-shells and hollow structures to promote HER performance. In order to maximize the HER activity of molybdenum carbide, an effective strategy based on nanoscale engineering was further established to expose more catalytic active sites.<sup>176, 177</sup> It is worth noting that nanoscale molybdenum carbides tend to undergo aggregation and precipitation which is caused by relatively high calcination temperatures during their synthesis. To tackle the drawback, nanocrystalline molybdenum carbide was thereby anchored onto conductive carbon supports (calcination of ZIFs), like porous carbon

with nitrogen doping which achieved excellent HER activity and mitigated the drawback of aggregation.<sup>178,179</sup> Doping electrochemically active N-doped molybdenum carbide has been proved to be effective for improving its electrocatalytic activity. This is mainly due to the fact that the N-dopant could interact with H<sup>+</sup> better than C atoms for enhanced H<sup>+</sup> adsorption and the favorable modification of the electronic structures of adjacent Mo and C atoms for improved H desorption from Mo-H.<sup>180,181</sup> As a result, H<sup>+</sup> is easily detached and forms H<sub>2</sub>.

Herein, a facile approach is applied to design a new structure of molybdenum carbide-based electrocatalyst. This is composed of N-doped molybdenum carbide nanoparticles (CMo@ZIF-8). We have shown that the resulting CMo@ZIF-8 catalysts are highly active and the activity remains in a 24h long-term stability test. As expected, the CMo@ZIF-8 presents a good performance in terms of hydrogen production in an acidic electrolyte. The observed catalytic feature would be attributed to the high degree of conductivity of each component in the CMo@ZIF-8 and the Pt-like d-band electronic structure of the Mo-based catalysts.

## **6.2 Methodology**

### **6.2.1 Synthesis methods**

Synthesis of ZIF-8

First, zinc nitrate hexahydrate (12.33 g) was dissolved in 500 mL methanol. Then, 2-methylimidazole (13.59 g) was dissolved in another 500 mL methanol. The latter solution was slowly added to the former in a 1 L wide mouth jar while stirring at room temperature. Stirring proceeded for 2 h, after which the solution was left to settle for 24 h. The clear top solution was drained, and the white precipitate was collected by centrifugation with further methanol washing. The sample was dried in an oven at 80 C for 24 h.

### Synthesis of ZIF-67

Firstly, the cobalt nitrate hexahydrate (7.185 g) was dissolved in 500 mL methanol. Then, 2-methylimidazole (8.106 g) was dissolved in another 500 mL methanol. The later solution was slowly added to the former one in a 1 L wide mouth jar while stirring at room temperature. Stirring proceeded for 2 h and solution was then left for 24h to settle. The top clear solution was drained out and the purple precipitates were collected by centrifugation with further methanol washing. The samples were dried for 24h at 80 °C in an oven.

### Synthesis of Mo@ZIF-8 and CMo@ZIF-8

ZIF-8 (0.46 g) was dissolved in 10 mL deionized water. Sonication and stirring were carried out for 1 h to achieve a homogeneous solution at room temperature. Likewise, ammonium molybdate tetrahydrate ((NH<sub>4</sub>)<sub>6</sub>Mo<sub>7</sub>O<sub>24</sub> 4H<sub>2</sub>O) (2.48 g) was added into 40 mL deionized water with stirring and sonication to form a homogeneous aqueous solution.

Two as-prepared solutions were refluxed at 50 °C for 5 hours in a 100 mL round bottom flask. The harvested solid was washed with water four times and freeze-drying, the precursor was pyrolyzed at 900 °C (heating rate of 5 C min<sup>-1</sup>) in an alumina boat (1 x 1.5 x 5 cm) in a horizontal tube furnace to form carbonized ZIF-8 with Mo doping, termed CMo@ZIF-8. The powders were annealed at 900 C for 6 hours under nitrogen and cooled to room temperature. After carbonization, black solids were collected and ground into fine powder. Mo@ZIF-67 and CMo@ZIF-67 were yielded by the same method but altered ZIF-8 into ZIF-67.

### **6.2.2 Physical characterization**

Powder X-ray diffraction (PXRD, Stoe Stadi-P, Cu-K-alpha and MoK-alpha) was carried out by encapsulation of samples in a 0.5 mm diameter borosilicate glass capillary under ambient conditions. X-ray photoemission spectroscopy (XPS, Al-K-alpha, Thermo Scientific) and transmission electron microscopy (SEM, Jeol) were carried out on carbon tape. Transmission electron microscopy (TEM, Jeol) measurements were completed on a carbon-coated copper TEM grid support.

### **6.2.3 Electrochemical test**

All tests were carried out using an Autolab (Metrohm PGSTAT302N) electrochemical station, using a three-electrode method with a glassy

carbon rotating disk as the working electrode and carbon rod and Ag/AgCl/saturated KCl as counter and reference electrode, respectively, in an acidic electrolyte (0.5 M H<sub>2</sub>SO<sub>4</sub>) at room temperature. All measurements were carried out with a fixed catalyst deposition of  $\sim 0.26 \text{ mg cm}^{-2}$  on a 3 mm diameter (area of  $0.0707 \text{ cm}^{-2}$ ) glassy carbon disk electrode. The catalyst was prepared as follows: 2 mg of sample was dispersed in a 540 mL solution consisting 500 mL of 4:1 v/v water/ethanol and 40 mL of Nafion (5% solution) under sonication. The sonication was carried out up to an hour to get uniform dispersion of catalyst ink, of which 5 mL was micropipetted and dropped on a glassy carbon disk electrode followed by drying at 60 C in the oven. All electrochemical test results are reported with respect to the reference Ag/AgCl. The linear sweep voltammetry (LSV) curves were recorded with voltage sweeping at  $10 \text{ mV s}^{-1}$  in the potential range of +0.0 V to -0.7 V with disk rotating speed of 1600 rpm in 0.5 M H<sub>2</sub>SO<sub>4</sub>. The data were collected after stable CVs were obtained. The measured potentials against Ag/AgCl were converted to RHE using the following relation: in 0.5M H<sub>2</sub>SO<sub>4</sub>,  $E_{(\text{RHE})} = E_{\text{Ag/AgCl}} + 0.059 \text{ pH} + E^{\circ}_{\text{Ag/AgCl}}$ , where  $E^{\circ}_{\text{Ag/AgCl}} = 0.1976 \text{ V}$  at 25 °C and  $E_{\text{Ag/AgCl}}$  is the working potential. The overpotential  $E = E_{(\text{RHE})}$ .

## **6.3 Results and Discussion**

### **6.3.1 Morphology and composition (the formation of carbon nanowires regarding to the size of ZIF structure)**

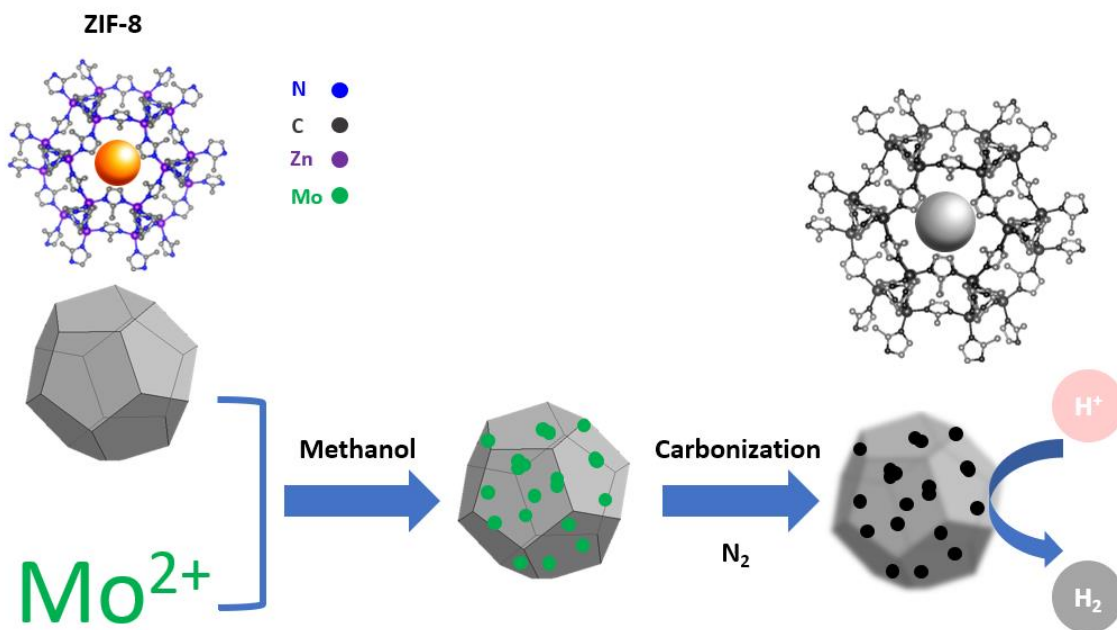


Figure 6. 1 Illustration of the synthesis procedures of carbonized Mo-doped nanoparticles (CMo@ZIF-8).

CMo@ZIF-8 was synthesized using a two-step approach. Firstly, ZIF precursors and molybdenum salt were entirely dissolved in methanol by stirring and reflux. Following this, the solvent was evaporated, and the as-synthesized material was annealed in an inert N<sub>2</sub> atmosphere at 900 °C for 6 hours to yield the final sample. For comparison, the carbonized ZIF without the Mo salt was also prepared. This is denoted as CZIF-8. The procedures are illustrated in Figure 6.1 and explained further in the Experimental section.

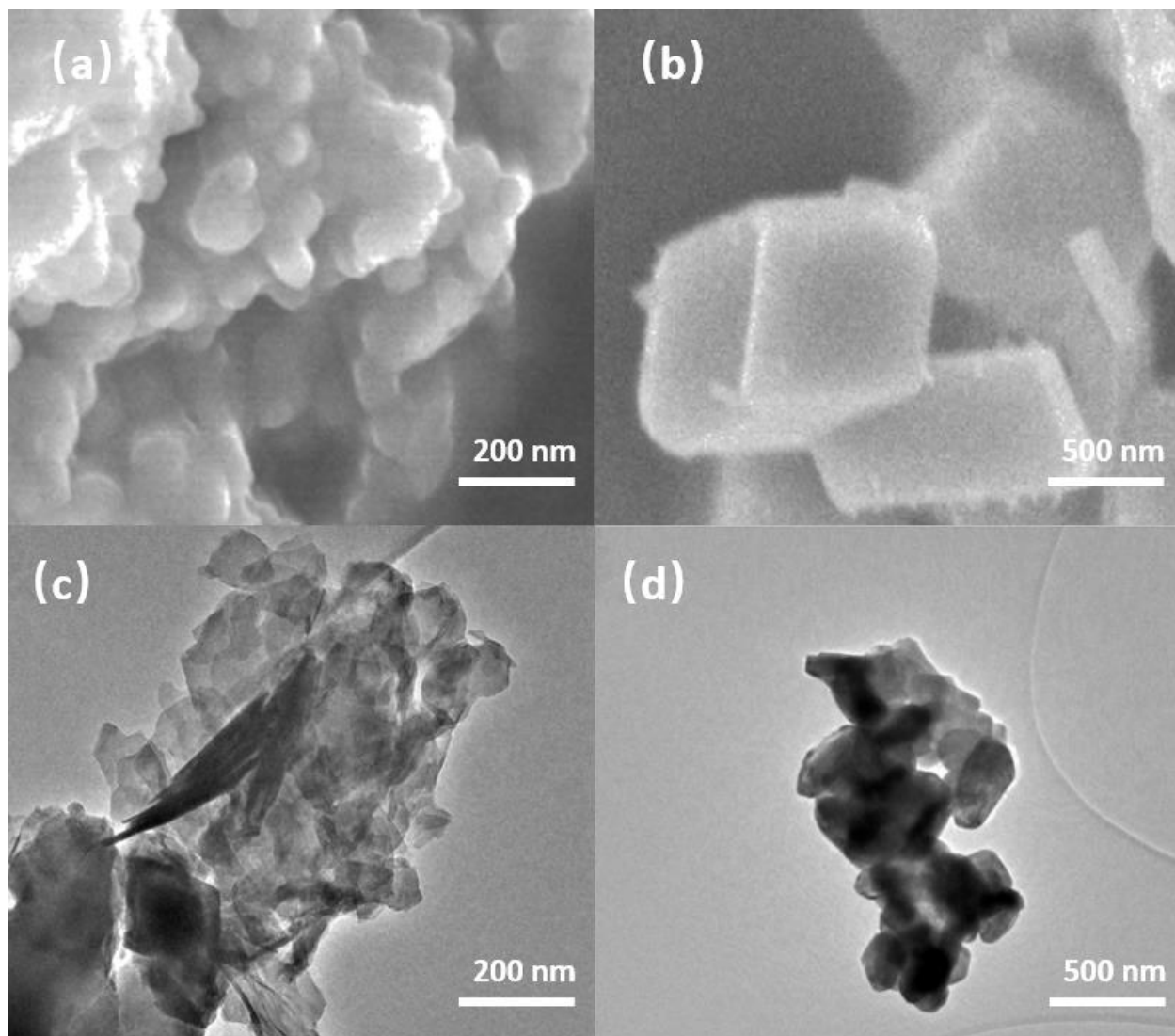


Figure 6. 2 (a) SEM image of Mo@ZIF-8; (b) SEM image of carbonized Ni@ZIF-8 at 900 °C for 6 hours; (c) TEM image of Mo@ZIF-8; (d) TEM image carbonized Mo@ZIF-8 at 900 °C for 6 hours.

The morphology and microstructure of as-prepared CMo@ZIF-8 was first observed by SEM and TEM. CMo@ZIF-8 were synthesized by direct carbonization of Mo-doped ZIF-8 at 900 °C for 6h under inert gas (N<sub>2</sub>) environment. As can be seen from Figure 6.2a, c, the precursor



Mo@ZIF-8 is composed of a uniform micro-sphere with a rough surface and porous texture. On the corresponding pyrolyzed product, CMo@ZIF-8 was mildly aggregated into a slightly larger cubic structure with a relatively smooth and compact surface. (Figure 6.2 b, d). This indicates that the high-temperature (900 °C) annealing procedure could result in a loose porous texture, thus not only increasing the electrolyte-electrode contact points and exposing the more active sites but also providing efficient electron transport and mass transfer to enhance the efficiency of hydrogen evolution reaction eventually.

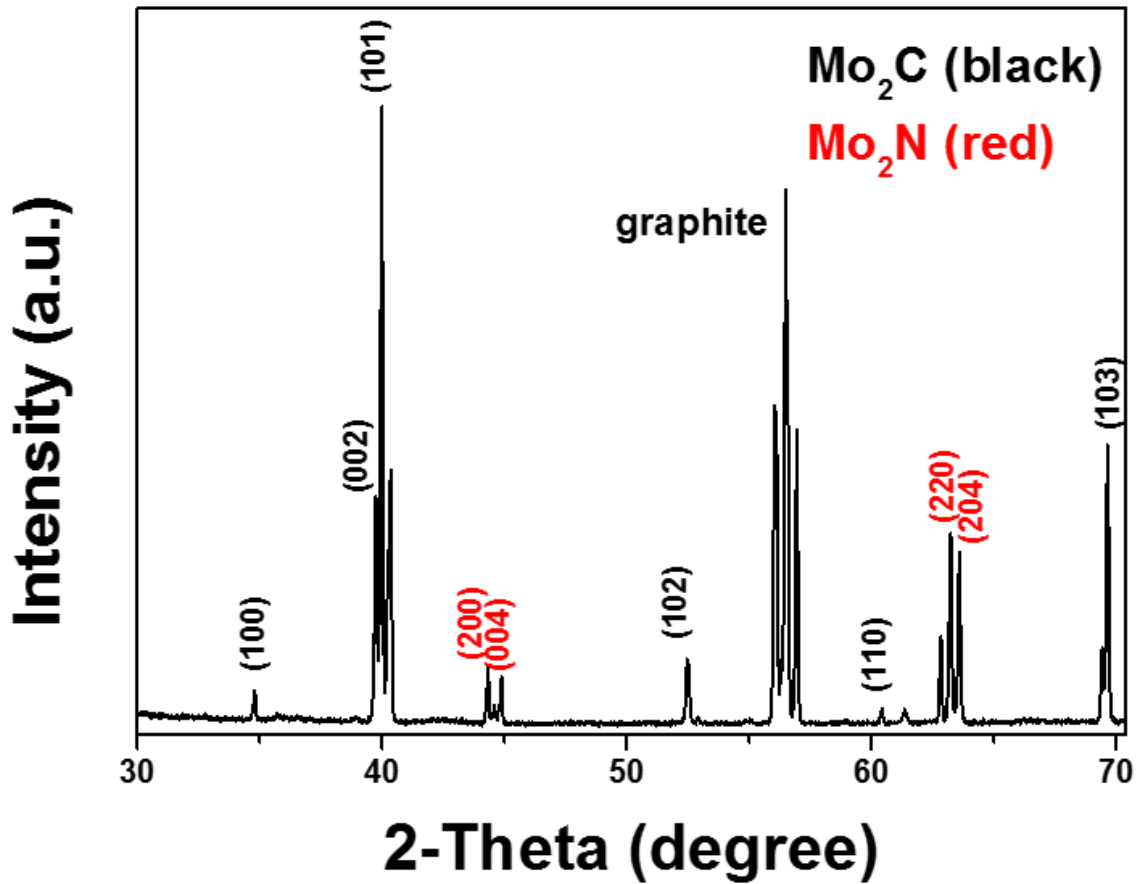


Figure 6. 3 The PXRD diffraction pattern of CMo@ZIF-8.

The crystalline phase composition of as-prepared CMo@ZIF-8 yielded at 900 °C determined by powder X-ray diffraction (Figure 6.3). When the precursor Mo@ZIF-8 is pyrolyzed, the corresponding product CMo@ZIF-8 clearly shows the characteristic diffraction peaks at 34.8°, 39.7°, 40.2°, 52.5°, 61.4° and 69.7° attributed to the (100), (002), (101), (102), (110) and (103) planes of a hexagonal  $\beta$ -Mo<sub>2</sub>C (JCPDS 65-8766), respectively. The majority of the peaks can be matched with hexagonal  $\beta$ -Mo<sub>2</sub>C, which is considered to be the most active molybdenum carbide.<sup>182</sup> The four red signals match the characteristic planes of tetragonal  $\beta$ -Mo<sub>2</sub>N.<sup>183</sup> The signal at 54° can be assigned to the (004) planes of graphite.<sup>184</sup> Additionally, graphite has no discernible impurities such as molybdenum metal, oxides or other carbides.

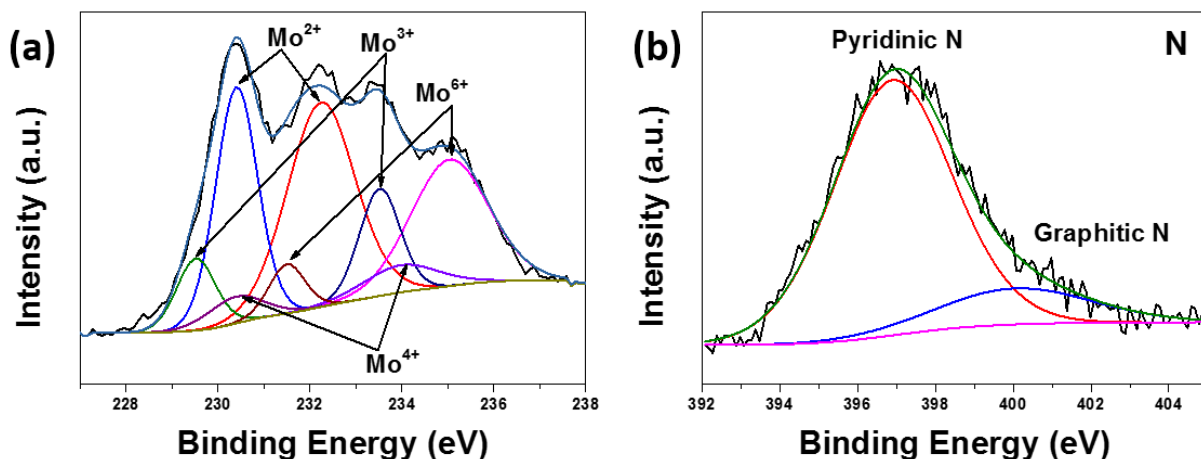


Figure 6. 4 XPS spectra of (a) molybdenum 3d, (b) nitrogen 1s of CPt@ZIF-67.

The surface composition and chemical states of CMo@ZIF-8 were

characterized by XPS. As shown in Figure 6.4a, the high-resolution Mo 3d spectrum can be splitting into four pairs of peaks, corresponding to three oxidation states for Mo species (+2, +3, +4, and +6) existing on the surface of CMo@ZIF-8. Mo<sup>4+</sup> (230.4 and 234.0 eV) and Mo<sup>6+</sup> (231.5 and 235.1 eV) can be distributed to Mo oxides from the surface oxidation of Mo during XPS measurement, as proved in previous reports.<sup>185,186</sup> The peaks at 230.4 and 232.2 eV can be assigned as Mo<sup>2+</sup>, these stand for the molybdenum carbides, which are the active sites for HER.<sup>187</sup> Mo<sup>3+</sup> with binding energies of 229.5 and 233.5 eV represents the nitrides. In other words, N nanoparticles occupy part of the C sites in CMo@ZIF-8.<sup>188</sup> The deconvolution analysis of the detailed N1s spectrum displays the predominant contribution from pyridinic nitrogen with some minor contribution from graphitic nitrogen (Figure 6.4b). They remain at 396.9 and 400.1 eV, respectively. The peak at 396.9 eV could be assigned to the N 1s signal which is related to N–Mo bonding. This is characteristic of molybdenum nitride.<sup>189</sup> Therefore, the XPS analysis provides evidence for the possible N-doping in CMo@ZIF-8.

### 6.3.2 The LSV performance of carbonized Mo@ZIF-67/ZIF-8 for hydrogen evolution reaction

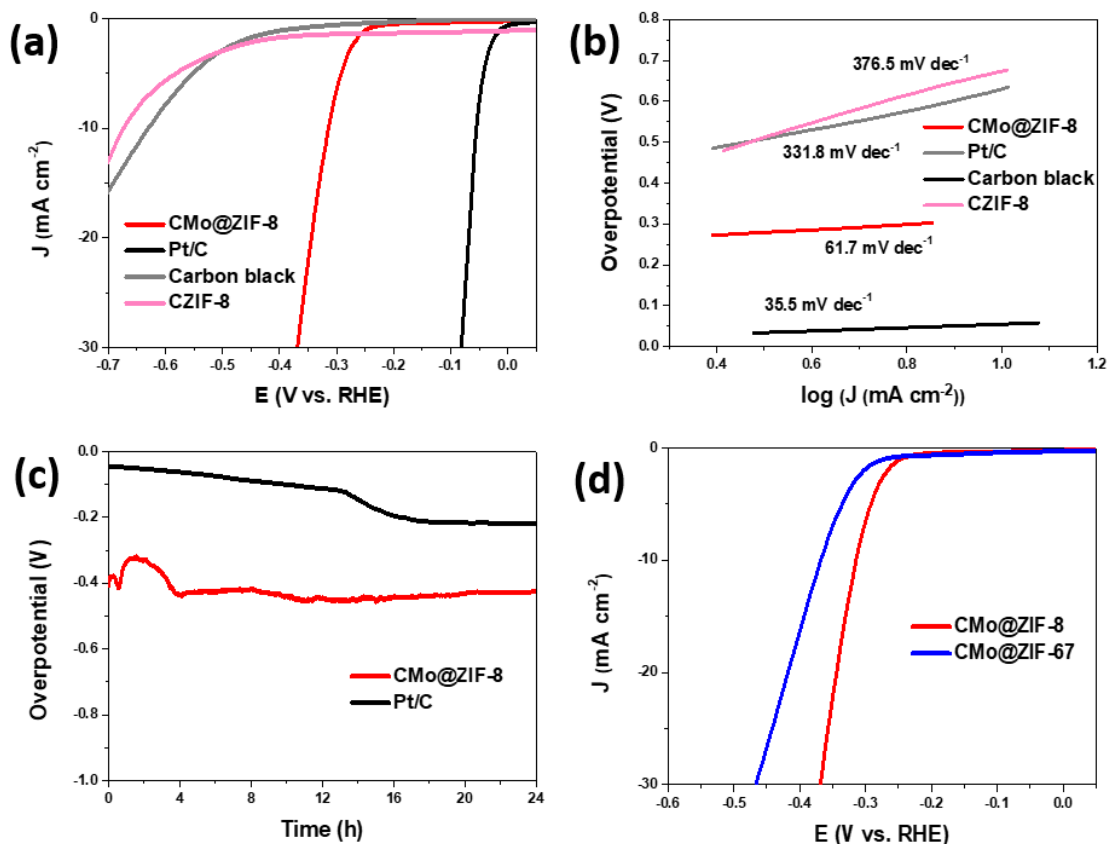


Figure 6. 5 (a) Polarization curves of CMo@ZIF-8, 20 wt.% Pt/C, carbon black and CZIF-8. (b) Tafel plots of CMo@ZIF-8, 20 wt.% Pt/C, carbon black and CZIF-8. (c) V-t curve of CMo@ZIF-8 and 20 wt.% Pt/C up to 24 hours. (d) Polarization curves of carbonized Mo-doped ZIF-8 and Mo-doped ZIF-67 at 900 °C for 6h.

The electrocatalytic HER performance of CMo@ZIF-8 in acidic electrolytes was assessed. Catalyst powder was dispersed in a mixed ethanol/ water (4:1 v/v water/ ethanol) solution with the addition of a Nafion binder. Following the process of sonication into a homogeneous

solution, the catalyst ink was then drop-cast onto a glassy carbon electrode to achieve an area loading of  $\sim 0.26 \text{ mg cm}^{-2}$ . For the purpose of benchmarking, commercial 20 wt. % Pt/C, carbon black and CZIF-8 were also included for the electrochemical measurements, side by side. Figure 6.5a illustrates the HER polarization curve in 0.5 M  $\text{H}_2\text{SO}_4$  and CMo@ZIF-8 exhibits a significant degree of HER activity. It only requires an overpotential of 310 mV to deliver a current density of  $10 \text{ mA cm}^{-2}$ .

As known, the Tafel slope indicates the intrinsic reactivity of HER electrocatalysts whilst the smaller Tafel slope suggests a more facile charge-transfer and higher kinetics of HER. In these circumstances, the Tafel slope which originated from the polarization curves is linked to the Tafel equation ( $\eta = b \log(j) + a$ , where  $j$  is the current density and  $b$  is the gradient of the equation or the Tafel slope). This is illustrated in Figure 6.5b. The Pt/C displays a Tafel slope of  $35.5 \text{ mV dec}^{-1}$ , a marginally poorer result compared to those of the existing literature. However, additional tests were carried out on 20 wt.% Pt/C to provide strong evidence for the reliability of our electrochemical measurements.<sup>190</sup>

It is notable that CMo@ZIF-8 achieves a small Tafel slope of  $60.7 \text{ mV dec}^{-1}$ , which is lower than those of  $\text{Mo}_2\text{C}/\text{NC750}$  ( $80 \text{ mV dec}^{-1}$ ) and MoDCA-2 ( $68 \text{ mV dec}^{-1}$ ) reported  $\text{Mo}_2\text{C}$ -based electrocatalysts (Table 6.1). The smaller Tafel slope indicates a faster proton discharge kinetic and superior HER activity for the CMo@ZIF-8 sample. In Figure 6.5c

the stability test depicts there was almost no performance degradation for up to 24h.

Table 6. 1 Summary of representative HER catalysts in acidic electrolyte.

Catalyst	Electrolyte	Overpotential at 10 mA cm <sup>-2</sup> (mV)	Tafel slope (mV dec <sup>-1</sup> )	Reference
CMo@ZIF-8	0.5 M H <sub>2</sub> SO <sub>4</sub>	310	62	This work
MoDCA-2	0.5 M H <sub>2</sub> SO <sub>4</sub>	209	68	191
Mo <sub>2</sub> C	0.5 M H <sub>2</sub> SO <sub>4</sub>	210	56	192
Mo <sub>2</sub> C nanoribbon/N-G film	0.5 M H <sub>2</sub> SO <sub>4</sub>	162	57	87
Mo <sub>2</sub> C/NC750		~ 145	80	193
Mo <sub>2</sub> C NPs	0.5 M H <sub>2</sub> SO <sub>4</sub>	198	56	194
MoCN NPs	0.5 M H <sub>2</sub> SO <sub>4</sub>	140	46	195
MoC <sub>x</sub> nano-octahedrons	0.5 M H <sub>2</sub> SO <sub>4</sub>	142	53	196
Mo <sub>2</sub> C	0.5 M	160	53	197

nanowires	H <sub>2</sub> SO <sub>4</sub>				
nw-W4Mo	0.5 M H <sub>2</sub> SO <sub>4</sub>	150	52	198	
β-Mo <sub>2</sub> C	0.1 M HClO <sub>4</sub>	180-220	120	199	

### 6.3.3 Optimization HER activity of carbonized Mo@ZIF based catalyst

Additionally, the CMo@ZIF-8 sample is observed to present a higher performance level than the CMo@ZIF-67 counterparts, evidenced by its relatively lower degree of overpotential at the same current density (310 mV vs 370 mV @10 mA cm<sup>-2</sup>) and larger catalytic current in the same potential window (Figure 6.5d). This observation implies that a synergistic effect could exist between cobalt and molybdenum carbide in CMo@ZIF-67 yet the HER activity performs lower than CMo@ZIF-8. This phenomenon reveals that the incorporation of molybdenum carbide cannot always enhance HER performance although metallic Co has a high level of conductivity.

## 6.4 Conclusions

The CMo@ZIF-8 electrocatalyst has been effectively synthesized via Mo-doped ZIF-8 calcination. The resulting electrocatalyst possesses finely dispersed molybdenum nanoparticles which are dispersed on porous carbon. The resulting catalyst (CMo@ZIF-8) exhibits excellent

performance for HER in 0.5 M H<sub>2</sub>SO<sub>4</sub>, achieving a Tafel slope of 61.7 mV dec<sup>-1</sup> with an overpotential of only 310 mV at the reference current density of 10 mA cm<sup>-2</sup>. The improvement is partly attributed to a similar d-band electronic structure with Pt along with the high level of electron conductivity in the carbon substrate. Meanwhile, the catalysts also provided an excellent level of stability for up to 24 hours with no performance loss in an acidic electrolyte. Overall, the approach generates a highly effective HER catalyst as a low cost and highly stable electrocatalyst for HER.



## Chapter 7. Conclusions

A series of effective, low-cost and stable transition metal doped ZIF-67/ZIF-8 electrocatalysts for hydrogen evolution reaction were developed based on the high-temperature carbonization method.

(1) A CPt@ZIF-67 bimetallic catalyst anchored on porous carbon exhibited superior HER performance in 0.5 M H<sub>2</sub>SO<sub>4</sub>, even outperforms the commercial 20 wt.% Pt/C. Furthermore, It achieves a Tafel slope of 27.1 mV dec<sup>-1</sup> with an overpotential of only 50 mV at the reference current density of 10 mA cm<sup>-2</sup>, which is four times of the mass-specific energy density of the commercial counterpart (20 wt.% Pt/C), even at a much lower Pt loading of 5 wt.% and a quarter of the noble metal (Pt) content. The extraordinary performance is attributed to the low the d-band centre based on the smooth charge transfer of metal clusters, the high electron conductivity of the porous carbon support, and the richness of the N-functional groups, along with the dispersion of the metal nanoparticles and the large surface area. Meanwhile, the catalysts also possessed excellent stability, up to 24 hours with negligible loss of activity in an acidic electrolyte. (Chapter 4)

(2) A facile approach was used to manufacture CNi@ZIF-8 via direct-annealing of Ni-doped ZIF-8 (this is achieved by simply mixing the Ni salt and ZIF-8). The resulting catalyst exhibits a superior degree of performance for HER in 0.5 M H<sub>2</sub>SO<sub>4</sub>, achieving a Tafel slope of 40.4 mV dec<sup>-1</sup> with an overpotential of only 141 mV at the reference current density of 10 mA cm<sup>-2</sup>. In the meantime, the catalysts also offered

excellent stability with up to 24 hours with negligible activity decay in an acidic electrolyte. The Ni metal nanoparticles are applied and anchored on the carbon support (ZIF-8) during the pyrolysis process. This leads to the high degree of activity and durability of CNi@ZIF-8 in HER. Not only does the dispersion of Ni nanoparticles have the property of high conductivity, but it also mitigates the aggregation and form of the nanowires structure to enhance the surface area and active site density of CNi@ZIF-8. CFe@ZIF-8 and CCo@ZIF-8 are also generated under the same methods and conditions yet no nanowire structure is created. Hence, Fe and Co nanoparticles cannot prevent high-temperature agglomeration. Overall, Ni-doped ZIF electrocatalysts are promising alternatives for the commercial 20 wt.% Pt/C for hydrogen production. This is due to their low cost and highly stable properties. (Chapter 5)

(3) The CMo@ZIF-8 catalyst exhibited excellent HER activity and durability via the carbonization of Mo-doped ZIF-8. The optimized electrocatalyst CMo@ZIF-8, which required relatively low overpotentials of 310 mV to produce a current density of 10 mA cm<sup>-2</sup> and low Tafel slope (61.7 mV dec<sup>-1</sup>). At the same time, there was no performance degradation in a durability test of up to 24h. The similar d-band electronic structure of Pt reveals a high degree of HER performance. It is worth noting that CMo@ZIF-8 performed better than CCo@ZIF-67 as evidenced by its relatively lower overpotential at the same current density (310 mV vs 370 mV @10 mA cm<sup>-2</sup>). This observation implies that a synergistic effect (CMo@ZIF-67 contains both Mo and Co) could exist between cobalt and molybdenum carbide

in CMo@ZIF-67. However, HER performance is lower than CMo@ZIF-8. This observation explains that the synergistic effect will not always improve the intrinsic properties of the resulting electrocatalysts for HER. (Chapter 6)

## Chapter 8. References

- 
- (1) S. Chu and A. Majumdar, *Nature*, 2012, **488**, 294–303.
  - (2) T. Nakata, *Transp. Res. Part D Transp. Environ.*, 2000, **5**, 373–383.
  - (3) V. Khare, S. Nema and P. Baredar, *Renew. Sustain. Energy Rev.*, 2016, **58**, 23–33.
  - (4) N. L. Panwar, S. C. Kaushik and S. Kothari, *Renew. Sustain. Energy Rev.*, 2011, **15**, 1513–1524.
  - (5) K. J. Jeon, H. R. Moon, A. M. Ruminski, B. Jiang, C. Kisielowski, R. Bardhan and J. J. Urban, *Nat. Mater.*, 2011, **10**, 286–290.
  - (6) C. C. L. McCrory, S. Jung, I. M. Ferrer, S. M. Chatman, J. C. Peters and T. F. Jaramillo, *J. Am. Chem. Soc.*, 2015, **137**, 4347–4357.
  - (7) F. E. Osterloh, *Chem. Soc. Rev.*, 2013, **42**, 2294–2320.
  - (8) G. Zhao, K. Rui, S. X. Dou and W. Sun, *Adv. Funct. Mater.*, 2018, **28**, 1–26.
  - (9) O. Ajayi-Oyakhire, *Inst. Gas Eng. Manag.*, 2012, 18.
  - (10) J. M. Ogden, *Annu. Rev. Energy Environ.*, 1999, **24**, 227–279.
  - (11) M. Fang, G. Dong, R. Wei and J. C. Ho, *Adv. Energy Mater.*, 2017, **7**, 1–25.
  - (12) C. C. L. McCrory, S. Jung, I. M. Ferrer, S. M. Chatman, J. C. Peters and T. F. Jaramillo, *J. Am. Chem. Soc.*, 2015, **137**, 4347–4357.
  - (13) S. Anantharaj, P. E. Karthik and S. Kundu, *J. Mater. Chem. A*, 2015, **3**, 24463–24478.
  - (14) Zhang, *Chem. Soc. Rev.*, 2015, **44**, 5148–5180.
  - (15) Z. Lu, H. Wang, D. Kong, K. Yan, P. C. Hsu, G. Zheng, H. Yao, Z. Liang, X. Sun and Y. Cui, *Nat. Commun.*, 2014, **5**, 1–7.
  - (16) S. Gadipelli, T. Zhao, S. A. Shevlin and Z. Guo, *Energy Environ. Sci.* 2016, **9**, 1661–1667.
  - (17) K. S. Park, Z. Ni, A. P. Côté, J. Y. Choi, R. Huang, F. J. Uribe-Romo, H. K.

- 
- Chae, M. O'Keeffe and O. M. Yaghi, *Proc. Natl. Acad. Sci.* 2006, **103**, 10186–10191.
- (18) Z. Hu and M. P. Srinivasan, *Microporous Mesoporous Mater.* 2001, **43**, 267–275.
- (19) P. T. Hsieh, Y. C. Chen, K. S. Kao and C. M. Wang, *Appl. Phys. A Mater. Sci. Process.* 2008, **90**, 317–321.
- (20) T. Yu, Y. Zhu, X. Xu, Z. Shen, P. Chen, C. T. Lim, J. T. L. Thong and C. H. Sow, *Adv. Mater.* 2005, **17**, 1595–1599.
- (21) F. H. Allen, O. Kennard, D. G. Watson, L. Brammer, A. G. Orpen and R. Taylor, *J. Chem. Soc. Perkin Trans. 2* 1987, **S1**, 1695–1914.
- (22) E. Kemppainen, A. Bodin, B. Sebok, T. Pedersen, B. Seger, B. Mei, D. Bae, P. C. K. Vesborg, J. Halme, O. Hansen, P. D. Lund and I. Chorkendorff, *Energy Environ. Sci.*, 2015, **8**, 2991–2999.
- (23) J. Duan, S. Chen and C. Zhao, *Nat. Commun.*, 2017, **8**, 15341.
- (24) W. Liu, E. Hu, H. Jiang, Y. Xiang, Z. Weng, M. Li, Q. Fan, X. Yu, E. I. Altman and H. Wang, *Nat. Commun.*, 2016, **7**, 10771.
- (25) J. Staszak-Jirkovský, C. D. Malliakas, P. P. Lopes, N. Danilovic, S. S. Kota, K. C. Chang, B. Genorio, D. Strmcnik, V. R. Stamenkovic, M. G. Kanatzidis and N. M. Markovic, *Nat. Mater.*, 2016, **15**, 197–203.
- (26) Y. J. Tang, M. R. Gao, C. H. Liu, S. L. Li, H. L. Jiang, Y. Q. Lan, M. Han and S. H. Yu, *Angew. Chemie - Int. Ed.*, 2015, **54**, 12928–12932.
- (27) J. Sen Li, Y. Wang, C. H. Liu, S. L. Li, Y. G. Wang, L. Z. Dong, Z. H. Dai, Y. F. Li and Y. Q. Lan, *Nat. Commun.*, 2016, **7**, 11204.
- (28) D. V. Esposito, S. T. Hunt, A. L. Stottlemyer, K. D. Dobson, B. E. McCandless, R. W. Birkmire and J. G. Chen, *Angew. Chemie - Int. Ed.*, 2010, **49**, 9859–9862.

- 
- (29) P. Zhang, X. W. (David) Lou, P. An, H. Zhang, J. Dong, W. Zhou and B. Y. Guan, *Sci. Adv.*, 2018, **4**, 6657.
- (30) H. Yin, S. Zhao, K. Zhao, A. Muqsit, H. Tang, L. Chang, H. Zhao, Y. Gao and Z. Tang, *Nat. Commun.*, 2015, **6**, 6430.
- (31) A. B. Laursen, K. R. Patraju, M. J. Whitaker, M. Retuerto, T. Sarkar, N. Yao, K. V. Ramanujachary, M. Greenblatt and G. C. Dismukes, *Energy Environ. Sci.*, 2015, **8**, 1027–1034
- (32) H. Fei, J. Dong, M. J. Arellano-Jiménez, G. Ye, N. Dong Kim, E. L. G. Samuel, Z. Peng, Z. Zhu, F. Qin, J. Bao, M. J. Yacaman, P. M. Ajayan, D. Chen and J. M. Tour, *Nat. Commun.*, 2015, **6**, 8668.
- (33) N. Yabuuchi, K. Kubota, M. Dahbi and S. Komaba, *Chem. Rev.*, 2014, **114**, 11636–11682.
- (34) S. A. Abbas, M. I. Iqbal, S. H. Kim and K. D. Jung, *Electrochim. Acta*, 2017, **227**, 382–390.
- (35) L. Wang, Y. Li, M. Xia, Z. Li, Z. Chen, Z. Ma, X. Qin and G. Shao, *J. Power Sources*, 2017, **347**, 220–228.
- (36) D. Y. Chung, J. W. Han, D. H. Lim, J. H. Jo, S. J. Yoo, H. Lee and Y. E. Sung, *Nanoscale*, 2015, **7**, 5157–5163.
- (37) P. A. Frey and G. H. Reed, *ACS Chem. Biol.*, 2012, **7**, 1477–1481.
- (38) J. Mohammed-Ibrahim and S. Xiaoming, *J. Energy Chem.*, 2019, **34**, 111–160.
- (39) Q. Liu, Z. Pu, A. M. Asiri and X. Sun, *Electrochim. Acta*, 2014, **149**, 324–329.
- (40) Y. Yang, Z. Lun, G. Xia, F. Zheng, M. He and Q. Chen, *Energy Environ. Sci.*, 2015, **8**, 3563–3571.

- 
- (41) Q. Liu, J. Tian, W. Cui, P. Jiang, N. Cheng, A. M. Asiri and X. Sun, *Angew. Chemie - Int. Ed.*, 2014, **53**, 6710–6714.
- (42) K. Xu, H. Cheng, H. Lv, J. Wang, L. Liu, S. Liu, X. Wu, W. Chu, C. Wu and Y. Xie, *Adv. Mater.*, 2018, **30**, 1–6.
- (43) R. S. Datta, F. Haque, M. Mohiuddin, B. J. Carey, N. Syed, A. Zavabeti, B. Zhang, H. Khan, K. J. Berean, J. Z. Ou, N. Mahmood, T. Daeneke and K. Kalantar-Zadeh, *J. Mater. Chem. A*, 2017, **5**, 24223–24231.
- (44) J. Kibsgaard and T. F. Jaramillo, *Angew. Chemie - Int. Ed.*, 2014, **53**, 14433–14437.
- (45) D. V. Esposito, S. T. Hunt, Y. C. Kimmel and J. G. Chen, *J. Am. Chem. Soc.*, 2012, **134**, 3025–3033.
- (46) Y. Wang, S. Song, V. Maragou, P. K. Shen and P. Tsiakaras, *Appl. Catal. B Environ.*, 2009, **89**, 223–228.
- (47) L. Liao, S. Wang, J. Xiao, X. Bian, Y. Zhang, M. D. Scanlon, X. Hu, Y. Tang, B. Liu and H. H. Girault, *Energy Environ. Sci.*, 2014, **7**, 387–392.
- (48) J. Duan, S. Chen, M. Jaroniec and S. Z. Qiao, *ACS Catal.*, 2015, **5**, 5207–5234.
- (49) J. Deng, P. Ren, D. Deng, L. Yu, F. Yang and X. Bao, *Energy Environ. Sci.*, 2014, **7**, 1919–1923.
- (50) J. Zhang and L. Dai, *Angew. Chemie - Int. Ed.*, 2016, **55**, 13296–13300.
- (51) Y. Zheng, Y. Jiao, L. H. Li, T. Xing, Y. Chen, M. Jaroniec and S. Z. Qiao, *ACS Nano*, 2014, **8**, 5290–5296.
- (52) K. Qu, Y. Zheng, Y. Jiao, X. Zhang, S. Dai and S. Z. Qiao, *Adv. Energy Mater.*, 2017, **7**, 1602068.
- (53) H. Lee, S. M. Dellatore, W. M. Miller, P. B. Messersmith, *Science*, 2007,

---

**318**, 426–430.

(54) W. Cui, Q. Liu, N. Cheng, A. M. Asiri and X. Sun, *Chem. Commun.*, 2014, **50**, 9340–9342.

(55) C. Xu, S. Peng, C. Tan, H. Ang, H. Tan, H. Zhang and Q. Yan, *J. Mater. Chem. A*, 2014, **2**, 5597–5601.

(56) N. Cheng, S. Stambula, D. Wang, M. N. Banis, J. Liu, A. Riese, B. Xiao, R. Li, T. K. Sham, L. M. Liu, G. A. Botton and X. Sun, *Nat. Commun.* 2016, **7**, 13638.

(57) Q. Yang, W. Liu, B. Wang, W. Zhang, X. Zeng, C. Zhang, Y. Qin, X. Sun, T. Wu, J. Liu, F. Huo and J. Lu, *Nat. Commun.* 2017, **8**, 14429–14437.

(58) Y. Zhai, D. Pierre, R. Si, W. Deng, P. Ferrin, A. U. Nilekar, G. Peng, J. A. Herron, D. C. Bell, H. Saltsburg, M. Mavrikakis and M. Flytzani-Stephanopoulos, *Science*, 2010, **329**, 1633–1637.

(59) Z. Cao, Q. Chen, J. Zhang, H. Li, Y. Jiang, S. Shen, G. Fu, B. A. Lu, Z. Xie and L. Zheng, *Nat. Commun.*, 2017, **8**, 15131.

(60) J. Greeley, T. F. Jaramillo, J. Bonde, I. Chorkendorff and J. K. Nørskov, *Nat. Mater.* 2006, **5**, 909–913.

(61) S. Bai, C. Wang, M. Deng, M. Gong, Y. Bai, J. Jiang and Y. Xiong, *Angew. Chemie - Int. Ed.* 2014, **53**, 12120–12124.

(62) M. Ledendecker, S. Krickalderön, C. Papp, H. P. Steinrück, M. Antonietti and M. Shalom, *Angew. Chemie - Int. Ed.*, 2015, **54**, 12361–12365.

(63) H. Fei, Y. Yang, Z. Peng, G. Ruan, Q. Zhong, L. Li, E. L. G. Samuel and J. M. Tour, *ACS Appl. Mater. Interfaces.* 2015, **7**, 8083–8087.

(64) S. Chen, J. Duan, M. Jaroniec and S. Z. Qiao, *Angew. Chemie - Int. Ed.* 2013, **52**, 13567–13570.

(65) Y. J. Tang, Y. Wang, X. L. Wang, S. L. Li, W. Huang, L. Z. Dong, C. H. Liu, Y.



- 
- F. Li and Y. Q. Lan, *Adv. Energy Mater.*, 2016, **6**, 160116.
- (66) Y. Pan, K. Sun, S. Liu, X. Cao, K. Wu, W. C. Cheong, Z. Chen, Y. Wang, Y. Li, Y. Liu, D. Wang, Q. Peng, C. Chen and Y. Li, *J. Am. Chem. Soc.*, 2018, **140**, 2610–2618.
- (67) B. Y. Xia, Y. Yan, N. Li, H. Bin Wu, X. W. D. Lou and X. Wang, *Nat. Energy* 2016, **1**, 15006.
- (68) H. Ataee-Esfahani, L. Wang, Y. Nemoto and Y. Yamauchi, *Chem. Mater.* 2010, **22**, 6310–6318.
- (69) L. Yu, B. Y. Xia, X. Wang and X. W. Lou, *Adv. Mater.* 2016, **28**, 92–97.
- (70) S. Dang, Q. L. Zhu and Q. Xu, *Nat. Rev. Mater.* 2017, **3**, 1–14.
- (71) G. Kresse and J. Furthmüller, *Comput. Mater. Sci.* 1996, **6**, 15–50.
- (72) G. Kresse and J. Furthmüller, *Phys. Rev. B* 1996, **54**, 11169–11186.
- (73) J. P. Perdew, K. Burke and M. Ernzerhof, *Phys. Rev. Lett.* 1996, **77**, 3865–3868.
- (74) P. E. Blöchl, *Phys. Rev. B* 1994, **50**, 17953–17979.
- (75) D. Joubert, *Phys. Rev. B* 1999, **59**, 1758–1775.
- (76) S. Dudarev and G. Botton, *Phys. Rev. B* 1998, **57**, 1505–1509.
- (77) L. Wang, T. Maxisch and G. Ceder, *Phys. Rev. B* 2006, **73**, 195107–195102.
- (78) J. K. Nørskov, T. Bligaard, A. Logadottir, J. R. Kitchin, J. G. Chen, S. Pandelov and U. Stimming, *J. Electrochem. Soc.* 2005, **152**, J23–J26.
- (79) K. Miwa and A. Fukumoto, *Phys. Rev. B* 2002, **65**, 155114–155120.
- 80 S. Gadipelli and Z. X. Guo, *ChemSusChem* 2015, **8**, 2123–2132.
- (81) D. Yu, E. Shamsaei, J. Yao, T. Xu and H. Wang, *Inorg. Chem. Front.* 2017, **4**, 845–849.
- (82) M. Zhu, J. B. Jasinski and M. A. Carreon, *J. Mater. Chem.* 2012, **22**, 7684–

---

7686.

(83) K. Zhou, B. Mousavi, Z. Luo, S. Phatanasri, S. Chaemchuen and F. Verpoort, *J. Mater. Chem. A*. 2017, **5**, 952–957.

(84) F. Zheng, H. Xia, S. Xu, R. Wang and Y. Zhang, *RSC Adv.* 2016, **6**, 71767–71772.

(85) L. Wang, W. Gao, Z. Liu, Z. Zeng, Y. Liu, M. Giroux, M. Chi, G. Wang, J. Greeley, X. Pan and C. Wang, *ACS Catal.* 2018, **8**, 35–42.

(86) L. J. Garces, B. Hincapie, R. Zerger and S. L. Suib, *J. Phys. Chem. C* 2015, **119**, 5484–5490.

(87) X. Zhang and K. Y. Chan, *J. Mater. Chem.* 2002, **12**, 1203–1206.

(88) Y. Sun, J. Lopez, H. W. Lee, N. Liu, G. Zheng, C. L. Wu, J. Sun, W. Liu, J. W. Chung, Z. Bao and Y. Cui, *Adv. Mater.*, 2016, **28**, 2455–2461.

(89) D. Zhou, Y. Cui, P.-W. Xiao, M.-Y. Jiang and B.-H. Han, *Nat. Commun.* 2014, **5**, 4716.

(90) K. Artyushkova, B. Kiefer, B. Halevi, A. Knop-Gericke, R. Schlogl and P. Atanassov, *Chem. Commun.* 2013, **49**, 2539–2541.

(91) J. Chen, Y. Yang, J. Su, P. Jiang, G. Xia and Q. Chen, *ACS Appl. Mater. Interfaces* 2017, **9**, 3596–3601.

(92) A. L. Wang, X. J. He, X. F. Lu, H. Xu, Y. X. Tong and G. R. Li, *Angew. Chemie - Int. Ed.* 2015, **54**, 3669–3673.

(93) Y. Zheng, Y. Jiao, Y. Zhu, L. H. Li, Y. Han, Y. Chen, A. Du, M. Jaroniec and S. Z. Qiao, *Nat. Commun.* 2014, **5**, 3783.

(94) M. Zeng and Y. Li, *J. Mater. Chem. A*. 2015, **3**, 14942–14962.

(95) J. Su, Y. Yang, G. Xia, J. Chen, P. Jiang and Q. Chen, *Nat. Commun.*, 2017, **8**, 14969.

- 
- (96) P. Jiang, Y. Yang, R. Shi, G. Xia, J. Chen, J. Su and Q. Chen, *J. Mater. Chem. A*, 2017, **5**, 5475–5485.
- (97) Y. Xue, B. Huang, Y. Yi, Y. Guo, Z. Zuo, Y. Li, Z. Jia, H. Liu and Y. Li, *Nat. Commun.* 2018, **9**, 1460–1469.
- (98) X. Zhang, Z. Luo, P. Yu, Y. Cai, Y. Du, D. Wu, S. Gao, C. Tan, Z. Li, M. Ren, T. Osipowicz, S. Chen, Z. Jiang, J. Li, Y. Huang, J. Yang, Y. Chen, C. Y. Ang, Y. Zhao, P. Wang, L. Song, X. Wu, Z. Liu, A. Borgna and H. Zhang, *Nat. Catal.* 2018, **1**, 460–468.
- (99) T. F. Jaramillo, K. P. Jorgensen, J. Bonde, J. H. Nielsen, S. Horch and I. Chorkendorff, *Science* 2007, **317**, 100–102.
- (100) J. F. Callejas, J. M. McEnaney, C. G. Read, J. C. Crompton, A. J. Biacchi, E. J. Popczun, T. R. Gordon, N. S. Lewis and R. E. Schaak, *ACS Nano* 2014, **8**, 11101–11107.
- (101) J. Yin, Q. Fan, Y. Li, F. Cheng, P. Zhou, P. Xi and S. Sun, *J. Am. Chem. Soc.* 2016, **138**, 14546–14549.
- (102) E. J. Popczun, C. G. Read, C. W. Roske, N. S. Lewis and R. E. Schaak, *Angew. Chemie - Int. Ed.* 2014, **53**, 5427–5430.
- (103) H.-W. Liang, S. Brüller, R. Dong, J. Zhang, X. Feng and K. Müllen, *Nat. Commun.* 2015, **6**, 7992–7999.
- (104) E. J. Popczun, J. R. McKone, C. G. Read, A. J. Biacchi, A. M. Wiltrout, N. S. Lewis and R. E. Schaak, *J. Am. Chem. Soc.* 2013, **135**, 9267–9270.
- (105) S. Cobo, J. Heidkamp, P. A. Jacques, J. Fize, V. Fourmond, L. Guetaz, B. Jusselme, V. Ivanova, H. Dau, S. Palacin, M. Fontecave and V. Artero, *Nat. Mater.* 2012, **11**, 802–807.
- (106) J. Xie, H. Zhang, S. Li, R. Wang, X. Sun, M. Zhou, J. Zhou, X. W. Lou and

- 
- Y. Xie, *Adv. Mater.* **25**, 5807–5813.
- (107) H. Zhang, Z. Ma, J. Duan, H. Liu, G. Liu, T. Wang, K. Chang, M. Li, L. Shi, X. Meng, K. Wu and J. Ye, *ACS Nano* **10**, 684–694.
- (108) T. Wang, Y. Guo, Z. Zhou, X. Chang, J. Zheng and X. Li, *ACS Nano* **10**, 10397–10403.
- (109) M. Zhuang, X. Ou, Y. Dou, L. Zhang, Q. Zhang, R. Wu, Y. Ding, M. Shao and Z. Luo, *Nano Lett.* **16**, 4691–4698.
- (110) D. Voiry, H. Yamaguchi, J. Li, R. Silva, D. C. B. Alves, T. Fujita, M. Chen, T. Asefa, V. B. Shenoy, G. Eda and M. Chhowalla, *Nat. Mater.* **12**, 850–855.
- (111) R. Wang, X. Y. Dong, J. Du, J. Y. Zhao and S. Q. Zang, *Adv. Mater.*, **2018**, **30**, 1–10.
- (112) Y. Li, H. Wang, L. Xie, Y. Liang, G. Hong and H. Dai, *J. Am. Chem. Soc.*, **2011**, **133**, 7296–7299.
- (113) G. Liu, Y. Qiu, Z. Wang, J. Zhang, X. Chen, M. Dai, D. Jia, Y. Zhou, Z. Li and P. Hu, *ACS Appl. Mater. Interfaces*, **2017**, **9**, 37750–37759.
- (114) W. Zhou, K. Zhou, D. Hou, X. Liu, G. Li, Y. Sang, H. Liu, L. Li and S. Chen, *ACS Appl. Mater. Interfaces*, **2014**, **6**, 21534–21540.
- (115) W. Ren, H. Zhang and C. Cheng, *Electrochim. Acta.*, **2017**, **241**, 316–322.
- (116) K. Qi, S. Yu, Q. Wang, W. Zhang, J. Fan, W. Zheng and X. Cui, *J. Mater. Chem. A*, **2016**, **4**, 4025–4031.
- (117) T. Wang, L. Liu, Z. Zhu, P. Papakonstantinou, J. Hu, H. Liu and M. Li, *Energy Environ. Sci.*, **2013**, **6**, 625–633.
- (118) Y. Peng, B. Lu, L. Chen, N. Wang, J. E. Lu, Y. Ping and S. Chen, *J. Mater. Chem. A*, **2017**, **5**, 18261–18269.
- (119) B. Lim, M. Jiang, P. H. C. Camargo, E. C. Cho, J. Tao, X. Lu, Y. Zhu and Y.

- 
- Xia, *Science.*, 2009, **324**, 1302–1305.
- (120) P. Wu, H. Lv, T. Peng, D. He and S. Mu, *Sci. Rep.*, 2014, **4**, 1–6.
- (121) X. Han, F. Cheng, T. Zhang, J. Yang, Y. Hu and J. Chen, *Adv. Mater.* 2014, **26**, 2047–2051.
- (122) M. Zeng and Y. Li, *J. Mater. Chem. A* 2015, **3**, 14942–14962.
- (123) Y. Zheng, Y. Jiao, Y. Zhu, L. H. Li, Y. Han, Y. Chen, A. Du, M. Jaroniec and S. Z. Qiao, *Nat. Commun.* 2014, **5**, 1–8.
- (124) J. K. Nørskov, T. Bligaard, J. Rossmeisl and C. H. Christensen, *Nat. Chem.*, 2009, **1**, 37–46.
- (125) G. Cilpa-Karhu and K. Laasonen, *Phys. Chem. Chem. Phys.*, 2018, **20**, 2741–2753.
- (126) J. Su, Y. Yang, G. Xia, J. Chen, P. Jiang and Q. Chen, *Nat. Commun* 2017, **8**, 14969–14980.
- (127) V. I. Anisimov, J. Zaanen and O. K. Andersen, *Phys. Rev. B* 1991, **44**, 943–954.
- (128) N. Becknell, Y. Son, D. Kim, D. Li, Y. Yu, Z. Niu, T. Lei, B. T. Sneed, K. L. More, N. M. Markovic, V. R. Stamenkovic and P. Yang, *J. Am. Chem. Soc.* 2017, **139**, 11678–11681.
- (129) W. Tang, E. Sanville and G. Henkelman, *J. Phys. Condens. Matter* 2009, **21**, 84204–84210.
- (130) H. Bin Wu, B. Y. Xia, L. Yu, X. Y. Yu and X. W. Lou, *Nat. Commun.*, 2015, **6**, 6512.
- (131) G. Humagain, K. MacDougall, J. MacInnis, J. M. Lowe, R. H. Coridan, S. MacQuarrie and M. Dasog, *Adv. Energy Mater.*, 2018, **8**, 1801461.
- (132) H. Jin, J. Wang, D. Su, Z. Wei, Z. Pang and Y. Wang, *J. Am. Chem. Soc.*,

---

2015, **137**, 2688–2694.

(133) M. Gong, W. Zhou, M. C. Tsai, J. Zhou, M. Guan, M. C. Lin, B. Zhang, Y. Hu, D. Y. Wang, J. Yang, S. J. Pennycook, B. J. Hwang and H. Dai, *Nat. Commun.*, 2014, **5**, 4695.

(134) B. Cao, G. M. Veith, J. C. Neufeind, R. R. Adzic and P. G. Khalifah, *J. Am. Chem. Soc.*, 2013, **135**, 19186–19192.

(135) W. F. Chen, K. Sasaki, C. Ma, A. I. Frenkel, N. Marinkovic, J. T. Muckerman, Y. Zhu and R. R. Adzic, *Angew. Chemie - Int. Ed.*, 2012, **51**, 6131–6135.

(136) J. D. Benck, T. R. Hellstern, J. Kibsgaard, P. Chakthranont and T. F. Jaramillo, *ACS Catal.*, 2014, **4**, 3957–3971.

(137) C. G. Morales-Guio and X. Hu, *Acc. Chem. Res.*, 2014, **47**, 2671–2681.

(138) Y. Shi and B. Zhang, *Chem. Soc. Rev.*, 2016, **45**, 1529–1541.

(139) X. Zhang, X. Yu, L. Zhang, F. Zhou, Y. Liang and R. Wang, *Adv. Funct. Mater.*, 2018, **28**, 1706523.

(140) J. Song, C. Zhu, B. Z. Xu, S. Fu, M. H. Engelhard, R. Ye, D. Du, S. P. Beckman and Y. Lin, *Adv. Energy Mater.*, 2017, **7**, 1601555.

(141) H.-W. Liang, S. Brüller, R. Dong, J. Zhang, X. Feng and K. Müllen, *Nat. Commun.*, 2015, **6**, 7992.

(142) T. Liu, F. Yang, G. Cheng and W. Luo, *Small*, 2018, **14**, 1703748.

(143) Y. Qin, X. Han, S. Gadipelli, J. Guo, S. Wu, L. Kang, J. Callison and Z. Guo, *J. Mater. Chem. A*, 2019, **7**, 6543–6551.

(144) D. J. Yang, Q. Zhang, S. F. Yoon, J. Ahn, S. G. Wang, Q. Zhou, Q. Wang and J. Q. Li, *Surf. Coatings Technol.*, 2003, **167**, 288–291.

(145) J. Liu, Z. Wang, Y. Zhao, H. Cheng, C. Hu, L. Jiang and L. Qu, *Nanoscale*, 2012, **4**, 7563–7568.

- 
- (146) L. Fan, P. F. Liu, X. Yan, L. Gu, Z. Z. Yang, H. G. Yang, S. Qiu and X. Yao, *Nat. Commun.*, 2016, **7**, 10667.
- (147) Z. H. Sheng, L. Shao, J. J. Chen, W. J. Bao, F. Bin Wang and X. H. Xia, *ACS Nano*, **5**, 4350–4358.
- (148) Z. Wei, J. Wang, S. Mao, D. Su, H. Jin, Y. Wang, F. Xu, H. Li and Y. Wang, *ACS Catal.*, 2015, **5**, 4783–4789.
- (149) H. Guo, N. Youliwasi, L. Zhao, Y. Chai and C. Liu, *Appl. Surf. Sci.*, 2018, **435**, 237–246.
- (150) Y. K. Lee and S. T. Oyama, *J. Catal.*, 2006, **239**, 376–389.
- (151) V. Armel, S. Hindocha, F. Salles, S. Bennett, D. Jones and F. Jaouen, *J. Am. Chem. Soc.*, 2017, **139**, 453–464.
- (152) S. Ozden, S. Bawari, S. Vinod, U. Martinez, S. Susarla, C. Narvaez, J. Joyner, C. S. Tiwary, T. N. Narayanan and P. M. Ajayan, *Nanoscale*, 2019, **11**, 12489–12496.
- (153) X. Pan and G. Zhou, *Phys. Chem. Chem. Phys.*, 2018, **20**, 7968–7973.
- (154) L. Zhang, L. Han, H. Liu, X. Liu and J. Luo, *Angew. Chemie - Int. Ed.*, 2017, **56**, 13694–13698.
- (155) G. Li, J. Yu, J. Jia, L. Yang, L. Zhao, W. Zhou and H. Liu, *Adv. Funct. Mater.*, 2018, **28**, 1801332.
- (156) X. Tian, P. Zhao and W. Sheng, *Adv. Mater.*, 2019, **31**, 1808066.
- (157) C. Tang, L. Xie, X. Sun, A. M. Asiri and Y. He, *Nanotechnology*, 2016, **27**, 20LT02.
- (158) J. Deng, P. Ren, D. Deng and X. Bao, *Angew. Chemie - Int. Ed.*, 2015, **54**, 2100–2104.
- (159) E. J. Popczun, J. R. McKone, C. G. Read, A. J. Biacchi, A. M. Wiltrout, N.

- 
- S. Lewis and R. E. Schaak, *J. Am. Chem. Soc.*, 2013, **135**, 9267–9270.
- (160) G. Zheng, Z. Peng, D. Jia, A. M. Al-Enizi and A. A. Elzatahry, *Adv. Energy Mater.*, 2015, **5**, 140231
- (161) D. Kong, J. J. Cha, H. Wang, H. R. Lee and Y. Cui, *Energy Environ. Sci.*, 2013, **6**, 3553–3558.
- (162) P. Jiang, Q. Liu and X. Sun, *Nanoscale*, 2014, **6**, 13440–13445.
- (163) T. R. Cook, D. K. Dogutan, S. Y. Reece, Y. Surendranath, T. S. Teets and D. G. Nocera, *Chem. Rev.*, 2010, **110**, 6474–6502.
- (164) P. Xiao, W. Chen and X. Wang, *Adv. Energy Mater.*, 2015, **5**, 1500985.
- (165) Y. Jiao, Y. Zheng, M. Jaroniec and S. Z. Qiao, *Chem. Soc. Rev.*, 2015, **44**, 2060–2086.
- (166) H. Ang, H. T. Tan, Z. M. Luo, Y. Zhang, Y. Y. Guo, G. Guo, H. Zhang and Q. Yan, *Small*, 2015, **11**, 6278–6284.
- (167) Z. Pu, M. Wang, Z. Kou, I. S. Amiinu and S. Mu, *Chem. Commun.*, 2016, **52**, 12753–12756.
- (168) L. Tao, X. Duan, C. Wang, X. Duan and S. Wang, *Chem. Commun.*, 2015, **51**, 7470–7473.
- (169) X. Long, G. Li, Z. Wang, H. Zhu, T. Zhang, S. Xiao, W. Guo and S. Yang, *J. Am. Chem. Soc.*, 2015, **137**, 11900–11903.
- (170) M. A. R. Anjum and J. S. Lee, *ACS Catal.*, 2017, **7**, 3030–3038.
- (171) J. Zhang, L. Qu, G. Shi, J. Liu, J. Chen and L. Dai, *Angew. Chemie - Int. Ed.*, 2016, **55**, 2230–2234.
- (172) Y. Sun, L. Hang, Q. Shen, T. Zhang, H. Li, X. Zhang, X. Lyu and Y. Li, *Nanoscale*, 2017, **9**, 16674–16679.
- (173) W. F. Chen, S. Iyer, S. Iyer, K. Sasaki, C. H. Wang, Y. Zhu, J. T. Muckerman



- 
- and E. Fujita, *Energy Environ. Sci.*, 2013, **6**, 1818–1826.
- (174) Y. Qiu, Z. Wen, C. Jiang, X. Wu, R. Si, J. Bao, Q. Zhang, L. Gu, J. Tang and X. Guo, *Small*, 2019, **15**, 1900014.
- (175) M. Miao, J. Pan, T. He, Y. Yan, B. Y. Xia and X. Wang, *Chem. - A Eur. J.*, 2017, **23**, 10947–10961.
- (176) K. Xiong, L. Li, L. Zhang, W. Ding, L. Peng, Y. Wang, S. Chen, S. Tan and Z. Wei, *J. Mater. Chem. A*, 2015, **3**, 1863–1867.
- (177) H. Lin, N. Liu, Z. Shi, Y. Guo, Y. Tang and Q. Gao, *Adv. Funct. Mater.*, 2016, **26**, 5590–5598.
- (178) Y. Huang, Q. Gong, X. Song, K. Feng, K. Nie, F. Zhao, Y. Wang, M. Zeng, J. Zhong and Y. Li, *ACS Nano*, 2016, **10**, 11337–11343.
- (179) D. Das, S. Santra and K. K. Nanda, *ACS Appl. Mater. Interfaces*, 2018, **10**, 35025–35038.
- (180) J. Guo, J. Wang, Z. Wu, W. Lei, J. Zhu, K. Xia and D. Wang, *J. Mater. Chem. A*, 2017, **5**, 4879–4885.
- (181) C. Lu, D. Tranca, J. Zhang, F. Rodríguez Hernández, Y. Su, X. Zhuang, F. Zhang, G. Seifert and X. Feng, *ACS Nano*, 2017, **11**, 3933–3942.
- (182) F. X. Ma, H. Bin Wu, B. Y. Xia, C. Y. Xu and X. W. Lou, *Angew. Chemie - Int. Ed.*, 2015, **54**, 15395–15399.
- (183) F. Cárdenas-Lizana, D. Lamey, L. Kiwi-Minsker and M. A. Keane, *J. Mater. Sci.*, 2018, **53**, 6707–6718.
- (184) M. S. Park, J. H. Kim, Y. N. Jo, S. H. Oh, H. Kim and Y. J. Kim, *J. Mater. Chem.*, 2011, **21**, 17960–17966.
- (185) X. Fan, Y. Liu, Z. Peng, Z. Zhang, H. Zhou, X. Zhang, B. I. Yakobson, W. A. Goddard, X. Guo, R. H. Hauge and J. M. Tour, *ACS Nano*, 2017, **11**, 384–394.

- 
- (186) J. Sen Li, Y. Wang, C. H. Liu, S. L. Li, Y. G. Wang, L. Z. Dong, Z. H. Dai, Y. F. Li and Y. Q. Lan, *Nat. Commun.*, 2016, **7**, 11204.
- (187) M. Huang, W. Zeng and Z. Zhu, *R. Soc. Open Sci.*, 2019, **6**, 190547.
- (188) Y. Y. Chen, Y. Zhang, W. J. Jiang, X. Zhang, Z. Dai, L. J. Wan and J. S. Hu, *ACS Nano*, 2016, **10**, 8851–8860.
- (189) H. Yan, C. Tian, L. Wang, A. Wu, M. Meng, L. Zhao and H. Fu, *Angew. Chemie - Int. Ed.*, 2015, **54**, 6325–6329.
- (190) Z. Shi, K. Nie, Z. J. Shao, B. Gao, H. Lin, H. Zhang, B. Liu, Y. Wang, Y. Zhang, X. Sun, X. M. Cao, P. Hu, Q. Gao and Y. Tang, *Energy Environ. Sci.*, 2017, **10**, 1262–1271.
- (191) R. Ma, Y. Zhou, Y. Chen, P. Li, Q. Liu and J. Wang, *Angew. Chemie - Int. Ed.*, 2015, **54**, 14723–14727.
- (192) H. Vrubel and X. Hu, *Angew. Chemie - Int. Ed.*, 2012, **51**, 12703–12706.
- (193) H. Wei, Q. Xi, X. Chen, D. Guo, F. Ding, Z. Yang, S. Wang, J. Li and S. Huang, *Adv. Sci.*, 2018, **5**, 1700733.
- (194) L. Ma, L. R. L. Ting, V. Molinari, C. Giordano and B. S. Yeo, *J. Mater. Chem. A*, 2015, **3**, 8361–8368.
- (195) Y. Zhao, K. Kamiya, K. Hashimoto and S. Nakanishi, *J. Am. Chem. Soc.*, 2015, **137**, 110–113.
- (196) H. Bin Wu, B. Y. Xia, L. Yu, X.-Y. Yu and X. W. (David) Lou, *Nat. Commun.*, 2015, **6**, 6512.
- (197) L. Liao, S. Wang, J. Xiao, X. Bian, Y. Zhang, M. D. Scanlon, X. Hu, Y. Tang, B. Liu and H. H. Girault, *Energy Environ. Sci.*, 2014, **7**, 387–392.
- (198) P. Xiao, X. Ge, H. Wang, Z. Liu, A. Fisher and X. Wang, *Adv. Funct. Mater.*, 2015, **25**, 1520–1526.

---

(199) C. Wan, Y. N. Regmi and B. M. Leonard, *Angew. Chemie - Int. Ed.*, 2014, **53**, 6407–6410.